Three-dimensional Magnetotelluric Inversion

by

Anna Avdeeva

Thesis presented for the degree of

Doctor of Philosophy

to the National University of Ireland

Research conducted at:

The Dublin Institute for Advanced Studies,

5 Merrion Square, Dublin 2

and

Department of Earth and Ocean Sciences, Faculty of Science,

National University of Ireland, Galway

Supervisors: Dr. Colin Brown,

Professor Alan Jones and Dr. Dmitry Avdeev

January 2008

Contents

Contents

List of Symbols

Symbol	Description of Symbol
(x, y, z)	Cartesian coordinates [m] and z representing positive down
$\mathbf{E}$	Electric field vector with x, y and z components E_x, E_y and E_z respectively [Vm^{-1}]
$\mathbf{H}$	Magnetic field vector with x, y and z components H_x, H_y and H_z respectively [Am^{-1}], or Hessian matrix
T	Period [s]; $1/T$ = frequency f [s^{-1}]
ω	Angular frequency [rad s^{-1}] ; $\omega = 2\pi f$
μ	Permeability [Hm^{-1}]
μ_0	Magnetic permeability of vacuum [Hm^{-1}] ; $\mu_0 = 4\pi \times 10^{-7}$Hm^{-1}
ε	Dielectric permittivity
ρ	Electrical resistivity [Ωm]
ρ^{app}	Apparent resistivity [Ωm]
σ	Electrical conductivity [Sm^{-1}]; $\sigma = 1/\rho$
σ_k	Electrical conductivity of k-th cell or layer [Sm^{-1}]
δ	Skin depth [m], or Dirac's delta-function
$\mathbf{Z}_{ij}$	2×2 complex-valued matrix of MT impedance tensor
$\mathbf{D}_{ij}$	2×2 complex-valued matrix of observed MT impedance tensor
$\widetilde{\mathbf{D}}_{ij}$	2×2 complex-valued matrix of noiseless MT impedance tensor

Symbol	Description of Symbol
φ	Objective (or penalty) function
φ_d	Data misfit
φ_s	Regularization function (or stabilizer)
λ	Regularization parameter
$\mathbf{m}$	Vector consisting of model parameters
N	Number of model parameters
N_S	Number of MT sites
N_T	Number of frequencies
n_{it}	Number of quasi-Newton iterations
n_{fg}	Number of evaluations of penalty function together with its gradient
n_{cp}	Number of correction pairs
tr	Trace of its matrix argument
$\Re$	Real part of its argument
$\Im$	Imaginary part of its argument
$x3d$	IE forward modelling code by Avdeev *et al.* (1997, 2002)

List of Abbreviations

Abbreviation	Description of Abbreviation
1D	one-dimensional
2D	two-dimensional
3D	three-dimensional
EM	electromagnetism
MT	magnetotellurics
QN	quasi-Newton (method)
GN	Gauss-Newton (method)
NLCG	non-linear conjugate gradient (method)
BFGS	the Broyden-Fletcher-Goldfarb-Shanno algorithm
L-BFGS	the limited memory Broyden-Fletcher-Goldfarb-Shanno algorithm
L-BFGS-B	the limited memory Broyden-Fletcher-Goldfarb-Shanno algorithm for bound constrained optimization
FD	finite-difference (method)
FE	finite-element (method)
IE	integral equation (method)
MPI	message passing interface

Acknowledgements

There are a number of people without whose help, support and guidance I would never have completed this thesis.

First, I would like to express my thanks to my father Dmitry Avdeev with whom I constantly collaborated during this four-years work on my PhD. His patient and determined support, advice, expertise and helpful suggestions were always available at just the right moments. His knowledge of mathematics, geophysics and life not only helped me in writing this thesis, but taught me valuable lessons in all aspects of life.

My supervisors Alan Jones and Colin Brown gave me the opportunity to work with various researchers around the world and to present my work on numerous occasions. They together with my external examiner Mark Everett made a lot of detailed comments and suggestions, which helped to improve this thesis.

I also would like to thank Professor Luke Drury, the director of the CosmoGrid Project, for benevolence, interest in my work and kind support.

Max Moorkamp made a lot of important corrections and suggestions, which helped to improve this thesis immensely. He showed endless patience at work and at home during times of despair.

Thanks to Brian O'Reilly, who corrected the English in a number of papers and abstracts submitted to various journals and conferences.

During my two-month visit to the Laurence Berkeley National Laboratory in Summer 2006, Gregory Newman and Michael Commer showed me how to handle 3D finite-difference modelling codes in the frequency and the time domain. This visit helped to widen my scientific horizon.

Professor Hisashi Utada helped me with the hassle I had to get a Japanese visa and kindly hosted me in the Ocean Hemisphere Research Center of University of Tokyo in July 2007, where I could closely work with Dmitry Avdeev at the final stage of this work.

Thank you very much also to Jessica Spratt for leading the Canadian MT field-

works in summer 2004, which gave me a general understanding of MT.

I would like also to thank the rest of the School of Cosmic Physics staff at Merrion Square. Their company at numerous very interesting coffee breaks provided a great deal of diversion and entertainment.

Huge thanks to Hilary O'Donnell for helping with difficulties of my casual life and for being such a good friend. She was always there in every difficult situation.

Without the moral support of my parents and my grandmother I certainly could never have completed this thesis, or even started it.

Summary

The main objective of my PhD research is developing a better understanding of the mathematics, physics and numerical aspects of 3D MT inversion. This should lead to a working software that allows inversion of MT datasets in three dimensions. It is well known that reliable inversion includes three important and well-developed constituents: forward modelling, optimization and regularization methods. Fortunately, I am lucky to have full access to an up-to-date forward modelling code, *x3d*. In addition there is a large number of optimization and regularization techniques. Having all those components in place greatly facilitate my task. It should be understood however that developing such complicated software as 3D inversion is not by any means a simple mix of the three constituents mentioned above. Even if all three mentioned constituents are ready to be used, the development of reliable inversion software still requires many years of hard work, as is shown by experience of many other inversion software developers. So why is it not just a simple mix? First of all, all three main constituents should be adjusted to our specific case - 3D MT data. As an example, it is unclear a priori which optimization method better suits 3D MT inversion. The theory and algorithm of our chosen optimization method - the limited memory quasi-Newton (QN) method - is presented in Section 2.2. To investigate what specific parameters of QN optimization are optimal for 3D MT inversion we, as a start, studied thoroughly the 1D MT case (Chapter 3). Another important point is that optimization methods require the calculation of derivatives (such as gradients, Jacobians, Hessians) of some penalty function. In my work this important question is considered in Sections 3.1.1 and 4.1.1. Even more simple than this, it is unclear a priori what specific form of the penalty function is effective for 3D MT inversion. We introduce the chosen penalty function for the 3D case in Section 4.1. Finally, of course, the whole approach has to be verified on synthetic examples. We performed this verification for several representative MT models and present the results in Section 4.2 and Chapter 5.

In summary we have developed a working 3D MT inversion approach and verified

it on synthetic test examples.

Of course, as usual some unresolved problem remains. This problem is related to the physics of the 3D MT inversion itself, rather than to bugs in the numerical software. This problem manifests itself in the synthetic experiment presented in Section 4.2.4. There we encountered a problem that the recovered anomaly image shows erratic behaviour in conductivity in the upper part of the model. For the moment the reason for this behaviour is clear - sizes of inversion cells are much smaller than an average distance between MT sites and at the same time the gradient is much higher for cells located just below the sites. This problem is not new and some remedies has been proposed. For example, usage of model covariance matrix to address this problem is reported in Siripunvaraporn *et al.* (2005) or usage of preconditioning of Newton system by an approximation to the inverted Hessian matrix (Newman, personal communication). This is discussed in Chapter 5 and is subject of my ongoing research.

Regardless of this unresolved issue, our solution can be used to recover the true resistivity of the lower parts of realistic Earth models. Proper recovery of the true resistivity for the upper part of the models depends on many factors, such as the geometry and resistivity of the structures inside the Earth, coverage of the region by MT sites and many others.

Chapter 1.

Introduction

1.1. Thesis outline

This thesis consists of six chapters. As this work was performed in close collaboration with Dr. Dmitry Avdeev, I will also describe for each chapter the specific contributions I made.

In Chapter 1 we give a brief overview of magnetotellurics, and its contributions to understanding Earth interior structure and dynamic processes. Then we shortly outline the basic equations of electromagnetism - Maxwell's equations. In this chapter we also present the history and relevant references on three-dimensional magnetotelluric inversion.

In Chapter 2 we present the essential parts of our EM inversion technique. These are forward modelling, optimization and regularization methods. In Section 2.1, we describe the basics of the integral equation (IE) approach for modelling EM fields in three dimensions, since we use the *x3d* forward modelling IE code by Avdeev *et al.* (1997, 2002) as an engine for 3D inversion. In order to accelerate the inversion I parallelized critical subroutines of the *x3d* code using message passing interface (MPI). We outline this parallel implementation and present some results obtained on distributed and shared memory clusters in Section 2.1.3. A 2D digital convolution routine used by the IE method is a performance bottleneck in its serial implementation, and is this part that we accelerate through parallelization. In Section 2.2 we describe in detail how to formulate MT inversion as a quasi-Newton optimization problem. We also present the basic equation for a particular form of QN method, the so-called limited memory quasi-Newton method, which we further use in this work. It should be noted here that our setting is somewhat unconventional for EM, since we chose to use conductivities as model parameters and explicitly impose natural

conductivity constraints. The conventional way is to use logarithmic transformation to ensure positiveness of the conductivity values. In Section 2.3 we consider a Tikhonov-type regularization to stabilize the solution, as the inverse problem is ill-posed.

In order to test the QN method, I applied it to 1D MT and present the results in Chapter 3. Thus, we introduce the particular form of the data misfit and stabilizer we use for this case. In addition, we present a complete theory for calculating the gradient of the penalty function, based on the IE representation. This theory forms a very useful prelude to the general case of 3D inversion. I performed a large number of numerical studies for this 1D case to optimize the parameters for our limited memory quasi-Newton inversion. Tuning the method using 3D models would be too expensive in terms of computer time and storage.

Chapter 4 is a key chapter of this work. It is devoted to our solution of the 3D MT inverse problem. In Section 4.1 we present the problem as an optimization problem for a special form of penalty function. We propose this new form of penalty function, as it most adequately represents MT data misfit. There we also present the complete theory for the calculation of gradients of the penalty function with an adjoint method. The application of the adjoint method to the particular case of 3D MT was mainly performed by Dr. Dmitry Avdeev. The equations involved in this derivation are presented in Section 4.1.1. The solution of the inverse problem in three dimensions also requires an advanced type of regularization that I implemented and tested. Section 4.2 is devoted to synthetic model studies that are extremely important for proper judgment of the quality of our approach. These studies involve information about performance, robustness and limitations of the inversion. We present several 3D MT models and the corresponding results of the inversion obtained for these models.

Chapter 5 we discuss different preconditioners, which can help to smooth the erratic behaviour of the conductivity values in the upper part of the inversion results observed for some of our synthetic examples. In Chapter 6 we present some conclusions and outline the possibilities for future work.

Some additional material to further understand the inversion method is placed into appendices. This material is not essential for general comprehension, but gives deeper understanding of the mathematics involved.

1.2. History and main aspects of magnetotellurics

Magnetotellurics (MT) appeared in the 1950's as a method of electromagnetic sounding of the Earth (Tikhonov, 1950; Cagniard, 1953). In contrast to other geoelectrical methods, which are based on the study of the relationship between electromagnetic fields and their sources, the MT method is studying the ratios between the horizontal components of the electric (telluric) and magnetic fields to investigate the electrical conductivity structure of the Earth. This is due to the fact that the sources of MT are ionospheric and magnetospheric currents originating from the interaction of solar and near-earth plasma with the Earth's magnetic field, and we do not have precise information on the distribution of these currents. Fortunately, in most cases the electromagnetic field arising from these sources can be considered a plane wave and the source geometry does not need to be known. This is one of the advantages of MT, as the geometry of artificial sources complicates the interpretation (i.e. forward modelling and inversion). In the following section we describe the MT sources in more detail.

1.2.1. Sources

There are two major types of source mechanisms that generate electromagnetic fields used for MT soundings (e.g. Simpson and Bahr, 2005):

1. Above 1 Hz the electromagnetic waves used for MT sounding are generated by worldwide lightning activity. The electromagnetic waves emitted by individual lightning strokes get partially trapped in the waveguide, formed between the conductive ionosphere, the part of the atmosphere with the largest concentration of ions extending from 100 to 250 km above the Earth's surface, and the Earth. These waves can travel long distances and the lightning somewhere in the world is enough to provide a continuous source at any location of the Earth's surface. The measured field at the surface of the Earth is a superposition of waves generated from individual lightnings and the exact characteristics of the electromagnetic fields depends on the size, shape and the nature of the boundaries of the waveguide. As long as the measurements are far away from the individual thunderstorms this superposition can be considered as a plane wave.

2. Solar wind consists of ionized particles flowing radially outward from the sun.
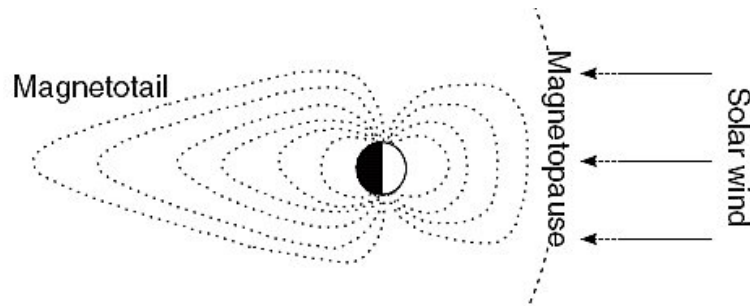
Figure 1.1.: Schematic image of magnetic field lines forming the Earth magnetosphere. The magnetosphere extends to more than 10 Earth radii on the day-side and to 40 radii on the night-side of the Earth (modified from Simpson and Bahr, 2005).

These ionized particles are deflected by the Earth's magnetic field at the outer region of the magnetosphere (at the magnetopause) and are guided around the Earth to the far tail, along the magnetic field lines (see Figure 1.1). When moving around the Earth they distort the Earth's magnetic field and generate their own field. The variations of these external magnetic fields can be measured at the surface of the Earth. The typical frequencies of these variations are from about 10^{-5} to 1 Hz. The amplitudes of these variations are greater at times of the high solar activity and reach several 100 nT at periods of several hours. When the solar wind is strongly enhanced, stronger magnetic effects occur, these are known as magnetic storms. Even though these storms provide a good source for MT measurements, when their activity becomes too strong, the plane wave assumption is no longer valid. Hence, segments of the data corresponding to these times should be discarded. This problem mostly exists in polar regions where charged particles come close to the Earth's surface in the cusp region, however when a storm is particularly large these effects can also be observed in mid-latitudes. Jones and Spratt (2002) provide a technique for identifying problematic segments of the data under some simplifying assumptions.

The narrow frequency range from 0.5 to 5 Hz, in the limit between solar wind and lightning activity, is known as the dead-band. In this frequency range the power spectrum of the natural electromagnetic field has a minimum (see Figure 1.2). In MT sounding curves this frequency range usually corresponds to a reduction of data quality.
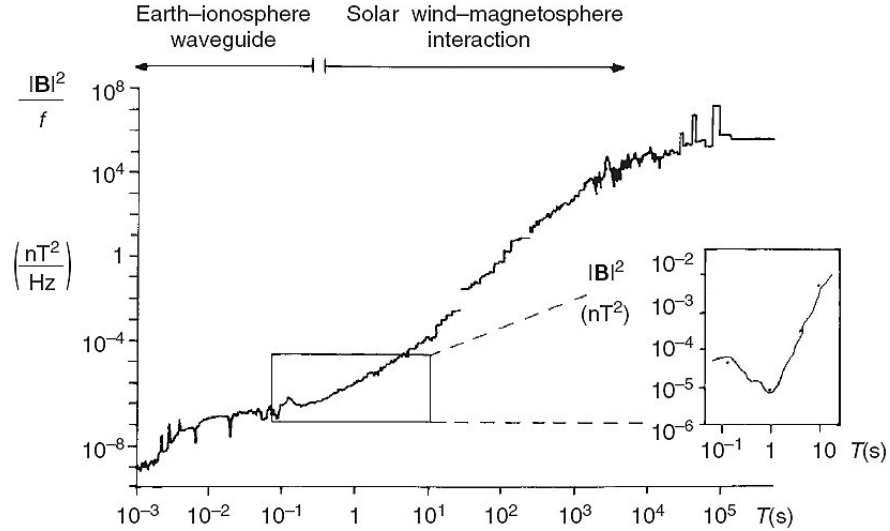
Figure 1.2.: Power spectrum of natural magnetic variations. The inset shows the minimum of the power spectrum in the dead-band (modified from Simpson and Bahr, 2005).

Both of the above source mechanisms create small, but measurable, time-varying electromagnetic signals. The problem is that the amplitudes of these signals vary considerably, which means that data have to be acquired for hours or even days at one MT site to ensure sufficient signal strength at all frequencies of interest.

1.2.2. Conductivity mechanisms in earth materials

As was mentioned earlier in this section the purpose of MT is to investigate the distribution of electrical conductivity inside the Earth's subsurface. In order to understand the expected conductivity variations and possible targets of MT surveys we will review the major conductivity mechanisms within the Earth.

Conductivity is the ability of a material to conduct electrical current. In rocks and minerals there are three types of the electrical charge transport mechanisms, these are semiconduction, electrolytic and electronic conduction.

1. The main conductivity mechanism in dry unaltered rocks in the crust and upper mantle is semiconduction. In this case the electrical current flow is due to the movement of positive holes or missing electrons. Typical resistivities due to this conduction mechanism are $10^3 - 10^6 \ \Omega m$. These are the upper limits of what is usually observed in MT surveys (e.g. Ledo *et al.*, 2004).

2. Electrolytic conduction means that the electric current is accompanied by the movement of matter in the form of ions. This type of conduction can appear in crustal rocks containing pores or fractures that are filled with fluid electrolytes containing, for example, NaCl. The amount of NaCl in the electrolyte fluid is usually the most important factor affecting the fluid saturated rock conductivity. This type of conduction usually suggested in tectonically active regions (e.g. Li *et al.*, 2003). Under the temperatures of the upper mantle water itself is present in the form of H^+ and OH^- ions which strongly enhance the observed conductivity (e.g. Gatzemeier and Moorkamp, 2005).

   In geothermal or volcanic areas very high conductivity can be explained by an interconnected network of partial melts, which is also act as electrolyte. Partial melts are formed when the temperature crosses the solidus line in pressure/temperature diagram. Small amounts of partial melt can greatly enhance the observed conductivity as long as it is interconnected and not in the form of isolated melt pockets (e.g. Heise *et al.*, 2007).

3. In electronic conductors, such as metals, the electrons can freely move within the material and transport charges. In the presence of an interconnected network of highly conducting matter, such as graphite or ores, this type of conduction increases the conductivity of the rock by orders of magnitude. Various groups of scientists assume this as a reason for the highly conductive areas within the crust (e.g. Haak *et al.*, 1997), however this is under debate, as electrolytic conduction through a similar interconnected pore system can be also an explanation (e.g. Li *et al.*, 2003).

A more detailed overview of mechanisms of conductivity together with some references can be found in the review paper by Nover (2005).

1.2.3. Practical measurements and processing

Although we will only give a theoretical justification of the method below, we describe here the practical aspects of acquiring MT data and how we obtain the frequency dependent impedance tensor that is the base of all MT surveys.

As explained above, MT is based on the simultaneous measurement of the horizontal components of the electric and magnetic fields at the Earth's surface. The exact way in which these fields are measured depends on the frequency range and whether the measurement site is on land or on the seafloor. We will concentrate

here on land-based measurements in the frequency range $300 \text{ Hz} - 10,000 \text{ s}$ as they are performed at the Dublin Institute for Advanced Studies.

Each component of the electric field in this frequency range is measured through the voltage between a pair of Pb/PbCl electrodes separated by $50 - 100$ m. As for a constant electric field the voltage increases linearly with the distance between the electrodes, longer separation allows to detect smaller signals and enhances the signal to noise ratio. However it is rarely practical to have separations greater than 100 m as the installation becomes increasingly difficult.

The magnetic fields are measured either with a set of coils for frequencies greater than 1 Hz or with three-component fluxgate magnetometers for longer periods. Modern broad-band magnetic coils have signal to noise ratios that allow to register signals with periods up to 5,000 s under ideal circumstances and fluxgate magnetometers therefore might seem unnecessary. In contrast to coils that measure the change of the magnetic field and whose sensitivity consequently falls of as 1/(frequency), fluxgate magnetometers have a nearly constant sensitivity below a threshold frequency and can better record long period signals. Thus often both types of sensors are installed at a single measurement site to ensure a wide frequency range can be used in the analysis. Regardless of which type of sensors are used, their electrical signals are digitized in a central recordings box and each component is stored on flash memory or a hard-disk as a time-series for further processing.

Even though MT processing is theoretically straightforward, modern processing algorithms use sophisticated statistical methods such as robust estimation (Egbert and Booker, 1986; Chave *et al.*, 1987) and the behaviour of the fields at neighbouring sites (Gamble *et al.*, 1979). This is necessary because any violation of the plane wave assumption can seriously distort the estimated impedance. We will restrict ourselves here to a basic description of the simplemost processing scheme, a more detailed review can be found in Egbert (2002).

The recorded time-series is divided into segments of equal length, depending on the total recording length and the longest period required. Each segment is fourier transformed and the auto- and cross-spectra are calculated. For each of those spectra we calculate the mean and the variance and then use a simple analytical formula to calculate the impedance estimates at the desired frequencies and their error. As mentioned above this way of calculating the estimates is highly susceptible to noise and therefore not recommended for practical applications. However it gives a better idea of the relationship between the measured quantities and the magnetotelluric

impedance used in inversion and modelling.

1.2.4. MT applications

Due to the huge frequency range from $10^{-5} - 10^4$ Hz and therefore depths of penetration from 10 m to up to 200 km, MT can be used for a large number of applications. In this section we present typical examples for some of most common ones.

1. *Deep crustal and mantle studies* The aim of crustal and mantle studies is usually to understand the structure and tectonic history of a certain region on a large scale. Therefore these kind of studies are mostly conducted by academic institutions although the results can also help the mining industry to understand fundamental properties of that region.

   Jones *et al.* (2001) present result from three MT experiments on the Slave craton, which became a very popular area for geosciences since the discovery of diamoniferous kimberlite pipes. The first experiment used conventional land-based broadband instruments (from 10^{-4} up to 10^4 Hz). For the second experiment they sank the electrodes to the bottom of the lake for electrical field recordings, while magnetometers were placed on the nearby shores. The third experiment used seafloor MT instruments deployed in the lakes. Analysing these data they found an electrical conductivity anomaly at a depth of ≈ 80 km that spatially coincides with the kimberlite field and is now known as the Central Slave Mantle Conductor (CSMC). To interpret this anomaly they discussed several possible causes for the high conductivity, such as melt, hydrated minerals, diffusion of hydrogen in the mantle, graphitization and sulfides. Combining their results with the results from geochemical data from the same area they suggest that the most probable explanation of the high conductivity is either interconnected graphite or dissolved hydrogen. They also speculate on possible tectonic formation processes that might have caused the enhanced conductivity. However the limited information available from this depth prevents the clear identification of a single cause.

2. *Geothermal studies* Geothermal studies are of interest to both academia and industry. Examining the structure of geothermal areas helps to understand basic properties of these systems and the connection to large scale tectonic processes, but also allows energy companies to identify interesting regions for geothermal power generation.

Heise *et al.* (2007) collected MT data along a profile across the Taupo Volcanic Zone (TVZ) consisting of 28 broad-band (0.003 - 2000 s) and 3 long period (10 - 10000 s) sites. Using the 2D inversion code by Rodi and Mackie (2001) and phase tensor analysis (Caldwell *et al.*, 2004) they constructed an electrical conductivity model beneath this geothermal zone. They showed that the resistive (500 - 1500 Ωm) crust is thinned underneath the TVZ from 20 to 10 km. Beneath this thinned crust there is an area of high conductivity (3 - 30 Ωm), which they interpret as a zone of melt accumulation. This interconnected melt zone starts at about 13 km depth, however the bottom of the conductor is not well constrained, which is typical for MT.

3. *Environmental studies* Usually shallow borehole measurements are used to investigate the extent and to monitor changes within waste sites. This technique, however, is relatively expensive. Buried waste often has an electrical conductivity much higher than the surrounding host material and therefore EM methods seem suitable for investigating the extent of the waste more economically. In addition, repeating these EM measurements can help to monitor the changes in conductivity within the waste site and the surrounding. Often groundwater contamination appears as a conductive zone around the waste site and can be identified from EM models. MT has been shown to be very useful for buried waste characterization when used at radio frequencies (from 10 kHz up to 1 MHz) (Pellerin, 2002). The principle of the radio magneto-telluric (RMT) method is the same as MT, but the source is the EM far-field of a radio transmitter, which can be viewed as a propagating plane wave. As RMT uses such high frequencies quick soundings are possible. As an example, Newman *et al.* (2003) had 320 RMT measurements using eight frequencies covering the range between 18.3 and 234 kHz. These measurements were collected over a buried waste site near Cologne, Germany. Inverting these data using a 3D MT inversion scheme (Newman and Alumbaugh, 2000) they successfully recovered the shape and extent of the contamination, which agrees with the borehole data. However, this success was partially due to incorporating a priori information within the inversion.

4. *Oil and mineral exploration* MT methods are important cheap supplementary methods to seismic surveys for petroleum exploration. Petroleum and natural gas are often trapped in pockets between rock and salt that were formed by

the upward movement of salt towards the surface, penetrating and bending the existing rock. Due to this fact, mapping the top and bottom of salt structures is important to identify the location of reservoirs. Salt structures contain entrained sediments that produce significant scattering and have strong reflecting vertical boundaries that produce ambiguities in the interpretation of seismic reflection data. Especially the steeply dipping sides and base of the salt are sometimes unresolved. Since the resistivity of salt is often more than ten times greater than the surrounding sediments, MT can help to resolve these problems. However, because of the attenuation of MT fields in conductive seawater the amplitude of the fields at short periods is within the noise level of traditional marine MT instruments. For this reason traditional instruments are used only at periods of 10^3 to 10^5 s in the marine environment. Yet, Hoversten *et al.* (1998) showed on the synthetic, but realistic examples that MT responses at periods from 1 and 10^3 s are sensitive to the salt structures at depth substantial for petroleum exploration. To solve this problem Constable *et al.* (1998) developed a novel broadband marine MT instrument and tested it for different sea water depths offshore San Diego. As a result they obtained good-quality responses at periods of 3 to 10^3 s in 1-km-deep water, while in shallower water due to wave activity and water currents the quality of the magnetic field recordings was not sufficient. They therefore suggest to replace these with nearby land magnetic recordings.

Using this novel instrumentation, data in the period band of 1 to 3000 s were collected over a salt body at Gemini Prospect, Gulf of Mexico. These data were used by Key *et al.* (2006) in order to investigate the effectiveness of using 2D marine MT methods to map 3D salt structures. Based on the result of the 2D inversion of 1) a synthetic dataset calculated for a 3D model constructed from the seismic salt model and 2) the real data, they conclude that for the adequate recovery of the boundaries of the salt structure, a full 3D inversion is needed. 2D inversion should still be used for data quality assessment, finding appropriate error floors and, most importantly, for constructing an improved starting model for 3D MT inversion.

These examples of recent applications of MT also show that most analyses of MT data are still performed with 2D inversion schemes and only rarely 3D tools are utilized. This is due to limited computer power, limited availability of 3D inversion codes and generally lower requirements in terms of number of stations for 2D surveys.

With current computer power and a greater variety of 3D inversion codes available it is starting to become mostly a matter of experimental design and costs whether 3D methods can be used or not.

1.3. Maxwell's equations and very basic definitions

Electromagnetic (EM) phenomena can be described by Maxwell's equations (presented here in the frequency-domain) (Ward and Hohmann, 1987)

$$\nabla \times \mathbf{H} = (\sigma - i\omega\varepsilon)\mathbf{E} + \mathbf{j}^{ext}, \tag{1.1a}$$

$$\nabla \times \mathbf{E} = i\omega\mu(\mathbf{H} + \mathbf{h}^{ext}), \tag{1.1b}$$

where μ and ε are the permeability and permittivity of the medium, respectively, σ is the electric conductivity, ω is the angular frequency of an EM field with assumed time-dependence $e^{-i\omega t}$, and $\mathbf{j}^{ext}$ and $\mathbf{h}^{ext}$ are external sources.

We will now shortly describe the definitions for forward and inverse problems that are commonly agreed on within the EM community. During forward modelling (1D, 2D or 3D) one numerically solves Maxwell's equations in order to calculate electric, $\mathbf{E}$, and magnetic, $\mathbf{H}$, fields within the volume of interest. Such mapping from the space of model parameters to the space of EM fields is called forward problem and we denote it as

$$\sigma, \varepsilon, \mu, \mathbf{j}^{ext}, \mathbf{h}^{ext} \longrightarrow \mathbf{E}, \ \mathbf{H}. \tag{1.2}$$

On the contrary, for inverse problem one assumes that the EM fields are known, usually at some sites on the surface (or underground) of the Earth, and the problem is to find a distribution of underground electrical conductivity, σ, permeability, μ, and permittivity, ε. In other words, the inverse problem is one of the following mappings

$$\mathbf{E}, \ \mathbf{H}, \ \mathbf{j}^{ext}, \ \mathbf{h}^{ext} \longrightarrow \sigma, \varepsilon, \mu, \tag{1.3a}$$

or

$$\mathbf{E}, \ \mathbf{H} \longrightarrow \underbrace{f(\mathbf{E}, \ \mathbf{H})}_{\text{transfer function}} \longrightarrow \sigma, \varepsilon, \mu. \tag{1.3b}$$

The electric and magnetic fields are functions of the extraneous sources, the conductivity distribution, and the point of observation. Fortunately, the transfer function in 1.3b that is independent of the geometry and polarization of the source can

be determined for MT. The MT transfer function is the impedance tensor, $\mathbf{Z}$. This tensor $\mathbf{Z}$ is a 2×2 complex-valued matrix

$$\begin{pmatrix} E_x \\ E_y \end{pmatrix} = \begin{pmatrix} Z_{xx} & Z_{xy} \\ Z_{yx} & Z_{yy} \end{pmatrix} \begin{pmatrix} H_x \\ H_y \end{pmatrix}. \tag{1.4}$$

This tensor relationship between the field components was first proposed by Neves (1957) and Berdichevsky (1960). In Appendix A we present some exact formulae for the MT impedance in the particular case of a layered-earth model.
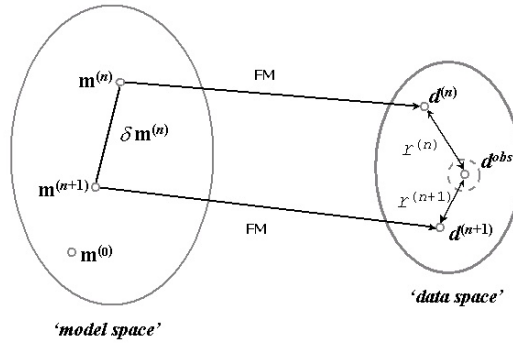

Figure 1.3.: Trivial scheme of model-data interaction.

In Figure 1.3 we present a trivial scheme of model-data interaction together with a schematic inverse procedure, which can be understood as following:

1) start with some initial guess model $\mathbf{m}^{(0)}$, $0 \to n$,

2) calculate the residual $r^{(n)} = \left\| d^{(n)} - d^{obs} \right\|$,

3) if $r^{(n)} \leq \varepsilon$ stop, else goto 4)

4) jump in the model space from model $\mathbf{m}^{(n)}$ to some other model $\mathbf{m}^{(n+1)}$,

5) $n + 1 \to n$, goto 2

In the above algorithm, $d^{(n)} = F(\mathbf{m}^{(n)})$ is the solution of the forward problem for the model $\mathbf{m}^{(n)}$, and ε is some preassigned tolerance.

From this trivial scheme we recognize two important components of the inversion procedure. First, the solution of the forward problem, and second, finding a way of jumping in the space of model parameters.

1.4. History of 3D MT inversion

Since Tikhonov's and Cagniard's times, the MT method has dramatically developed. Generally, modern MT can be viewed as a discipline, consisting of several self-contained parts, such as the MT equipment design, data acquisition, processing etc. In particular, it includes data interpretation, which, in its turn, includes a numerical inversion as an important constituent. Starting from the 1D case (in Tikhonov's and Cagniard's time) through 2D case (in the 70's), it has now become feasible to invert data with respect to a 3D Earth model. In other words the inversion in three dimensions is an actual and important topic of modern MT. To further back up the idea of importance of 3D MT inversion today, we mention three international meetings partially devoted to this subject (Oristaglio and Spies, 1999; Zhdanov and Wannamaker, 2002; Macnae and Liu, 2003). We see three main reasons for that - first, significant improvement in instruments and acquisition techniques, second, dramatic rise in numerical methods and computer performance and, third, the need among geologists and Earth scientists to understand crustal-scale geological structures and processes.

Interestingly, in spite of the urgent need for sophisticated 3D MT inversion software only a few developments of such a software are reported. It is not very surprising considering the level of complexity of 3D MT inverse problems (Mackie and Madden, 1993; Mackie *et al.*, 2001; Newman and Alumbaugh, 2000; Newman *et al.*, 2003; Zhdanov and Golubev, 2003; Sasaki, 2004; Siripunvaraporn *et al.*, 2005; Avdeev and Avdeeva, 2006). Here we briefly summarize the main achievements of these previously published works.

Usually a solution of the inverse problem is sought as a stationary point of some penalty functional $\varphi(\mathbf{m})$. In order to do this Newton-type iterative methods are commonly applied. These methods traditionally require to compute and store the sensitivity matrix $\mathbf{J} = \frac{\partial F}{\partial m}$ (F - forward problem solution) and Hessian matrix $\mathbf{H} = \frac{\partial^2 \varphi}{\partial m^2}$, or its approximation. These matrices are long to compute and large memory is required in order to store them in the 3D case. That is why it is important to make this computations more economical or even try to avoid them.

Mackie and Madden (1993) present algorithms for the solution of a 3D least-squares inverse problem using the conjugate gradient method (CG). This method does not require to calculate the sensitivity matrix $\mathbf{J}$ explicitly. At each iteration it only needs to compute the effect of the sensitivity matrix or its transpose mul-

tiplied by an arbitrary vector. They show that this is equivalent to the solution of two forward problems per frequency with sources distributed throughout the volume and across the surface and demonstrate that their procedure works well for simple 3D models. Newman and Alumbaugh (2000); Newman *et al.* (2003); Mackie *et al.* (2001) use another optimization approach – the non-linear conjugate gradient method (NLCG) by (Fletcher and Reeves, 1964; Polak and Ribiere, 1969) for the 3D MT inversion solution development. This approach avoids the calculation of sensitivities, but requires to compute the gradient vectors $\mathbf{g} = \frac{\partial \varphi}{\partial m}$ instead. The evaluation of the gradients involves a single solution of one forward problem and one adjoint problem at each NLCG iteration. This approach has been used to invert commercial datasets.

Zhdanov and Golubev (2003) developed a 3D inversion algorithm also based on the NLCG method. To speed up the solution of the inverse problem they use a quasi-analytical approximation for the forward modelling solution. Another optimization method used to invert 3D MT data is the Gauss-Newton method (GN). This method requires to calculate the sensitivity matrix $\mathbf{J}$ in order to compute a first order approximation to the Hessian matrix $\mathbf{H}$. Sasaki (2004) developed a 3D MT inversion based on a typical GN optimization with some modifications made to reduce the number of forward modellings to a reasonable level. His inversion algorithm allows to invert the MT data with static shift. Siripunvaraporn *et al.* (2005) successfully developed a solution based again on a GN approach, but this time in data space to reduce the size of the sensitivity matrix, as in 3D the amount of data is usually much smaller than the number of model parameters.

In this work we apply a limited memory quasi-Newton optimization method to solve the 3D MT inverse problem. Quasi-Newton methods, similarly to NLCG, also require only the gradients $\mathbf{g}$ of the penalty functional φ to be supplied at each iteration. Using the gradients these methods construct an approximation to the Hessian matrix or its inverse. When computing the approximation to the inverse of the Hessian they circumvent the solution of the system of linear equations at each iteration, which is necessary for GN method. However their approximations to the Hessian or its inverse are usually dense, which makes it difficult to store and compute them in memory for large-scale problems. In this cases a modification of the method has to be applied. One of such modifications – the limited memory quasi-Newton method – obtains an inverse Hessian approximation that can be stored in just a few vectors. The length of these vectors is the same as the amount of model parameters.

This method is fairly robust and inexpensive, does not converge rapidly (Nocedal and Wright, 1999). As far as we know this method has never been applied before to solve an MT inverse problem, although Haber (2005) used QN methods to invert controlled-source electromagnetic data.

Chapter 2.

Essential parts of EM inversion

In this chapter we present the main constituents of EM inversion: forward modelling, optimization and regularization. In our current implementation we use the integral equation forward modelling code *x3d* by Avdeev *et al.* (1997, 2002). We chose to use a limited memory quasi-Newton optimization method, as an optimization technique. For regularization, we used various Tikhonov-type regularizations. The essential details of these components are described below; we begin with the forward modelling technique used.

2.1. Forward modelling method

There are three main ways of solving the forward problem: finite-difference (e.g. Mackie *et al.*, 1993; Newman and Alumbaugh, 1995; Xiong, 1999; Wang and Fang, 2001; Siripunvaraporn *et al.*, 2002), integral equation (e.g. Hohmann, 1975; Wannamaker, 1991; Avdeev *et al.*, 1997, 2002) and finite-element (e.g. Reddy *et al.*, 1977; Zyserman and Santos, 2000; Badea *et al.*, 2001; Mitsuhata and Uchida, 2004) approaches. The FD methods are the most widely used, mostly due to the apparent simplicity of the numerical implementation. IE methods are not so trivial in their implementation, however if they are implemented accurately they are efficient in terms of computer memory. FE methods are still not widely used in 3D MT modelling, due to the nontrivial and time-consuming construction of the finite elements themselves. This approach operates with unstructured meshes, and hence, is more appropriate for complex geometries, than FD and IE methods (Badea *et al.*, 2001).

For all of these approaches the initial system of Maxwell's equations reduces to the system of linear equations

$$\mathbf{Ax} = \mathbf{b}. \tag{2.1}$$

The difference between these three approaches is the properties of the matrix **A**. For FD the matrix **A** is complex, large, sparse and symmetric. For FE this matrix is also complex, large and sparse, but now it is usually nonsymmetric. For the IE approach the matrix **A** is complex and dense, but much more compact than for FD or FE.

The important points here for all three approaches are how well the system 2.1 approximates the original system of Maxwell's equations and how fast one can find its solution **x**. After many years of competition we have a few accurate, reliable and fast FD, FE and IE forward solvers. Comparison of these solvers is a very difficult task, for the reason that they perform better for different models and there is always a large number of meshes (completely different for different approaches) that have to be used to find the most appropriate ones. One of the attempts to compare FD, FE and IE was the COMMEMI project of Zhdanov *et al.* (1997). One should understand that the COMMEMI project was performed in 1997 and the results are out of date. The more complete overview and reference list on forward modelling can be found in the recent review paper by Avdeev (2005).

I have never worked with any of FE forward solvers, but had an opportunity to work with the IE *x3d* code, which is used as an engine for our inversion solution and had some experience with two advanced 3D FD forward modelling codes, during a two-month visit to the Lawrence Berkeley National Laboratory. These FD codes are a time-domain FD code by Commer and Newman (2004) and a frequency-domain FD code by Newman and Alumbaugh (1995). As the results of this two-month work are not related to MT inversion, I present them in Appendix E.

Regarding the forward modelling solver for my PhD research, I had only two options: (a) to develop such a code myself, or (b) to use an existing code written by somebody else. Item (a) involves enough work for a PhD thesis, and therefore was an unacceptable option. Item (b) also presents some difficulties, since the development of an MT inversion solution requires access to a forward modelling code together with its sources. Additionally, this code has to be able to handle controlled-source problems along with MT ones for reasons we will explain below. Fortunately, I had access to the *x3d* code through collaboration with Dr. Dmitry Avdeev. This code is based on a volume integral equation method originally presented by Singer (1995). The relevant references about the further development of the method can be found, for example, in Avdeev *et al.* (2002). A serial implementation of the method, named *x3d*, is thoroughly described in the papers of Avdeev *et al.* (1997, 2002), where the

reader can find more details about the algorithm. Here we also present a parallel implementation of this code. This parallel implementation is essential for 3D EM inversion, as it reduces the required computation times significantly.

In Section 2.1.1 we briefly summarize the main aspects of the volume IE approach. We present formulae of the 3D IE EM forward modelling method that are of importance for us.

In Section 2.1.2, we describe some numerical bottlenecks of the serial *x3d* code and show how the solution may be parallelized to circumvent these bottlenecks. In particular, we demonstrate that a 2D digital convolution is the most time-consuming part, at least for large-scale models. Further, in Subsection 2.1.3 we analyse to what extent our parallel implementation outperforms the serial *x3d* solution for various numbers of processors and model sizes. Comparisons have been undertaken on both distributed and shared memory clusters. The results presented are encouraging and suggest the parallel implementation can accelerate the *x3d* solution and, therefore, the inversion of EM data. This parallel implementation is one of the important parts of this thesis, but it is by no means a main scientific contribution to the work.

2.1.1. Key formulae of IE method

In this section we summarize the main aspects of the forward modelling code *x3d* based on the volume IE approach, following works by Avdeev *et al.* (1997, 2002). For the volume IE approach, first we have to choose some reference model with generalized conductivity $\zeta_0 = \sigma_0 - i\omega\varepsilon_0$. This model can be chosen in many ways with the condition that we are able to effectively calculate the 3×3 dyadic Green's tensors for it. For example, it can have isotropic or transversely anisotropic conductivity. Avdeev *et al.* (1997) present the explicit formulae of the Green's tensors for a general case of a layered uniaxial anisotropic model. Anisotropic conductivity has been observed in lab measurements on the upper mantle materials (e.g. Simpson and Tommasi, 2005) and is sometimes used to explain MT data (e.g. Mareschal *et al.*, 1995).

Once the reference model is chosen, we can write the following system of Maxwell's equations:

$$\nabla \times \mathbf{H}^0 = \zeta_0 \mathbf{E}^0 + \mathbf{j}^{ext}, \qquad (2.2a)$$

$$\nabla \times \mathbf{E}^0 = i\omega\mu(\mathbf{H}^0 + \mathbf{h}^{ext}), \qquad (2.2b)$$

where $\mathbf{E}^0$ and $\mathbf{H}^0$ are the electric and magnetic fields, respectively. Using the definition of the Green's tensor the electric field $\mathbf{E}^0$ is easy to calculate as

$$\mathbf{E}^0(\mathbf{r}) = \int_{V^{ext}} G_0^{ee}(\mathbf{r}, \mathbf{r}')(\mathbf{j}^{ext}(\mathbf{r}') + \nabla \times \mathbf{h}^{ext}(\mathbf{r}'))d^3\mathbf{r}', \tag{2.3}$$

where V^{ext} is the volume supporting the extraneous current $\mathbf{j}^{ext} + \nabla \times \mathbf{h}^{ext}$, $\mathbf{r} = (x, y, z)$, $\mathbf{r}' = (x', y', z')$ are the vectors of 3D space, $d^3\mathbf{r}' = dx'dy'dz'$ is the element of 3D volume. Substracting equations 2.2 from equations 1.1 we obtain the system of Maxwell's equations for the scattered fields:

$$\nabla \times \mathbf{H}^s = \zeta_0 \mathbf{E}^s + \mathbf{j}^q, \tag{2.4a}$$

$$\nabla \times \mathbf{E}^s = i\omega\mu\mathbf{H}^s. \tag{2.4b}$$

In equations 2.4 $\mathbf{E}^s = \mathbf{E} - \mathbf{E}^0$ and $\mathbf{H}^s = \mathbf{H} - \mathbf{H}^0$ are the scattered electric and magnetic fields, respectively, and $\mathbf{j}^q = (\zeta - \zeta_0)(\mathbf{E}^s + \mathbf{E}^0)$.

We can derive the scattered electric field in a similar manner to formula 2.3.

$$
\begin{aligned}
\mathbf{E}^s(\mathbf{r}) &= \int_{V^s} G_0^{ee}(\mathbf{r}, \mathbf{r}')\mathbf{j}^q(\mathbf{r}')d^3\mathbf{r}' \\
&= \mathbf{E}_0(\mathbf{r}) + \int_{V^s} G_0^{ee}(\mathbf{r}, \mathbf{r}')(\zeta(\mathbf{r}') - \zeta_0(\mathbf{r}'))\mathbf{E}^s(\mathbf{r}')d^3\mathbf{r}',
\end{aligned}
\tag{2.5}
$$

where $\mathbf{E}_0(\mathbf{r}) = \int_{V^s} G_0^{ee}(\mathbf{r}, \mathbf{r}')(\zeta(\mathbf{r}') - \zeta_0(\mathbf{r}'))\mathbf{E}^0(\mathbf{r}')d^3\mathbf{r}'$ is a free term, and the volume V^s is the volume where $\zeta - \zeta_0$ differs from 0. Equation 2.5 is a traditional integral scattering equation (Dmitriev, 1969; Weidelt, 1975a).

In order to efficiently solve this scattering equation for models with high conductivity contrasts, the modified iterative dissipative method (MIDM) should be applied. This method was first proposed by Singer (1995). Following MIDM the following change of variables has to be made $\mathbf{E}^s \to \chi$, where

$$\chi(\mathbf{r}) = \frac{1}{2}\nu^{-1}(\mathbf{r})\left[(\zeta(\mathbf{r}) + \overline{\zeta_0(\mathbf{r})})\mathbf{E}^s(\mathbf{r}) + (\zeta(\mathbf{r}) - \zeta_0(\mathbf{r}))\mathbf{E}^0(\mathbf{r})\right]. \tag{2.6}$$

Here $\nu = diag\left(\sqrt{\Re(\zeta_{0\tau})}, \sqrt{\Re(\zeta_{0\tau})}, \sqrt{\Re(\zeta_{0z})}\right)$, the upper bar and $\Re$ in the above expressions, as everywhere else, are the complex conjugate and real parts of their argument, respectively. After this change of variables we can rewrite equation 2.5

as:

$$\chi(\mathbf{r}) = \chi_0(\mathbf{r}) + R(\mathbf{r})\chi(\mathbf{r}) + 2\nu(\mathbf{r}) \int_{V^s} G_0^{ee}(\mathbf{r}, \mathbf{r}')\nu(\mathbf{r}')R(\mathbf{r}')\chi(\mathbf{r}')d^3\mathbf{r}', \qquad (2.7)$$

where

$$\chi_0(\mathbf{r}) = R(\mathbf{r})\nu(\mathbf{r})\mathbf{E}^0(\mathbf{r}) + 2\nu(\mathbf{r}) \int_{V^s} G_0^{ee}(\mathbf{r}, \mathbf{r}')\nu(\mathbf{r}')R(\mathbf{r}')\nu(\mathbf{r}')\mathbf{E}^0(\mathbf{r}')d^3\mathbf{r}'. \qquad (2.8)$$

To derive the above equations 2.7 and 2.8 we used the formula $\overline{\zeta_0} + \zeta_0 = 2\nu^2$ and the notation $R = (\zeta - \zeta_0)(\zeta + \overline{\zeta_0})^{-1}$.

From equation 2.7, imposing a numerical grid on the model allows us to derive the following system of linear equations with respect to the unknown field χ:

$$(A\chi)_{i,j,k} = (\chi_0)_{i,j,k}. \qquad (2.9)$$

Operator A of equation 2.9 is defined as follows

$$(A\chi)_{i,j,k} = \chi_{i,j,k} - (R\chi)_{i,j,k} - \Phi_2^{-1} \left[\sum_{k'=1}^{N_z} Q_{k,k'}\Phi_2 \left[(\widetilde{R\chi})_{k'} \right] \right]_{i,j}. \qquad (2.10)$$

It is assumed that the modelling volume V^s is discretized by prisms $D_{i,j,k}$ ($i = 1, ..., N_x, j = 1, ..., N_y, k = 1, ..., N_z$), where we assume also that all prisms in the mesh are of the same horizontal size, but their vertical size is variable along the vertical axis. Subscript i, j, k of equation 2.10 stands for an average value over prism $D_{i,j,k}$. In this key equation

$$R_{i,j,k} = (\zeta_{i,j,k} - (\zeta_0)_k) \left(\zeta_{i,j,k} + \overline{(\zeta_0)_k} \right)^{-1}; \qquad (2.11)$$

Φ_2 and Φ_2^{-1} are respectively the direct and inverse 2D digital Fourier transforms over both subscripts i and j;

$$(Q_{k,k'})_{i',j'} = 2\nu_k \Phi_2 \left[\widetilde{q}_{k,k'} \right]_{i',j'} \nu_{k'}, \qquad (2.12)$$

where $i' = 1, ..., 2N_x$, $j' = 1, ..., 2N_y$,

$$\nu_k = diag \left(\sqrt{\Re(\zeta_{0\tau})_k}, \sqrt{\Re(\zeta_{0\tau})_k}, \sqrt{\Re(\zeta_{0z})_k} \right), \qquad (2.13)$$

and

$$(q_{k,k'})_{i,j} = \int_{D_{i,j,k'}} G_0^{ee}(x, y, z_k, z')dz'. \tag{2.14}$$

Here z_k is the depth of the centre of prism $D_{i,j,k}$.

The theory for the derivation of equation 2.10 from equation 2.7 is explained in appendix B. There the reader also can find an explanation for the tilde sign.

The serial implementation of Avdeev *et al.* (2002) solves the system 2.9 using a Krylov subspace iteration technique. This iteration technique generates the sequence of Krylov approximations, $\left\{\chi_{i,j,k}^{(n)}\right\}$, $n = 1, ...,$ that approach the solution, $\chi_{i,j,k}$, of the system 2.9 as

$$\chi_{i,j,k} \approx \lim_{n \to \infty} \chi_{i,j,k}^{(n)}. \tag{2.15}$$

The stopping criteria for the Krylov iteration is based on reducing the relative residual

$$r^{(n)} = \frac{\left\| A\chi^{(n)} - \chi_0 \right\|_{L_2}}{\left\| \chi_0 \right\|_{L_2}} \tag{2.16}$$

down to a user-determined level ε.

When the solution $\chi_{i,j,k}$ of equation 2.15 is found, the electric field within the modelling volume V^s is calculated as

$$\mathbf{E}_{i,j,k} = \left(\zeta_{i,j,k} + \overline{(\zeta_0)_k}\right)^{-1} \left(2\nu_k\chi_{i,j,k} - \mathbf{j}_{i,j,k}^s\right) + \mathbf{E}_{i,j,k}^0, \tag{2.17}$$

where

$$\mathbf{j}_{i,j,k}^s = (\zeta_{i,j,k} - (\zeta_0)_k)\mathbf{E}_{i,j,k}^0, \tag{2.18}$$

and $\mathbf{E}_{i,j,k}^0$ is the reference electric field.

In the context of this study it is of particular importance that the solution exploits the multiple calculation of a discrete 2D convolution given on the right hand side of equation 2.10.

2.1.2. Bottlenecks of serial implementation

The performance of the serial implementation *x3d* for the solution presented above strongly depends on two time-consuming parts of the algorithm. The first is the calculation of the 3×3 Green's matrices $(Q_{k,k'})_{i',j'}$ given in equation 2.12, where $k, k' = 1, ..., N_z$, $i' = 1, ..., 2N_x$ and $j' = 1, ..., 2N_y$. This requires the calculation of $9 \times 2N_x \times 2N_y \times N_z^2$ complex-valued numbers in total. It should be noted that

x3d stores the Green's matrices $(Q_{k,k'})_{i',j'}$ on hard disk for large-scale problems, and standard IO operations are used to read and write them to RAM when needed. This allows *x3d* to carry out this calculation only once during the whole iterative solution process, at the very beginning.

The second time-consuming part is the multiple 2D convolution presented in the right hand side of equation 2.10. The amount of these convolutions depends on the number of Krylov iterates. Figures 2.1 and 2.2 present a typical computation time ratio between those two parts of the *x3d* solution. This ratio

$$q = \frac{T_{A\chi}}{T_Q} \tag{2.19}$$

is a fraction of the wall time, $T_{A\chi}$, spent by the *x3d* solution within the 2D convolution routine, summed up for all Krylov iterates, over the wall time, T_Q, required for calculation of the Green's matrices $(Q_{k,k'})_{i',j'}$. The ratio 2.19 is presented for 3D models with a conductivity contrast of 30 in bilogarithmic scale as a function of the model sizes $N_x(= N_y)$ and N_z.
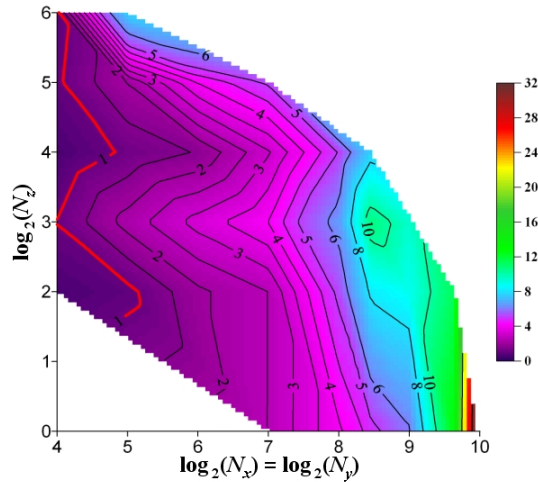

Figure 2.1.: Factor q of equation 2.19 obtained on a distributed memory cluster Leda. The results are presented in bilogarithmic scale as a function of model sizes $N_x(= N_y)$ and N_z.

It is interesting that, for the models considered, the whole *x3d* solution requires only six Krylov iterates to achieve a relative residual as small as $\varepsilon = 5 \times 10^{-4}$. The models with higher conductivity contrasts would need more Krylov iterates, and hence, the ratio q for these models would be even larger than that presented in Figures 2.1 and 2.2. From these figures we can see that the ratio q can be as large
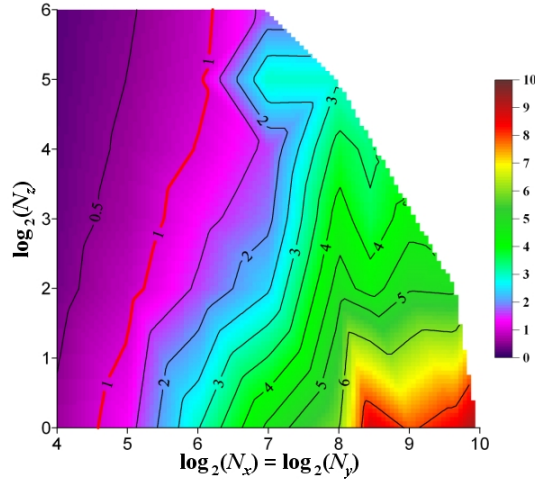
Figure 2.2.: Factor q of equation 2.19 obtained on a shared memory cluster Hamilton. The results are presented in bilogarithmic scale as a function of model sizes $N_x(= N_y)$ and N_z.

as 30 for the models considered. Therefore, we conclude that the 2D convolution routine is the best candidate for acceleration of EM inversion through parallelization of the *x3d* computer code. Accordingly, we implemented this solution on distributed and shared memory clusters to investigate relative improvements in computational speed.

2.1.3. Parallel implementation

2.1.3.1. Distributed memory cluster

First we developed a parallel implementation of the solution described above to run on a distributed memory cluster. Similar work was previously undertaken by Yoshioka and Zhdanov (2005) using the ScaLAPACK package. In our implementation, however, we adopted a more trivial scheme, which assigns the number k (number of the layer) given in the right hand side of equation 2.10 to the kth processor of the cluster. In other words, the kth processor calculates $(A\chi)_{i,j,k}$ of equation 2.10 for all $i = 1, ..., N_x$ and $j = 1, ..., N_y$. A modification of this approach to the case where the total number N_{pr} of processors is less than N_z is straightforward and easy to implement.

The acceleration factor

$$q_{N_{pr}} = \frac{T_{A\chi}^1}{T_{A\chi}^{N_{pr}}} \tag{2.20}$$
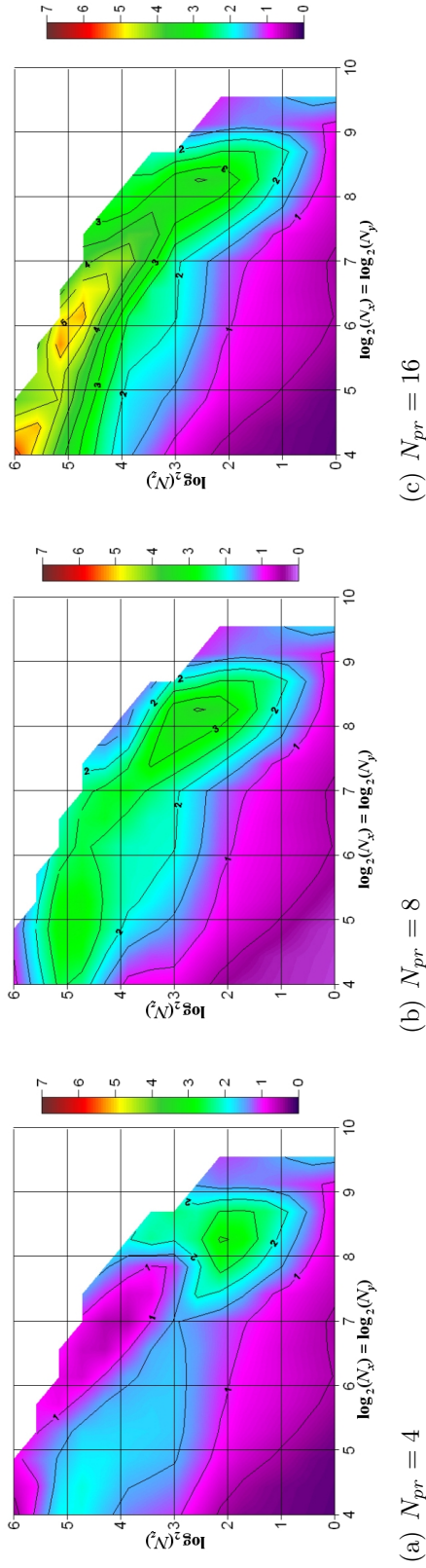
(a) $N_{pr} = 4$

(b) $N_{pr} = 8$

(c) $N_{pr} = 16$

Figure 2.3.: The results on the distributed memory cluster (Leda). Factor $q_{N_{pr}}$ of equation 2.20 for $N_{pr} = 4, 8, 16$. The results are presented in bilogarithmic scale as a function of model sizes $N_x(= N_y)$ and N_z.

of the parallel implementation over the serial one is presented in Figure 2.3. Here $T_{A\chi}^{N_{pr}}$ is the wall time for the calculation of $(A\chi)_{i,j,k}$, using N_{pr} processors. For our research we used a Linux cluster (Leda) available at the Dublin Institute for Advanced Studies. This cluster has 16 nodes, each with 2 processors, networked through a Gigabit ethernet. To parallelize the solution we used the MPI (message passing interface) for the interprocessor communications. The panels 2.3(a), 2.3(b), and 2.3(c) show the factor $q_{N_{pr}}$ of equation 2.20, calculated for various numbers of processors $N_{pr} = 4, 8, 16$, as a function of the model size of $N_x(= N_y) = 16, 32, 64, 128, 256, 512, 1000$ and $N_z = 1, 4, 16, 32, 64$. From Figure 2.3(c) we can see that for as much as $N_{pr} = 16$ processors the maximum acceleration, defined by $q_{N_{pr}}$, is less than 6. This is because interprocessor communication takes up a lot of wall time. In particular, the N_z arrays of $\Phi_2\left[(\widetilde{R}\widetilde{\chi})_{k'}\right]$ of equation 2.10 for all $k' = 1, ..., N_z$ must be broadcast to all processors. This is a very time-consuming operation on a distributed memory cluster. Indeed, since

$$T_{A\chi}^{N_{pr}} \approx \frac{T_{A\chi}^1}{N_{pr} - 1} + T_{comm},$$

where T_{comm} is the wall time spent on the interprocessor communications, the acceleration factor is

$$q_{N_{pr}} \approx \frac{T_{A\chi}^1}{\frac{1}{N_{pr}-1}T_{A\chi}^1 + T_{comm}} \leq \frac{T_{A\chi}^1}{T_{comm}}.$$

It is therefore clear that for any number of processors N_{pr} the acceleration $q_{N_{pr}}$ cannot be more than $\frac{T_{A\chi}^1}{T_{comm}}$. This value depends on the size of 3D grid under consideration and the speed of communication of the particular cluster employed in the calculation. In order to try to reduce the effect of interprocessor communications we repeated the above experiments on a shared memory cluster.

2.1.3.2. Shared memory cluster

For our experiments we used a Linux shared memory cluster (Hamilton) managed by the ICHEC[1] project. In Figure 2.4 the acceleration factor $q_{N_{pr}}$ of equation 2.20 is presented. However, it should be understood that we did not have exclusive access to the cluster and the performance measurements are not very reliable. One factor affecting the performance is the current amount of users running their jobs. From the comparison of Figures 2.3 and 2.4 we see that the acceleration achieved on the

---

[1]Irish Centre for High-End Computing, http://www.ichec.ie/
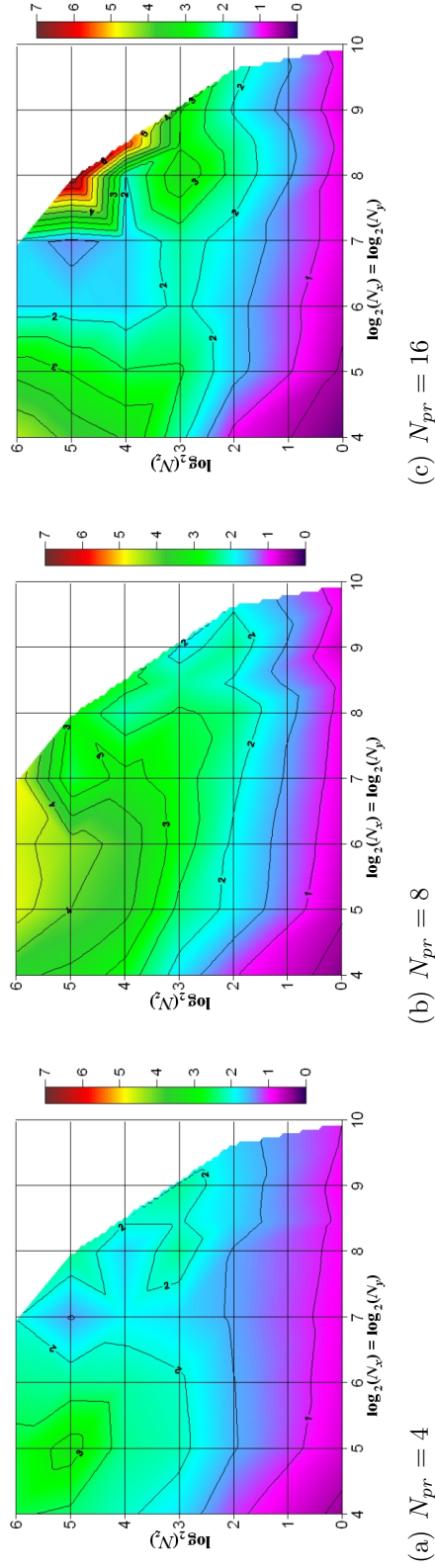
(a) $N_{pr} = 4$

(b) $N_{pr} = 8$

(c) $N_{pr} = 16$

Figure 2.4.: The results on the shared memory cluster (Hamilton). Factor $q_{N_{pr}}$ of equation 2.20 for $N_{pr} = 4, 8, 16$. The results are presented in bilogarithmic scale as a function of model sizes $N_x(= N_y)$ and N_z.

shared memory cluster is only slightly greater than that obtained on the distributed memory cluster. This is far from what might be anticipated and the reason for that is still unclear. One possible explanation is that the parallel implementation was written for a distributed memory cluster architecture and therefore transfers significant amount of data beetween different parts of the shared memory. Although this is considerably faster than transferring data over the network, a dedicated shared memory implementation, using OpenMP for example, could further enhance the performance.

In this section we have described the basic equations of the serial implementation for 3D EM forward modelling, based on the volume integral equation approach. The key time-consuming part of this serial solution is the discrete 2D convolution routine. We chose to parallelize this routine, since we demonstrated that another time-consuming part of the solution, calculation of the Green's matrices, takes much less wall time, especially for large-scale 3D models. To understand to what extend our parallel implementation improves performance of 3D EM forward modelling, we compared it with the serial *x3d* implementation by Avdeev *et al.* (1997, 2002). On both distributed and shared memory clusters, our parallel implementation allowed the solution to be reasonably accelerated. As an example, acceleration of 7 times was achieved with 16 processors for large models.

2.2. Optimization method

A large number of optimization methods for various applications, including geophysics, has been developed. A very good review of some of these methods can be found in Nocedal and Wright (1999). For large-scale nonlinear problems, such as 3D MT inversion, we shall minimize some objective functional using gradient based optimization techniques, including non-linear conjugate gradient (NLCG) and limited memory quasi-Newton schemes, because of their minimal storage requirements. In this work we chose a limited memory quasi-Newton method to be applied to solve our MT inverse problem.

2.2.1. General setting of EM inverse problem, as optimization problem

The EM inverse problem of equation 1.3b is usually solved by minimization, $\min_{\mathbf{m},\lambda}\varphi(\mathbf{m},\lambda)$, of the following objective function:

$$\varphi(\mathbf{m},\lambda) = \varphi_d(\mathbf{m}) + \lambda\varphi_s(\mathbf{m}), \qquad (2.21)$$

where

$$\varphi_d(\mathbf{m}) = \frac{1}{2}\left\|d^{obs} - F(\mathbf{m})\right\|^2 \qquad (2.22)$$

is the data misfit. Here $\mathbf{m} = (m_1,...,m_N)^T$ is the vector consisting of the model parameters; for EM applications this is usually vector consisting of the conductivities or log conductivities of the layers (for 1D case) or cells (for 3D case); superscript T means transpose; N is the number of model parameters; $F(\mathbf{m})$ is the solution of the forward mapping 1.2; d^{obs} is the observed data; and λ is the regularization parameter. As prescribed by the theory of Tikhonov (1963), the objective function in equation 2.21 has a regularization part (stabilizer) $\varphi_s(\mathbf{m})$. This stabilizer can be chosen in many ways (see, for example, Farquharson and Oldenburg (1998), and references therein), and moreover, the choice of $\varphi_s(\mathbf{m})$ influences the inversion result. Traditionaly, this stabilizer is chosen to obtain smooth models, however this remains a subjective matter. We will discuss our choices of the stabilizer in Sections 3.1.2 and 4.1.2.

In our inversion scheme we chose to use conductivities σ_k as the model parameters m_k, $(k = 1,...,N)$. Conductivity must be nonnegative, and usually lies in the range of 10^{-6} to 100 S/m (Simpson and Bahr, 2005), and hence, the optimization problem

given in equation 2.21 is subject to the bounds:

$$\mathbf{l} \leq \mathbf{m} \leq \mathbf{u}, \tag{2.23}$$

where $\mathbf{l} = (l_1, ..., l_N)^T$ and $\mathbf{u} = (u_1, ..., u_N)^T$ are the lower and upper bounds, respectively, $l_k \geq 0$ $(k = 1, ..., N)$.

An alternative way to keep the conductivities nonnegative is to define model parameters m_k as $m_k = \log(\sigma_k - l_k)$, or $m_k = \log\left(\frac{\sigma_k - l_k}{u_k - \sigma_k}\right)$. After such transformations, the bounds of the model parameters, m_k, extend to infinity, and the constrained problem of equations 2.21-2.23 nominally turns to an easier unconstrained problem. Although these transformations are commonly used, they may slow down the convergence of the solution if a minimum of the objective function of equation 4.1 is located on or near the bounds. However, a detailed study of the convergence of such an approach would require additional investigation.

The problem posed in equations 2.21-2.23 is a typical optimization problem with simple bounds (Nocedal and Wright, 1999). One possible method to solve this problem is quasi-Newton optimization.

2.2.2. Quasi-Newton optimization method

Quasi-Newton (QN) optimization methods have become very popular tools for the numerical solution of EM inverse problems (Newman and Boggs, 2004; Haber, 2005). The reason behind this is that the methods only require calculation of gradients and avoid the calculation of second-derivative terms. For large-scale inverse problems, such as the three-dimensional (3D) magnetotelluric (MT) inverse problem, limited memory QN methods are preferable, because their requirements for storage are not as excessive as for other QN methods. However, it should be understood that their small memory requirements are counterbalanced by slower convergence. Our inverse problem solution is based on a limited memory quasi-Newton method and we describe its implementation below; it is an extension of previous work by Ni and Yuan (1997). In contrast to this earlier work, we implement Wolfe conditions, given in equations 2.36 to terminate the line search procedure, as was recommended by Byrd *et al.* (1995).

We now present a general theory of QN optimization. This method operates similar to the other Newton-type methods that are also commonly applied to solve problem in equations 2.21-2.23. At each iteration step n, the Newton system of

linear equations

$$\mathbf{H}^{(n)}\mathbf{p}^{(n)} = -\mathbf{g}^{(n)} \tag{2.24}$$

is solved to find the search direction $\mathbf{p}^{(n)}$. It is desirable that the vector $\mathbf{p}^{(n)}$ is a descent direction, i.e. $\mathbf{g}^{(n)T}\mathbf{p}^{(n)} < 0$. In equation 2.24 the gradient

$$\mathbf{g} = \left(\frac{\partial \varphi}{\partial m_1}, ..., \frac{\partial \varphi}{\partial m_N} \right)^T \tag{2.25}$$

and the Hessian matrix

$$\mathbf{H} = \begin{pmatrix} \frac{\partial^2 \varphi}{\partial m_1 \partial m_1} & \cdots & \frac{\partial^2 \varphi}{\partial m_1 \partial m_N} \\ \cdots & \cdots & \cdots \\ \frac{\partial^2 \varphi}{\partial m_N \partial m_1} & \cdots & \frac{\partial^2 \varphi}{\partial m_N \partial m_N} \end{pmatrix} \tag{2.26}$$

are calculated at $\mathbf{m} = \mathbf{m}^{(n)}$. The next iterate $\mathbf{m}^{(n+1)}$ is then found as

$$\mathbf{m}^{(n+1)} = \mathbf{m}^{(n)} + \alpha^{(n)}\mathbf{p}^{(n)}, \tag{2.27}$$

where the step length $\alpha^{(n)}$ is computed by an inexact line search procedure.

The calculation and storage of the Hessian matrix $\mathbf{H}$ is a complex numerical problem. Fortunately, there is a group of Newton-type methods that avoids having to deal with the Hessian of equation 2.26, the so-called quasi-Newton (QN) methods. These methods require only the (multiple) calculation of the gradients of equation 2.25. For these methods, at each iteration step n the search direction $\mathbf{p}^{(n)}$ has the following form

$$\mathbf{p}^{(n)} = -\mathbf{G}^{(n)}\mathbf{g}^{(n)}, \tag{2.28}$$

where the symmetric matrix $\mathbf{G}^{(n)}$ is an approximation to the inverse Hessian matrix, $\mathbf{H}^{(n)-1}$, and is updated at every iteration. When the vector $\mathbf{p}^{(n)}$ is found from equation 2.28, and $\mathbf{G}^{(n)}$ is positive definite, one has

$$\mathbf{p}^{(n)T}\mathbf{g}^{(n)} = -\mathbf{g}^{(n)T}\mathbf{G}^{(n)}\mathbf{g}^{(n)} < 0, \tag{2.29}$$

and, hence, $\mathbf{p}^{(n)}$ is a descent direction. Even though we are guaranteed that the vector $\mathbf{p}^{(n)}$ is a descent direction as long as $\mathbf{G}^{(n)}$ is symmetric and positive definite, the convergence to the solution is better if $\mathbf{G}^{(n)}$ is a good approximation to the inverse of the Hessian. There are a variety of approaches that allow $\mathbf{G}^{(n)}$ to be calculated, one of them is the so-called Broyden-Fletcher-Goldfarb-Shanno formula

(Nocedal and Wright, 1999).

2.2.2.1. BFGS formula

According to the BFGS formula, at each iteration step n the approximation $\mathbf{G}^{(n)}$ is updated as

$$\mathbf{G}^{(n)} = \mathbf{V}^{(n-1)T}\mathbf{G}^{(n-1)}\mathbf{V}^{(n-1)} + \rho^{(n-1)}\mathbf{s}^{(n-1)}\mathbf{s}^{(n-1)T}, \tag{2.30}$$

where $\rho^{(n-1)} = \frac{1}{\mathbf{y}^{(n-1)T}\mathbf{s}^{(n-1)}}$,

$$\mathbf{G}^{(0)} = \mathbf{I}, \tag{2.31}$$

and

$$\mathbf{V}^{(n-1)} = \mathbf{I} - \rho^{(n-1)}\mathbf{y}^{(n-1)}\mathbf{s}^{(n-1)T}, \tag{2.32}$$

$$\mathbf{s}^{(n-1)} = \mathbf{m}^{(n)} - \mathbf{m}^{(n-1)}, \quad \mathbf{y}^{(n-1)} = \mathbf{g}^{(n)} - \mathbf{g}^{(n-1)}. \tag{2.33}$$

It follows from 2.30 that the matrix $\mathbf{G}^{(n)}$ satisfies the secant equation

$$\mathbf{G}^{(n)}\mathbf{y}^{(n-1)} = \mathbf{s}^{(n-1)}. \tag{2.34}$$

To explain the term "secant" let us, for simplicity, consider the case of only one model parameter ($N = 1$). In this case $\mathbf{G}^{(n)}$ is just a 1×1 matrix, and $\mathbf{m}$ and $\mathbf{g}$ are scalars. From 2.34, we can see that $\mathbf{G}^{(n)-1}$ approximates the slope of the gradient function $\mathbf{g}$ at point $\mathbf{m}^{(n)}$ by taking the secant through points $(\mathbf{m}^{(n-1)}, \mathbf{g}^{(n-1)})$ and $(\mathbf{m}^{(n)}, \mathbf{g}^{(n)})$. This means that $\mathbf{G}^{(n)}$ is an approximation of the inverse of the true Hessian $\mathbf{H}^{(n)}$ of equation 2.24. Moreover, when the vectors $\mathbf{s}^{(n-1)}$ and $\mathbf{y}^{(n-1)}$ satisfy the curvature condition

$$\mathbf{s}^{(n-1)T}\mathbf{y}^{(n-1)} > 0, \tag{2.35}$$

it can be easily shown that the matrix $\mathbf{G}^{(n)}$ is positive definite, as required by inequality 2.29 to guarantee the descent direction $\mathbf{p}^{(n)}$. However, the condition 2.35 does not always hold, and in such cases one needs to enforce 2.35 explicitly by imposing restrictions on step length $\alpha^{(n)}$ of equation 2.27. The condition 2.35 is guaranteed to hold if we impose the following Wolfe conditions

$$\varphi^{(n)} \leq \varphi^{(n-1)} + c_1\alpha^{(n-1)}\mathbf{g}^{(n-1)T}\mathbf{p}^{(n-1)}, \tag{2.36a}$$

$$\mathbf{g}^{(n)T}\mathbf{p}^{(n-1)} \geq c_2\mathbf{g}^{(n-1)T}\mathbf{p}^{(n-1)}, \tag{2.36b}$$

with $0 < c_1 < c_2 < 1$ (typical values for c_1 and c_2 are 10^{-4} and 0.9, respectively), where $\varphi^{(n)} = \varphi(\mathbf{m}^{(n)}, \lambda)$. To verify this statement we note that from equation 2.33 and condition 2.36b it follows that

$$\mathbf{g}^{(n)T}\mathbf{s}^{(n-1)} \geq c_2 \mathbf{g}^{(n-1)T}\mathbf{s}^{(n-1)},$$

and therefore,

$$\mathbf{y}^{(n-1)T}\mathbf{s}^{(n-1)} \geq (c_2 - 1)\alpha^{(n-1)}\mathbf{g}^{(n-1)T}\mathbf{p}^{(n-1)}.$$

Since $c_2 < 1$ and $p^{(n-1)}$ is a descent direction, the term on the right of the above inequality is positive, and the curvature condition 2.35 holds. A good illustration of the Wolfe conditions can be found in (p.37-41 Nocedal and Wright, 1999).

Unfortunately, the BFGS formula is not practically applicable to large-scale optimization problems, because matrix $\mathbf{G}^{(n)}$ is usually dense. Therefore the storage and computational requirements grow in proportion to N^2, and become excessive for large N. In order to circumvent this issue a limited memory QN methods must be applied.

2.2.2.2. L-BFGS formula

In accordance with the L-BFGS formula (Nocedal and Wright, 1999), the BFGS matrix $\mathbf{G}^{(n)}$ is approximated as

$$
\begin{aligned}
\mathbf{G}^{(n)} \approx \mathbf{G}_L^{(n)} &= \left(\mathbf{V}^{(n-1)T} \cdots \mathbf{V}^{(n-n_{cp})T}\right) \gamma^{(n)}\mathbf{I} \left(\mathbf{V}^{(n-n_{cp})} \cdots \mathbf{V}^{(n-1)}\right) \\
&+ \rho^{(n-n_{cp})} \left(\mathbf{V}^{(n-1)T} \cdots \mathbf{V}^{(n-n_{cp}+1)T}\right) \mathbf{s}^{(n-n_{cp})}\mathbf{s}^{(n-n_{cp})T} \left(\mathbf{V}^{(n-n_{cp}+1)} \cdots \mathbf{V}^{(n-1)}\right) \\
&+ \rho^{(n-n_{cp}+1)} \left(\mathbf{V}^{(n-1)T} \cdots \mathbf{V}^{(n-n_{cp}+2)T}\right) \mathbf{s}^{(n-n_{cp}+1)}\mathbf{s}^{(n-n_{cp}+1)T} \left(\mathbf{V}^{(n-n_{cp}+2)} \cdots \mathbf{V}^{(n-1)}\right) \\
&+ \cdots \\
&+ \rho^{(n-1)}\mathbf{s}^{(n-1)}\mathbf{s}^{(n-1)T},
\end{aligned}
$$

$$(2.37)$$

where $\gamma^{(n)} = \frac{\mathbf{s}^{(n-1)T}\mathbf{y}^{(n-1)}}{\mathbf{y}^{(n-1)T}\mathbf{y}^{(n-1)}}$, and stored implicitly using the n_{cp} correction pairs $\{\mathbf{s}^{(i)}, \mathbf{y}^{(i)} : i = n - n_{cp}, ..., n - 1\}$ given in equation 2.33. After the correction pair $\{\mathbf{s}^{(n)}, \mathbf{y}^{(n)}\}$ is computed, the oldest pair $\{\mathbf{s}^{(n-n_{cp})}, \mathbf{y}^{(n-n_{cp})}\}$ is deleted and replaced by this new pair. The main idea behind this approach is to use information from only the most recent iterations and the information from earlier iterations is discarded

in the interests of saving storage.

It can be shown that the matrix $\mathbf{G}_L^{(n)}$ also satisfies the secant equation 2.34 and, hence, all the above argumentation about $\mathbf{G}^{(n)}$ remains valid for $\mathbf{G}_L^{(n)}$.

2.2.2.3. Simple bounds constraints

In our case the problem is also subject to simple bounds defined in inequality 2.23. As it was proved above, the Wolfe conditions guarantee that the matrix $\mathbf{G}_L^{(n)}$ is positive definite and, hence, $\mathbf{p}^{(n)}$ is a descent direction. But condition 2.36b may not be reached inside the feasible region 2.23 and therefore the methods mentioned above may not work. If condition 2.36b does not hold, one should modify $\mathbf{s}^{(n-1)}$ of 2.33 as follows (Ni and Yuan, 1997)

$$\theta \mathbf{s}^{(n-1)} + (1 - \theta)\mathbf{G}_L^{(n-1)}\mathbf{y}^{(n-1)} \rightarrow \mathbf{s}^{(n-1)} \tag{2.38}$$

where $\theta = \begin{cases} 1, & \text{if } a \geq 0.2b \\ 0.8b/(b-a), & \text{otherwise} \end{cases}$, $a = \mathbf{s}^{(n-1)T}\mathbf{y}^{(n-1)}$, $b = \mathbf{y}^{(n-1)T}\mathbf{G}_L^{(n-1)}\mathbf{y}^{(n-1)}$.
Ni and Yuan (1997) proved that the transformation 2.38 guarantees that the matrix $\mathbf{G}_L^{(n)}$ is positive definite.

Alternative ways to deal with the bound constrained QN optimization can be found in Byrd *et al.* (1995) and Kelley (1999).

To conclude this section let us mention that the QN method described above does not depend on the dimensionality of the inverse problem. It can be equally applied to 1D, 2D or 3D cases. For the 1D case, m_i is the electrical conductivity of the ith layer, for 2D and 3D cases, it is the electrical conductivity of the ith cell.

2.3. Regularization

The inverse problem 2.21-2.23 is ill-posed, as it is illustrated in Figure 2.5. This means that (due to the fact that the EM inverse problem is nonlinear and data are limited and contaminated by noise) there are an infinite number of models that can equally fit the data within a given tolerance threshold, i.e. $\varphi_d(\mathbf{m}_1) \approx \varphi_d(\mathbf{m}_2)$, when $\|\mathbf{m}_1 - \mathbf{m}_2\| >> \|\mathbf{m}_1\|$.

One approach for narrowing down the set of solutions of the inverse problem is to introduce a regularization term in the objective function, as done in the objective
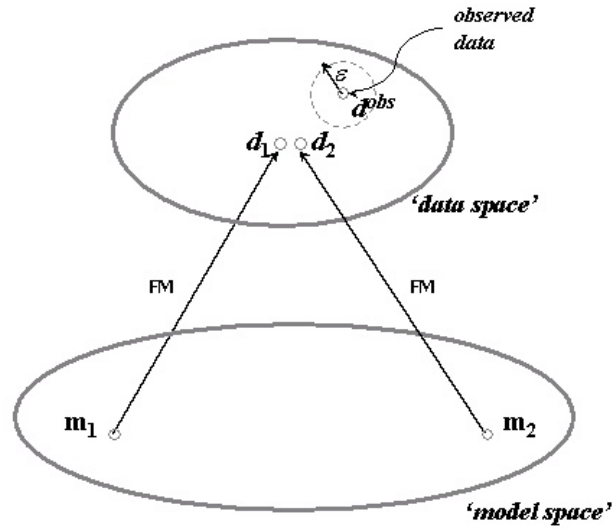
Figure 2.5.: Sensitivity of inverse mapping.

function of equation 2.21:

$$\varphi(\mathbf{m}, \lambda) = \varphi_d(\mathbf{m}) + \lambda \varphi_s(\mathbf{m}).$$

A possible way to construct the regularization term is to apply the following expression:

$$\varphi_s(\mathbf{m}) = \|\mathbf{W}\mathbf{m}\|^2 \tag{2.39}$$

This form usually forces the model $\mathbf{m}$ to be either:

1. the flattest that is still consistent with the data. This means that the first derivative of $\mathbf{m}$ is minimized, i.e. the matrix $\mathbf{W}$ is finite-difference approximation to the gradient operator,

2. the smoothest, but again consistent with the data, meaning that the second derivative of $\mathbf{m}$ is minimized, i.e. $\mathbf{W}$ represents the Laplacian,

or some combination of the above two. The explicit expressions for the regularization function φ_s, we used in our implementations, are described in Sections 3.1.2 and 4.1.2.

Chapter 3.

1D MT Inversion

In this chapter we apply the methods of Chapter 2 to a one-dimensional (1D) magnetotelluric (MT) inverse problem in order to test the optimization routines and determine suitable parameter values. Section 3.1 explains our setting of the 1D MT inverse problem. In Subsection 3.1.1 we present our calculation of gradients, which speeds up the inverse problem solution many times. In Subsection 3.1.2 we show a possible stabilizer for the 1D case together with an algorithm for choosing the regularization parameter λ. This regularization successfully stabilizes the QN inversion result. In Section 3.2 we demonstrate the efficiency of our inversion on a synthetic, but realistic, numerical example, along with a comparison with the limited memory Broyden-Fletcher-Goldfarb-Shanno algorithm for bound constrained optimization (L-BFGS-B) by Byrd *et al.* (1995). This comparison shows similar convergence rates. In addition, we show that it is sufficient to store only a few correction pairs to produce reasonable results. The study presented in this chapter is a first step towards the solution of large-scale electromagnetic problems, with a full treatment of the 3D conductivity structure of the Earth, and the results have been published in Avdeeva and Avdeev (2006).

3.1. Theory and basic equations

In the frame of one-dimensional magnetotelluric inversion we assume a layered earth model and seek the conductivities of those layers. As mentioned in the previous chapter, this problem is usually solved by minimization $\min_{\mathbf{m},\lambda}\varphi(\mathbf{m}, \lambda)$ of the following objective function:

$$\varphi(\mathbf{m}, \lambda) = \varphi_d(\mathbf{m}) + \lambda\varphi_s(\mathbf{m}) \tag{3.1}$$

For the 1D MT case the data misfit has the following form

$$\varphi_d(\mathbf{m}) = \frac{1}{2} \sum_{j=1}^{N_T} \beta_j \left| Z_j\left(\boldsymbol{\sigma}(\mathbf{m})\right) - D_j \right|^2. \tag{3.2}$$

Here $\boldsymbol{\sigma} = (\sigma_1, ..., \sigma_N)^T$ is the vector consisting of the electrical conductivities of the layers; $\mathbf{m} = (m_1, ..., m_N)^T$ is the vector of model parameters, such that

$$m_k = \sigma_k / \sigma_k^{(0)}, (k = 1, ..., N); \tag{3.3}$$

$\boldsymbol{\sigma}^{(0)}$ is an initial guess conductivity model; superscript T means transpose; N is the number of layers; $Z_j(\boldsymbol{\sigma})$ and D_j are the complex-valued, modeled, and observed impedances at the jth period $(j = 1, ..., N_T)$, respectively;

$$\beta_j = \frac{1}{N_T} \frac{2}{\varepsilon_j^2 \left| D_j \right|^2} \tag{3.4}$$

are positive weights. In definition 3.4 ε_j are the user-estimated relative errors of the impedance D_j. We will call these errors ε_j the noise floor. A large noise floor corresponds to bad quality MT data.

There are two reasons for the form 3.4 for the weights β_j: first, to be able to equally fit the impedances at all frequencies or choose the frequencies, which are important for a particular case and put large errors ε_j for the others, and second, to know to what level we should minimize our data misfit φ_d, in order not to overfit the data. For example, we should not minimize the data misfit to a level lower than 1, if our data has noise of ε_j.

Since the conductivities σ_k $(k = 1, ..., N)$ must be nonnegative and reasonable, the optimization problem given in equation 3.1 is subject to bounds:

$$\mathbf{l} \leq \boldsymbol{\sigma} \leq \mathbf{u}, \tag{3.5}$$

where $\mathbf{l} = (l_1, ..., l_N)^T$ and $\mathbf{u} = (u_1, ..., u_N)^T$ are the lower and upper bounds, respectively, $l_k \geq 0$.

To solve the problem posed in equations 3.1-3.5 we use the limited memory QN method described in Chapter 2. An essential difficulty of this optimization method is the calculation of derivatives $\partial \varphi_d / \partial m_k$ as given in equation 2.25. Taking in mind

equation 3.3, we see that

$$\frac{\partial \varphi_d}{\partial m_k} = \frac{\partial \varphi_d}{\partial \sigma_k} \sigma_k^{(0)}. \tag{3.6}$$

3.1.1. Calculation of derivatives $\frac{\partial \varphi_d}{\partial \sigma_k}$

A straightforward numerical calculation of the derivatives by finite differences

$$\frac{\partial \varphi_d}{\partial \sigma_k} \approx \frac{\varphi_d(\sigma_1, \ldots, \sigma_k + \delta\sigma_k, \ldots, \sigma_N) - \varphi_d(\sigma_1, \ldots, \sigma_k, \ldots, \sigma_N)}{\delta\sigma_k} \tag{3.7}$$

involves at least $N + 1$ solutions of the forward problem. However, for large-scale problems, when N is large, such a straightforward calculation may be prohibitive in terms of computational time. In addition, the selection of the increment $\delta\sigma_k$ is not easy in order to ensure numerical stability, and usually few increments should be tried. One can significantly speed up the inverse problem solution by avoiding this straightforward calculation, given in formula 3.7.

Our approach for calculating the derivatives exploits the Green's function technique and requires time equal to the time of the solution of two forward problems, rather than $N + 1$ forward problems.

To derive the derivatives $\frac{\partial \varphi_d}{\partial \sigma_k}$ let us first rewrite equation 3.2 as

$$\varphi_d(\boldsymbol{\sigma}) = \frac{1}{2} \langle \mathbf{Z} - \mathbf{D}, \mathbf{Z} - \mathbf{D} \rangle_2, \tag{3.8}$$

where we introduce the vectors $\boldsymbol{\sigma} = (\sigma_1, ..., \sigma_N)^T$, $\mathbf{Z} = (Z_1, ..., Z_{N_T})^T$, and $\mathbf{D} = (D_1, ..., D_{N_T})^T$ and an inner product $\langle \cdot, \cdot \rangle_2$ of vectors $\mathbf{a}$ and $\mathbf{b}$ as

$$\langle \mathbf{a}, \mathbf{b} \rangle_2 = \sum_{j=1}^{N_T} \beta_j \bar{a}_j b_j. \tag{3.9}$$

From equations 3.8 and 3.9, it follows that

$$\begin{aligned}
\frac{\partial \varphi_d}{\partial \sigma_k} &= \frac{1}{2} \sum_{j=1}^{N_T} \beta_j \left\{ \frac{\overline{\partial(Z_j - D_j)}}{\partial \sigma_k}(Z_j - D_j) + \overline{\frac{\partial(Z_j - D_j)}{\partial \sigma_k}}(Z_j - D_j) \right\} \\
&= \Re \left\langle \mathbf{Z} - \mathbf{D}, \frac{\partial \mathbf{Z}}{\partial \sigma_k} \right\rangle_2.
\end{aligned} \tag{3.10}$$

The main problem now is how to calculate the derivatives $\frac{\partial \mathbf{Z}}{\partial \sigma_k}$. From Maxwell's equations written for a layered earth (see Appendix A), it follows that at any depth

z, the impedance can be derived as

$$Z_j(z) = \frac{i\omega_j\mu_0 v_j}{\partial_z v_j},$$ (3.11)

where $v_j(z)$ satisfies the Helmholtz equation

$$\partial_z^2 v_j + i\omega_j\mu_0\sigma(z)v_j = 0,$$ (3.12)

and the boundary condition $v_j \underset{z\to\infty}{\to} 0$. Here, $\omega_j = 2\pi/T_j$ is the jth angular frequency, and μ_0 is the magnetic permeability of free space. Further, for a layered earth we easily may decompose $\sigma(z)$ as

$$\sigma(z) = \sum_{k=1}^{N} \sigma_k\chi_k(z),$$ (3.13)

where σ_k is the conductivity of the kth layer confined between boundaries z_k and z_{k+1}, and the boxcar function $\chi_k(z) = \theta(z - z_k) - \theta(z - z_{k+1})$, where $\theta(z)$ is the Heaviside function. Note that in equation 3.13 we assume that $z_{N+1} = \infty$. From equations 3.12 and 3.13 it follows that

$$\partial_z^2\frac{\partial v_j}{\partial\sigma_k} + i\omega_j\mu_0\sigma(z)\frac{\partial v_j}{\partial\sigma_k} = -i\omega_j\mu_0\chi_k(z)v_j.$$ (3.14)

From equation 3.14, it follows that the derivative $\frac{\partial v_j}{\partial\sigma_k}$ is expressed as

$$\frac{\partial v_j}{\partial\sigma_k} = -\int G_j(z,\zeta)\chi_k(\zeta)v_j(\zeta)d\zeta = -\int_{z_k}^{z_{k+1}} G_j(z,\zeta)v_j(\zeta)d\zeta,$$ (3.15)

where the Green's function is a solution to the following equation:

$$\partial_z^2 G_j(z,\zeta) + i\omega_j\mu_0\sigma(z)G_j(z,\zeta) = i\omega_j\mu_0\delta(z - \zeta),$$ (3.16)

and where $\delta(z)$ is the delta-function. From equation 3.11 it follows that

$$\frac{\partial Z_j}{\partial\sigma_k}(z) = Z_j\left(\frac{1}{v_j}\frac{\partial v_j}{\partial\sigma_k} - \frac{1}{\partial_z v_j}\partial_z\frac{\partial v_j}{\partial\sigma_k}\right).$$ (3.17)

Substituting equation 3.15 into equation 3.17 (and assuming $z = 0$) yields

$$
\frac{\partial Z_j}{\partial \sigma_k}(0) = Z_j(0) \left(-\frac{1}{v_j(0)} \int_{z_k}^{z_{k+1}} G_j(0, \zeta) v_j(\zeta) d\zeta \right.
$$
$$
\left. + \frac{1}{\partial_z v_j|_{z=0}} \int_{z_k}^{z_{k+1}} \partial_z G_j(z, \zeta)|_{z=0} v_j(\zeta) d\zeta \right). \tag{3.18}
$$

Using the following properties of $G_j(z, \zeta)$ (at $z < \zeta$) (Avdeev *et al.*, 1997):

$$
\partial_z G_j(z, \zeta) = i\omega_j \mu_0 \frac{1}{Z_j^*(z)} G_j(z, \zeta), \tag{3.19}
$$

$$
G_j(z, \zeta) = \frac{1}{Z_j^{-1}(z) - Z_j^{*-1}(z)} \gamma_j(z, \zeta), \tag{3.20}
$$

where

$$
\gamma_j(z, \zeta) = \exp\left(i\omega_j \mu_0 \int_z^\zeta Z_j^{-1}(\zeta) d\zeta \right), \tag{3.21}
$$

and $Z_j^*(z)$ is the impedance of the layered earth model above the depth z, from equation 3.18 we derive that

$$
\begin{aligned}
\frac{\partial Z_j}{\partial \sigma_k}(0) &= Z_j(0) \left(-\frac{1}{v_j(0)} + \frac{i\omega\mu_0 Z_j^{*-1}(0)}{\partial_z v_j|_{z=0}} \right) \frac{1}{Z_j^{-1}(0) - Z_j^{*-1}(0)} \int_{z_k}^{z_{k+1}} \gamma_j(0, \zeta) v_j(\zeta) d\zeta \\
&\overset{3.11}{=} -Z_j(0) \frac{i\omega\mu_0}{\partial_z v_j|_{z=0}} \int_{z_k}^{z_{k+1}} \gamma_j(0, \zeta) v_j(\zeta) d\zeta \overset{3.11}{=} -Z_j^2(0) \int_{z_k}^{z_{k+1}} \gamma_j(0, \zeta) \frac{v_j(\zeta)}{v_j(0)} d\zeta \\
&= -Z_j^2(0) \int_{z_k}^{z_{k+1}} \gamma_j^2(0, \zeta) d\zeta. \tag{3.22}
\end{aligned}
$$

To obtain equation 3.22 we also used the fact that

$$
\gamma_j(0, \zeta) \overset{3.21,3.11}{=} \exp\left(\int_0^\zeta \frac{\partial_z v_j|_{z=\zeta}}{v_j(\zeta)} d\zeta \right) = \frac{v_j(\zeta)}{v_j(0)}
$$

Substituting equation 3.22 in equation 3.10 yields the desired derivatives

$$
\frac{\partial \varphi_d}{\partial \sigma_k} = -\Re\left(\sum_{j=1}^{N_T} \beta_j \Gamma_{kj} \left(\overline{Z}_j - \overline{D}_j \right) Z_j^2 \right), \tag{3.23}
$$

where for simplicity we denoted $Z_j = Z_j(0)$, and

$$\Gamma_{kj} = \int_{z_k}^{z_{k+1}} \gamma_j^2(0, \zeta) d\zeta \ (k = 1, ..., N). \tag{3.24}$$

Let us now derive an explicit expression for the coefficients Γ_{kj}.

3.1.1.1. Calculation of Γ_{kj}

By definition (see equation 3.24 and 3.21)

$$\Gamma_{kj} = \int_{z_k}^{z_{k+1}} \gamma_j^2(0, \zeta) d\zeta \ (k = 1, ..., N),$$

where

$$\gamma_j(z, \zeta) = \exp\left(i\omega_j \mu_0 \int_z^\zeta Z_j^{-1}(\zeta) d\zeta\right).$$

From these two equations it follows that

$$
\begin{aligned}
\Gamma_{kj} &= \int_{z_k}^{z_{k+1}} \left[\exp\left(i\omega_j \mu_0 \sum_{l=1}^{k-1} \int_{z_l}^{z_{l+1}} Z_j^{-1}(\zeta) d\zeta + i\omega_j \mu_0 \int_{z_k}^{\zeta} Z_j^{-1}(\zeta) d\zeta\right)\right]^2 d\zeta \\
&= \left(\prod_{l=1}^{k-1} \gamma_j^2(z_l, z_{l+1})\right) \gamma_{kj},
\end{aligned} \tag{3.25}
$$

where

$$\gamma_{kj} = \int_{z_k}^{z_{k+1}} \gamma_j^2(z_k, \zeta) d\zeta. \tag{3.26}$$

In the above expressions, we assumed that $z_1 = 0$ and $z_{N+1} = \infty$. From equation 3.25 it follows that the coefficients Γ_{kj} can be calculated recursively as

$$\Gamma_{k+1j} = \gamma_j^2(z_k, z_{k+1}) \frac{\gamma_{k+1j}}{\gamma_{kj}} \Gamma_{kj}, \tag{3.27}$$

where $\Gamma_{1j} = \gamma_{1j}$ as can be seen from equations 3.25 and 3.26. From equations 3.11, 3.12 and the definition given by equation 3.21, it follows that

$$\gamma_j(z_k, \zeta) = \cosh\left(\kappa_{kj}(\zeta - z_k)\right) + \lambda_{kj} \sinh\left(\kappa_{kj}(\zeta - z_k)\right), (z_k \leq \zeta \leq z_{k+1}), \tag{3.28}$$

40

where $\kappa_{kj} = \sqrt{-i\omega\mu_0\sigma_k}$ and

$$\lambda_{kj} = \frac{i\omega\mu_0}{\kappa_{kj}} Z_j^{-1}(z_k). \tag{3.29}$$

From equations 3.11 and 3.12 and the definition given by equation 3.29, the following recursive formula follows

$$\lambda_{kj} = \begin{cases} \dfrac{-\sinh(\Delta_k\kappa_{kj}) + \cosh(\Delta_k\kappa_{kj})\frac{\kappa_{k+1j}}{\kappa_{kj}}\lambda_{k+1j}}{\cosh(\Delta_k\kappa_{kj}) - \sinh(\Delta_k\kappa_{kj})\frac{\kappa_{k+1j}}{\kappa_{kj}}\lambda_{k+1j}}, & k = N-1, ..., 1 \\ -1, & k = N \end{cases} \tag{3.30}$$

This formula can also be easily obtained from definition 3.29 and the recursive formula for the 1D impedance A.9, explicitly derived in Appendix A.

From equation 3.28 it also follows that

$$\gamma_j(z_k, z_{k+1}) = \cosh(\Delta_k\kappa_{kj}) + \lambda_{kj}\sinh(\Delta_k\kappa_{kj}). \tag{3.31}$$

Finally, substituting equation 3.28 into equation 3.26, and after some manipulation, one obtains

$$\gamma_{kj} = \begin{cases} \Delta_k \left(\frac{1-\lambda_{kj}^2}{2} + \frac{\sinh(\Delta_k\kappa_{kj})}{\Delta_k\kappa_{kj}} \cdot \right. \\ \left. \left[\frac{(1+\lambda_{kj})^2}{2}\cosh(\Delta_k\kappa_{kj}) + \lambda_{kj}\sinh(\Delta_k\kappa_{kj}) \right] \right), & k = N-1, ..., 1 \\ \frac{1}{2\kappa_{kj}}, & k = N \end{cases} \tag{3.32}$$

The expressions presented in equations 3.31 and 3.32 permit the recursive calculation of the coefficients Γ_{kj} using equation 3.27. Comparing equations 3.30-3.32, one can see that the coefficients λ_{kj}, γ_{kj}, and $\gamma_j(z_k, z_{k+1})$ are calculated simultaneously while moving from the bottom of the model to the surface. Such a calculation is somewhat equivalent to the forward problem solution. Once the coefficients γ_{kj} and $\gamma_j(z_k, z_{k+1})$ are found, the Γ_{kj} required by the derivatives defined in equation 3.23 are calculated recursively from the surface to the bottom using equation 3.27. Thus the time to calculate the derivatives of equation 3.23 is not more than twice that required for the forward problem solution (calculating λ_{kj} alone).

It is important to mention that the derivatives $\partial\varphi_d/\partial\sigma_k$ can also be calculated using the chain-rule (e.g. Constable *et al.*, 1987), which is based on the differentiation of an analytical solution to a 1D forward problem.

3.1.2. Regularization technique

In our 1D implementation the regularized part (stabilizer) φ_s introduced earlier in equation 3.1 has the following form:

$$\varphi_s(\mathbf{m}) = \sum_{k=2}^{N} (m_k - m_{k-1})^2 \tag{3.33}$$

where $\mathbf{m} = (m_1, ..., m_N)^T$ and model parameters m_k are given by equation 3.3.

3.1.2.1. Choice of parameter λ

When we use any stabilizer φ_s we encounter the additional problem of finding the regularization parameter λ. We know that the solution of underdetermined ($M \ll N$) inverse problems very much depends on the choice of parameter λ (Farquharson and Oldenburg, 1998). A large value of λ may lead to a model that is extremely smooth, whereas a value of λ that is small may deliver a model with oscillating conductivity values. In this study, we applied a simple cooling-type approach that comprises two stages. First, we find two values λ_{low} and λ_{high} such that $\varphi_d(\mathbf{m}^{\lambda_{\mathrm{low}}}) < 1$, and $\varphi_d(\mathbf{m}^{\lambda_{\mathrm{high}}}) > 1$, where $\mathbf{m}^\lambda$ delivers the solution of $\min_{\mathbf{m}} \varphi(\mathbf{m}, \lambda)$, with the parameter λ. To do this we solve the inverse problem posed in equations 3.1-3.5 for different values of λ. As prescribed by the cooling approach, we start this process with a large value of the parameter λ. Note that the weight coefficients β_j $j = 1, ..., N_T$ of the misfit φ_d are chosen so that the value $\varphi_d = 1$ exactly corresponds to the noise floor (see page 36). In the second stage, we find the biggest possible λ_{opt} such that $\varphi_d(\mathbf{m}^{\lambda_{\mathrm{opt}}}) \leq 1$, where $\mathbf{m}^{\lambda_{\mathrm{opt}}}$ is a solution of $\min_{\mathbf{m}} \varphi(\mathbf{m}, \lambda_{\mathrm{opt}})$. To find such a value λ, we iteratively apply the linear interpolation of $\phi(\lambda) = \varphi_d(\mathbf{m}^\lambda)$ at the segment $[\lambda_{\mathrm{low}}, \lambda_{\mathrm{high}}]$. This approach is a simple variant of an algorithm by Haber and Oldenburg (1997). It should be understood, however, that it does not make sense to fine tune the regularization parameter λ, following our procedure, if the noise floor cannot be estimated reliably. In the numerical examples presented below, we demonstrate that our procedure works successfully for the case of a slightly overestimated noise floor.

3.2. Model study

We demonstrate on a synthetic example the extent to which the calculation of the derivatives given by equation 3.6 presented in Section 3.1.1 accelerates the solution of the inverse problem. A seven-layered earth model is given in Table 3.1. This

Conductivity [S/m]	Thickness [km]
0.01	64
0.05	180
0.1	150
0.12	126
0.28	130
1.1	150
1.5	

Table 3.1.: A seven-layered earth model

model was compiled from the models derived from a seafloor MT and a global GDS long-period data set collected in the North Pacific Ocean (see Avdeev *et al.*, 2004). To complicate the inversion process, we subdivided the three upper layers in this model (to a depth of 394 km) into 197 sublayers of equal thickness. This means that we deliberately overparametrized the problem. For this 201-layered ($N = 201$) model, we inverted the impedance $D_j = Z_j(\mathbf{m})$, calculated at $N_T = 30$ periods, from 10 s to 10,800 s. In addition, we added 0.5% random noise to the impedance data. This is a realistic noise level for very good quality MT data. The relative error ε_j of equation 3.4 was taken as 0.01, which means that the noise floor is slightly overestimated and should lead to a smoother result. A 10 Ωm uniform half-space was used as an initial guess model.

In Figure 3.1(a), we compare the convergence rates of two solutions obtained with straightforward calculation of the derivatives (see formula 3.7) and using the method presented in Section 3.1.1, respectively. The curves are shown as a function of the number of evaluations of $\varphi(\mathbf{m}, \lambda)$ for two cases, $\lambda = 0$ and $\lambda_{\mathrm{opt}} = 320$. From Figure 3.1(a), it is seen that the calculation of the derivatives given in Section 3.1.1 accelerates the solution by 130 times. The results of the inversion are presented in 3.1(b). As might be expected, the conductivity models recovered do not fit well for depths greater than 400 km because the responses at the periods considered are almost insensitive to these depths.

(a)

(b)
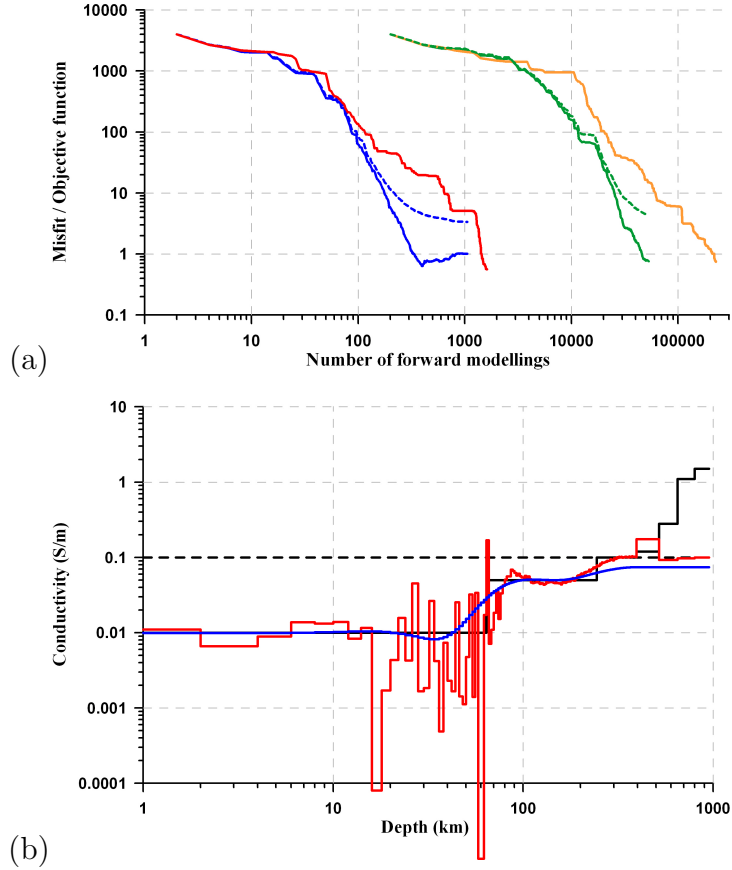
Figure 3.1.: (a) Comparison of convergence rates: The curves present the misfit of equation 3.2 obtained with the straightforward calculation of the derivatives shown for $\lambda = 0$ (amber) and $\lambda_{\mathrm{opt}} = 320$ (green). The green dashed line presents the objective function of equation 3.1 for $\lambda_{\mathrm{opt}} = 320$. The same is shown with the calculation of the derivatives that is presented in Section 3.1.1, for $\lambda = 0$ (red) and $\lambda_{\mathrm{opt}} = 320$ (blue solid and dashed lines). (b) The conductivity models obtained with the calculation of the derivatives as presented in Section 3.1.1: for $\lambda = 0$ (red) and $\lambda_{\mathrm{opt}} = 320$ (blue). The solid and dashed black lines show the true and initial guess models, respectively.

In our next example (Figure 3.2), we study the convergence rate of our solution for various numbers n_{cp} of correction pairs. Let us remind here that every iteration n a pair of vectors $\{\mathbf{s}^{(n)}, \mathbf{y}^{(n)}\}$ is calculated. This pair is called a correction pair. The optimization method requires to store these pairs only from n_{cp} previous iterations. So the information from only the most recent iterations is stored and information from the previous iterations is discarded in the interest of saving storage. The number n_{cp} is defined by user and depends on the amount of available memory. The

curves in Figure 3.2(a) are shown as a function of n_{fg}. This number, n_{fg}, is the number of evaluations of objective function $\varphi(\mathbf{m}, \lambda_{\mathrm{opt}})$ together with its gradient $(\partial\varphi/\partial m_1, ..., \partial\varphi/\partial m_N)^T|_{\mathbf{m},\lambda_{\mathrm{opt}}}$ and is equal to or a little bit larger than the number of QN iterations, n_{it}, since the method might need few steps within the line search procedure.

We can see that for all the n_{cp} numbers considered we get very similar resulting models (see Figure 3.2(b)). For $n_{cp} = 2$ the convergence is worse than for all other n_{cp} numbers (see Figure 3.2(a)). It is surprising that such a small number of pairs $(n_{cp} = 5)$ can be sufficient to get a relatively good convergence and a reasonable result.

(a)

(b)
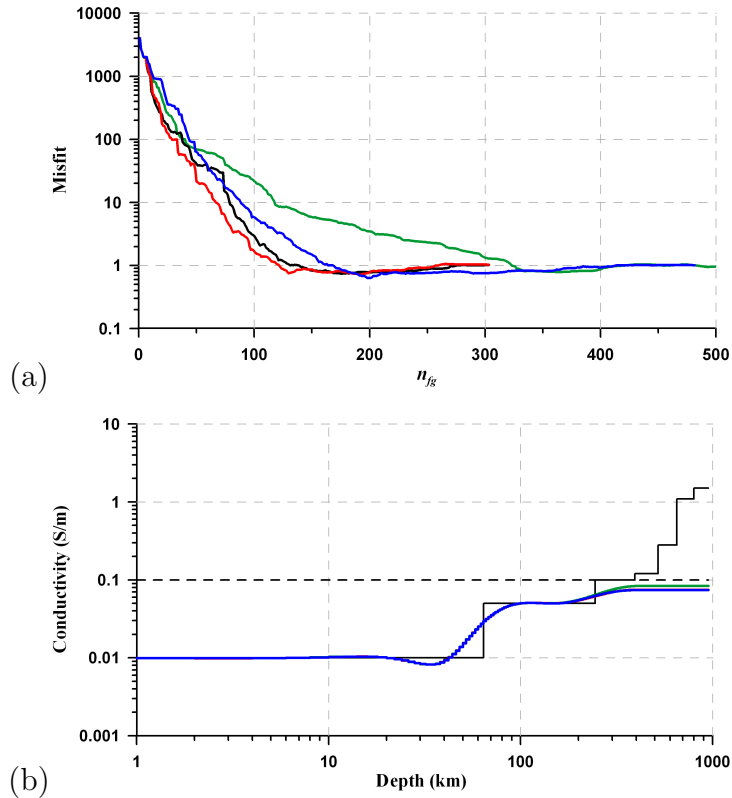
Figure 3.2.: Comparison for different numbers of correction pairs (n_{cp}). (a) The convergence rate for $n_{cp} = 2$ (green), $n_{cp} = 5$ (blue), $n_{cp} = 20$ (red) and $n_{cp} = 25$ (black). (b) The corresponding conductivity models, which are plotted mostly on top of each other. The solid and dashed black lines show the true and initial guess models, respectively.

In Figure 3.3, we present the third example – a comparison of two different solutions. The first solution is based on the optimization method offered in previous

chapter, and the second one uses the L-BFGS-B optimization code by Byrd *et al.* (1995). The comparison is presented for $n_{cp} = 5$ correction pairs and $\lambda_{\mathrm{opt}} = 320$. These solutions converge in a similar way and produce similar models. In the same figure we show the curves produced using the conventional QN algorithm of Gill *et al.* (1981), subject to simple bounds. To find the search direction $\mathbf{p}^{(n)}$, this algorithm solves the Newton system $\mathbf{H}^{(n)}\mathbf{p}^{(n)} = -\mathbf{g}^{(n)}$, rather than making use of equation $\mathbf{p}^{(n)} = -\mathbf{G}^{(n)}\mathbf{g}^{(n)}$ (see equation 2.28), and it is mostly suitable for small-scale problems.

(a)

(b)
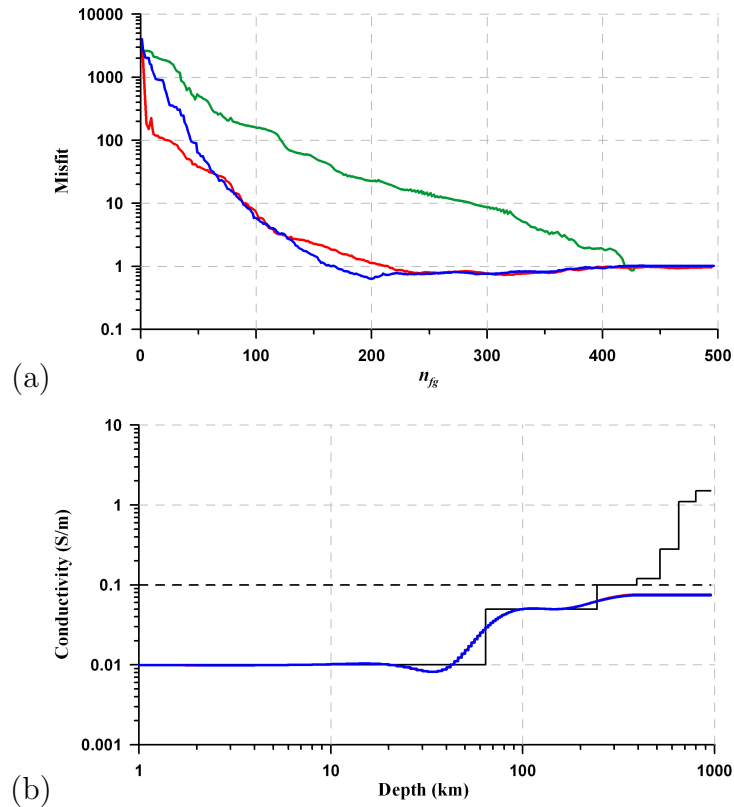
Figure 3.3.: Comparison of three different QN methods. (a) The convergence rate for inversions, which uses the approach presented in Chapter 2 (blue line), L-BFGS-B algorithm (red) and QN algorithm by Gill *et al.* (1981) (green). (b) The corresponding conductivity models, which are plotted on top of each other. The solid and dashed black lines show the true and initial guess models, respectively.

3.3. Conclusions

In this chapter we describe a limited memory QN method applied to solve the 1D MT inverse problem. In the numerical examples presented, we demonstrate that our method for the calculation of derivatives (see 3.1.1) dramatically accelerates the problem solution. The nontrivial problem of such a calculation of derivatives in the 3D MT case is presented in the next chapter. We also describe the regularization procedure and propose a method for finding an optimal regularization parameter, λ_{opt}. This procedure is useful in cases where the noise floor is roughly known and we demonstrate that it works successfully on numerical examples. Another finding of our numerical experiments is that we can find a reasonable solution to the inverse problem with a surprisingly small number of correction pairs ($n_{cp} = 5$). We also demonstrate that the solution, based on method described in Chapter 2, converges similarly to the solution based on the L-BFGS-B method.

Chapter 4.

3D MT Inversion

In this chapter we describe how we apply the limited memory quasi-Newton optimization method to develop a novel fully three-dimensional magnetotelluric inversion technique. The inversion involves all four entries of the MT impedance matrix and we employ the integral equation forward modelling code *x3d* by Avdeev *et al.* (1997, 2002), briefly described in Section 2.1, as an engine for this inversion.

In Section 4.1 we first briefly describe the setting of the inverse problem, as well as some key features of our implementation. In Subsection 4.1.1, we develop the theory and basic equations for the calculation of the derivatives of the data misfit, our theory is based on the known adjoint approach (Rodi, 1976; Rodi and Mackie, 2001; Chen *et al.*, 2005). Then, we demonstrate that the calculation of the derivatives, at a given period, is equivalent to only two forward modellings. Usage of this adjoint approach dramatically accelerates the inversion. In Section 4.2 we demonstrate how our inversion works in practice (in terms of the convergence, performance and accuracy) on synthetic, but realistic numerical examples. One of the examples (Subsection 4.2.2) includes a tilted conductive dyke in a uniform half-space (Zhdanov and Tolstaya, 2004). Another example is more complex, involving a model with resistive and conductive adjacent blocks buried in a two-layered earth (Subsection 4.2.4). Both models have also been used to test other forward and inverse codes. The results presented in this chapter are encouraging and suggest that the solution developed in this work can be successfully applied to 3D inverse problems with measured MT data.

4.1. Theory and basic equations

Let us consider a 3D earth conductivity model discretized by N cells, such that $\sigma(\mathbf{r}) = \sum_{k=1}^{N} \sigma_k \chi_k(\mathbf{r})$, where $\chi_k(\mathbf{r}) = \begin{cases} 1, \mathbf{r} \in V_k \\ 0, \mathbf{r} \notin V_k \end{cases}$, V_k is the volume occupied by the kth cell and $\mathbf{r} = (x, y, z)$. In the frame of 3D MT inversion, we seek the conductivities σ_k $(k = 1, ..., N)$ of the cells. This is again - as in the previous chapter - a typical optimization problem, such that $\varphi(\boldsymbol{\sigma}, \lambda) \underset{\boldsymbol{\sigma}, \lambda}{\rightarrow} \min$, with a penalty function φ given as

$$\varphi(\boldsymbol{\sigma}, \lambda) = \varphi_d(\boldsymbol{\sigma}) + \lambda \varphi_s(\boldsymbol{\sigma}). \tag{4.1}$$

As in the previous chapter, the first term, $\varphi_d(\boldsymbol{\sigma})$, is the data misfit and serves to ensure that our recovered model matches the observed data. The second term in equation 4.1, $\varphi_s(\boldsymbol{\sigma})$, is a Tikhonov-type stabilizer (Tikhonov, 1963); λ is the regularization parameter that balances the effect of data misfit and model regularization during minimization. The stabilizer φ_s can be chosen in many different ways. This aspect of the problem is discussed in Subsection 4.1.2.

For the 3D MT case the data misfit $\varphi_d(\boldsymbol{\sigma})$ has the following form

$$\varphi_d = \frac{1}{2} \sum_{i=1}^{N_S} \sum_{j=1}^{N_T} \beta_{ij} tr[\overline{\mathbf{A}}_{ij}^T \mathbf{A}_{ij}] \tag{4.2}$$

Here N_S is the number of MT sites $\mathbf{r}_i = (x_i, y_i, z = 0)$, where $i = 1, ..., N_S$; N_T is the number of the frequencies ω_j, where $j = 1, ..., N_T$; the 2×2 matrices $\mathbf{A}_{ij}$ are defined as $\mathbf{A}_{ij} = \mathbf{Z}_{ij} - \mathbf{D}_{ij}$, where $\mathbf{Z}_{ij} = \begin{pmatrix} Z_{xx} & Z_{xy} \\ Z_{yx} & Z_{yy} \end{pmatrix}_{ij}$ and $\mathbf{D}_{ij} = \begin{pmatrix} D_{xx} & D_{xy} \\ D_{yx} & D_{yy} \end{pmatrix}_{ij}$ are matrices of the complex-valued predicted $\mathbf{Z}(\mathbf{r}_i, \omega_j)$ and observed $\mathbf{D}(\mathbf{r}_i, \omega_j)$ impedances, respectively;

$$\beta_{ij} = \frac{1}{N_S N_T} \frac{2}{\varepsilon_{ij}^2 tr \left[\overline{\mathbf{D}}_{ij}^T \mathbf{D}_{ij} \right]} \tag{4.3}$$

are the positive weights, where ε_{ij} is the relative error of the observed impedance $\mathbf{D}_{ij}(\boldsymbol{\sigma})$. The sign $tr[\cdot]$ introduced above means the trace of its matrix argument, which is defined as $tr[\mathbf{B}] = B_{xx} + B_{yy}$, for any $\mathbf{B} = \begin{pmatrix} B_{xx} & B_{xy} \\ B_{yx} & B_{yy} \end{pmatrix}$. The question of why the form of equation 4.2 was chosen to represent a measure of misfit is discussed in Appendix C. In addition, a more generalized form of this equation is considered in Appendix D.

An alternative way for constructing data misfit φ_d would be to treat the individual entries of the impedance separately.

Again, the conductivities σ_k $(k = 1, ..., N)$ must be nonnegative and realistic and, hence, the optimization problem 4.1 is subject to the bounds

$$\mathbf{l} \leq \boldsymbol{\sigma} \leq \mathbf{u}, \tag{4.4}$$

where $\mathbf{l} = (l_1, ..., l_N)^T$ and $\mathbf{u} = (u_1, ..., u_N)^T$ are the lower and upper bounds, respectively, and $l_k \geq 0$, $(k = 1, ..., N)$.

To solve the problem posed in equations 4.1-4.4 we use the limited memory QN method described in Chapter 2. We assume that

$$m_k = \sigma_k / \sigma_k^{(0)}, \tag{4.5}$$

where $\sigma_k^{(0)}$ is the conductivity of k-th cell for an initial guess model. As for the 1D case considered above, the essential difficulty of the 3D solution is the calculation of derivatives

$$\frac{\partial \varphi_d}{\partial m_k} = \frac{\partial \varphi_d}{\partial \sigma_k} \sigma_k^{(0)} \tag{4.6}$$

4.1.1. Calculation of derivatives $\frac{\partial \varphi_d}{\partial \sigma_k}$

To derive the derivatives $\frac{\partial \varphi_d}{\partial \sigma_k}$ we apply a technique that is based on ideas of the electromagnetic adjoint method (Rodi, 1976, among others). This method uses the EM field reciprocity and has been applied previously to calculate sensitivities (Weidelt, 1975b; McGillivray and Oldenburg, 1990) and for forward modelling and inversion (Dorn *et al.*, 1999; Rodi and Mackie, 2001; Newman and Boggs, 2004; Chen *et al.*, 2005). The main idea behind EM field reciprocity is that we can interchange sources and receivers without affecting the measured electromagnetic field. This means that instead of calculating the field at the MT sites from sources located at every cell, we can can calculate the fields from sources located at the MT sites. Let us now describe our implementation of such a technique.

From equation 4.2 it easily follows that

$$\frac{\partial \varphi_d}{\partial \sigma_k} = \frac{1}{2} \sum_{i=1}^{N_S} \sum_{j=1}^{N_T} \beta_{ij} tr \left[\overline{\left(\overline{\mathbf{A}}_{ij}^T \frac{\partial \mathbf{Z}_{ij}}{\partial \sigma_k} \right)^T + \overline{\mathbf{A}}_{ij}^T \frac{\partial \mathbf{Z}_{ij}}{\partial \sigma_k}} \right]$$

$$\overset{\forall \mathbf{B}: tr\underline{\mathbf{B}}^T = tr\mathbf{B}}{=} \Re \left\{ \sum_{i=1}^{N_S} \sum_{j=1}^{N_T} \beta_{ij} tr \left[\overline{\mathbf{A}}_{ij}^T \frac{\partial \mathbf{Z}_{ij}}{\partial \sigma_k} \right] \right\}. \tag{4.7}$$

The MT impedance $\mathbf{Z}_{ij} = \mathbf{Z}(\mathbf{r}_i, \omega_j)$ is a 2×2 matrix, which satisfies the following matrix equation

$$\mathbf{E}_{ij} = \mathbf{Z}_{ij} \mathbf{H}_{ij}. \tag{4.8}$$

The matrices $\mathbf{E}_{ij}$, $\mathbf{H}_{ij}$ of equation 4.8 are defined as

$$\mathbf{E}_{ij} = \mathbf{p} \mathbf{E}_j(\mathbf{r}_i), \mathbf{H}_{ij} = \mathbf{p} \mathbf{H}_j(\mathbf{r}_i), \tag{4.9}$$

where $\mathbf{p} = \begin{pmatrix} 1 & 0 & 0 \\ 0 & 1 & 0 \end{pmatrix}$ is the 2×3 projection matrix, $\mathbf{E}_j(\mathbf{r}) = \begin{pmatrix} E_x^{(1)} & E_y^{(1)} & E_z^{(1)} \\ E_x^{(2)} & E_y^{(2)} & E_z^{(2)} \end{pmatrix}_j^T$

and $\mathbf{H}_j(\mathbf{r}) = \begin{pmatrix} H_x^{(1)} & H_y^{(1)} & H_z^{(1)} \\ H_x^{(2)} & H_y^{(2)} & H_z^{(2)} \end{pmatrix}_j^T$ are functions of the Cartesian coordinates $\mathbf{r} = (x, y, z)$. Here the superscripts 1 and 2 denote the polarization of the source $\mathbf{J}_j(\mathbf{r}) = \begin{pmatrix} J_x^{(1)} & J_y^{(1)} & J_z^{(1)} \\ J_x^{(2)} & J_y^{(2)} & J_z^{(2)} \end{pmatrix}_j^T$, and the vectors $\mathbf{E} = (E_x, E_y, E_z)^T$ and $\mathbf{H} = (H_x, H_y, H_z)^T$ are the electric and magnetic fields, respectively. We choose the polarizations of the source parallel(1) and perpendicular(2) to the x-axis. The 3×2 matrices $\mathbf{E}_j(\mathbf{r})$ and $\mathbf{H}_j(\mathbf{r})$ are composed of EM fields and, hence, they satisfy $2 \times N_T$ systems of Maxwell's equations written as

$$\nabla \times \mathbf{H}_j = \sigma(\mathbf{r})\mathbf{E}_j + \mathbf{J}_j, \tag{4.10a}$$

$$\nabla \times \mathbf{E}_j = \sqrt{-1}\omega_j \mu \mathbf{H}_j, \tag{4.10b}$$

where $\nabla \times \mathbf{H}_j$ and $\nabla \times \mathbf{E}_j$ denote 3×2 matrices $\begin{pmatrix} \nabla \times \mathbf{H}^{(1)} \\ \nabla \times \mathbf{H}^{(2)} \end{pmatrix}_j^T$, $\begin{pmatrix} \nabla \times \mathbf{E}^{(1)} \\ \nabla \times \mathbf{E}^{(2)} \end{pmatrix}_j^T$, respectively.

From equation 4.8 it immediately follows that

$$\mathbf{Z}_{ij} = \mathbf{E}_{ij} \mathbf{H}_{ij}^{-1}, \tag{4.11}$$

where $\mathbf{H}_{ij}^{-1}$ is the inverse of matrix $\mathbf{H}_{ij}$. Applying the chain-rule of differentiation to equation 4.11 one can derive

$$\mathbf{Z}_{ij,k} = (\mathbf{E}_{ij,k} - \mathbf{Z}_{ij}\mathbf{H}_{ij,k})\mathbf{H}_{ij}^{-1}, \tag{4.12}$$

where we denote

$$\mathbf{Z}_{ij,k} = \frac{\partial \mathbf{Z}_{ij}}{\partial \sigma_k}, \mathbf{E}_{ij,k} = \frac{\partial \mathbf{E}_{ij}}{\partial \sigma_k}, \mathbf{H}_{ij,k} = \frac{\partial \mathbf{H}_{ij}}{\partial \sigma_k} \quad (k = 1, ..., N). \tag{4.13}$$

Now substituting the derivative of equation 4.12 into equation 4.7 one gets

$$\frac{\partial \varphi_d}{\partial \sigma_k} = \Re \left\{ \sum_{i=1}^{N_S} \sum_{j=1}^{N_T} \beta_{ij} tr \left[\overline{\mathbf{A}}_{ij}^T (\mathbf{E}_{ij,k} - \mathbf{Z}_{ij}\mathbf{H}_{ij,k}) \mathbf{H}_{ij}^{-1} \right] \right\}. \tag{4.14}$$

Further, from equations 4.9, 4.10 it follows that

$$\mathbf{E}_{ij,k} = \mathbf{pe}_{jk}(\mathbf{r}_i), \mathbf{H}_{ij,k} = \mathbf{ph}_{jk}(\mathbf{r}_i), \tag{4.15}$$

where 3×2 matrices $\mathbf{e}_{jk}(\mathbf{r})$ and $\mathbf{h}_{jk}(\mathbf{r})$ satisfy $2 \times N_T \times N$ systems of Maxwell's equations

$$\nabla \times \mathbf{h}_{jk} = \sigma(\mathbf{r})\mathbf{e}_{jk} + \mathbf{j}_{jk}, \tag{4.16a}$$

$$\nabla \times \mathbf{e}_{jk} = \sqrt{-1}\omega_j\mu\mathbf{h}_{jk}, \tag{4.16b}$$

with the given electric current densities

$$\mathbf{j}_{jk} = \chi_k \mathbf{E}_j. \tag{4.17}$$

To derive equations 4.16, 4.17 from 4.10 we decompose the conductivity as $\sigma(\mathbf{r}) = \sum_{k=1}^{N} \sigma_k \chi_k(\mathbf{r})$ and then differentiate equations 4.10 by σ_k. We also assume that $\frac{\partial \mathbf{J}_j}{\partial \sigma_k} = 0$.

In equations 4.16 and 4.17 the matrices $\mathbf{e}_{jk}(\mathbf{r}) = \begin{pmatrix} e_x^{(1)} & e_y^{(1)} & e_z^{(1)} \\ e_x^{(2)} & e_y^{(2)} & e_z^{(2)} \end{pmatrix}_{jk}^T$ and $\mathbf{h}_{jk}(\mathbf{r}) = \begin{pmatrix} h_x^{(1)} & h_y^{(1)} & h_z^{(1)} \\ h_x^{(2)} & h_y^{(2)} & h_z^{(2)} \end{pmatrix}_{jk}^T$ are functions of the Cartesian coordinates $\mathbf{r} = (x, y, z)$.

Thus, to calculate the MT impedance derivative $\frac{\partial \mathbf{Z}}{\partial \sigma_k}(\mathbf{r}_i, \omega_j)$ for the complete set of triple indices $\{(i, j, k) : i = 1, ..., N_S, j = 1, ..., N_T, k = 1, ..., N\}$ one should solve

$2 \times N_T \times (N+1)$ forward problems, given in equations 4.10 and 4.16. Obviously, for a 3D conductivity model, where the number of cells, N, is relatively large, such an approach is not feasible. Fortunately, we need to calculate derivatives $\frac{\partial \varphi}{\partial \sigma_1}$, ..., $\frac{\partial \varphi}{\partial \sigma_N}$ rather than the matrices of equation 4.13. In the following explanation, we show that for the calculation of these derivatives $\frac{\partial \varphi}{\partial \sigma_1}$, ..., $\frac{\partial \varphi}{\partial \sigma_N}$, we need to solve only $2 \times N_T \times 2$ forward problems, rather then $2 \times N_T \times (N+1)$.

Along with the forward problems given in equation 4.16, let us also consider $2 \times N_T$ adjoint problems, presented by Maxwell's equations

$$\nabla \times \mathbf{v}_j = \sigma \mathbf{u}_j + \mathbf{j}_j^{ext} + \nabla \times \mathbf{h}_j^{ext}, \qquad (4.18a)$$

$$\nabla \times \mathbf{u}_j = \sqrt{-1}\omega_j \mu \mathbf{v}_j, \qquad (4.18b)$$

where $\mathbf{j}_j^{ext}$ and $\mathbf{h}_j^{ext}$ are defined as

$$\mathbf{j}_j^{ext} = \sum_{i=1}^{N_S} \beta_{ij} \mathbf{p}^T \overline{\mathbf{A}}_{ij} \mathbf{H}_{ij}^{-T} \delta(\mathbf{r} - \mathbf{r}_i), \qquad (4.19)$$

and

$$\mathbf{h}_j^{ext} = -\frac{1}{\sqrt{-1}\omega_j\mu} \sum_{i=1}^{N_S} \beta_{ij} \mathbf{p}^T \mathbf{Z}_{ij}^T \overline{\mathbf{A}}_{ij} \mathbf{H}_{ij}^{-T} \delta(\mathbf{r} - \mathbf{r}_i), \qquad (4.20)$$

respectively. In these equations $\mathbf{H}_{ij}^{-T}$ means transpose of $\mathbf{H}_{ij}^{-1}$, and δ is the Dirac's delta-function.

Let us now rewrite equations 4.16 and 4.18 as

$$\nabla \times \nabla \times \mathbf{e}_{jk} - \sqrt{-1}\omega_j\mu\sigma(\mathbf{r})\mathbf{e}_{jk} = \sqrt{-1}\omega_j\mu\chi_k\mathbf{E}_j, \qquad (4.21a)$$

$$\nabla \times \nabla \times \mathbf{u}_j - \sqrt{-1}\omega_j\mu\sigma(\mathbf{r})\mathbf{u}_j = \sqrt{-1}\omega_j\mu(\mathbf{j}_j^{ext} + \nabla \times \mathbf{h}_j^{ext}). \qquad (4.21b)$$

Multiplying equation 4.21a by $\mathbf{u}_j^T$ and equation 4.21b by $\mathbf{e}_{jk}^T$ and integrating the difference of the resulting equations over the whole 3D space, one gets

$$\int_{R^3} tr\left[\mathbf{e}_{jk}^T \mathbf{j}_j^{ext} + \mathbf{e}_{jk}^T \nabla \times \mathbf{h}_j^{ext}\right] dV = \int_{V_k} tr\left[\mathbf{u}_j^T \mathbf{E}_j\right] dV. \qquad (4.22)$$

To derive equation 4.22 we use the Green-type formula $\int_{R^3}(\mathbf{v}\nabla\times\mathbf{w} - \mathbf{w}\nabla\times\mathbf{v})dV = 0$ that is valid for any complex-valued vector fields $\mathbf{v}$ and $\mathbf{w}$. We then modify the left

hand side of equation 4.22 as

$$\int_{R^3} tr\left[\mathbf{e}_{jk}^T\mathbf{j}_j^{ext} + \sqrt{-1}\omega_j\mu\mathbf{h}_{jk}^T\mathbf{h}_j^{ext}\right]dV = \int_{V_k} tr\left[\mathbf{u}_j^T\mathbf{E}_j\right]dV, \qquad (4.23)$$

using $tr\left[\mathbf{e}_{jk}^T\nabla\times\mathbf{h}_j^{ext}\right] = tr\left[(\nabla\times\mathbf{e}_{jk})^T\mathbf{h}_j^{ext}\right] = \sqrt{-1}\omega_j\mu tr\left[\mathbf{h}_{jk}^T\mathbf{h}_j^{ext}\right]$. Substituting further equations 4.19, 4.20 for sources $\mathbf{j}_j^{ext}$, $\mathbf{h}_j^{ext}$ into equation 4.23 and using the property that $\int_{R^3}\mathbf{v}(\mathbf{r})\delta(\mathbf{r}-\mathbf{r}_i)dV = \mathbf{v}(\mathbf{r}_i)$ for any vector $\mathbf{v}$, one derives

$$\sum_{i=1}^{N_S}\beta_{ij}tr\left[\overline{\mathbf{A}}_{ij}^T\left(\mathbf{pe}_{jk}(\mathbf{r}_i) - \mathbf{Z}_{ij}\mathbf{ph}_{jk}(\mathbf{r}_i)\right)\mathbf{H}_{ij}^{-1}\right] = \int_{V_k} tr\left[\mathbf{u}_j^T\mathbf{E}_j\right]dV, \qquad (4.24)$$

since $tr[\mathbf{BC}] = tr[\mathbf{CB}]$, $tr[\mathbf{B}^T] = tr[\mathbf{B}]$, $(\mathbf{BC})^T = \mathbf{C}^T\mathbf{B}^T$ for any pair of matrices $\mathbf{B}$ and $\mathbf{C}$. Comparing equations 4.24, 4.9 and 4.14 one immediately concludes that

$$\frac{\partial\varphi_d}{\partial\sigma_k} = \Re\left\{\sum_{j=1}^{N_T}\int_{V_k} tr\left[\mathbf{u}_j^T\mathbf{E}_j\right]dV\right\}. \qquad (4.25)$$

The formula of equation 4.25 means that the computational loads for calculating the gradient of equation 2.25 are equivalent to those for the solution of $2\times N_T$ forward problems using equations 4.10 to find $\mathbf{E}_j$ and of $2\times N_T$ adjoint problems using equations 4.18 to find $\mathbf{u}_j$ for all $j = 1, ..., N_T$.

4.1.1.1. Numerical verification

To calculate the derivatives of equation 4.25 we need to solve the adjoint system of Maxwell's equations 4.18. To solve this system we should be able to calculate not the electric fields, but their averages over numerical cells, for the media excited by horizontal electric, $\mathbf{j}_j^{ext}$, and magnetic, $\mathbf{h}_j^{ext}$, dipoles. We are lucky that the *x3d* code computes exactly these averages. To verify the ability of *x3d*, we checked it against an analytical solution for a uniform space.

Thus, let us consider a uniform space with conductivity σ. For such a space the electric field components excited by a horizontal magnetic dipole of moment $(M_x, 0, 0)$, which is located at the coordinate origin, are as following (Ward and

Hohmann, 1987)

$$E_x = 0, \tag{4.26a}$$

$$E_y = -\sqrt{-1}\omega\mu\frac{M_x z a(r)}{r^2}(\kappa r + 1), \tag{4.26b}$$

$$E_z = \sqrt{-1}\omega\mu\frac{M_x y a(r)}{r^2}(\kappa r + 1), \tag{4.26c}$$

where $\kappa^2 = -\sqrt{-1}\omega\mu\sigma$, $r = \sqrt{x^2 + y^2 + z^2}$ and $a(r) = e^{-\kappa r}/4\pi r$.
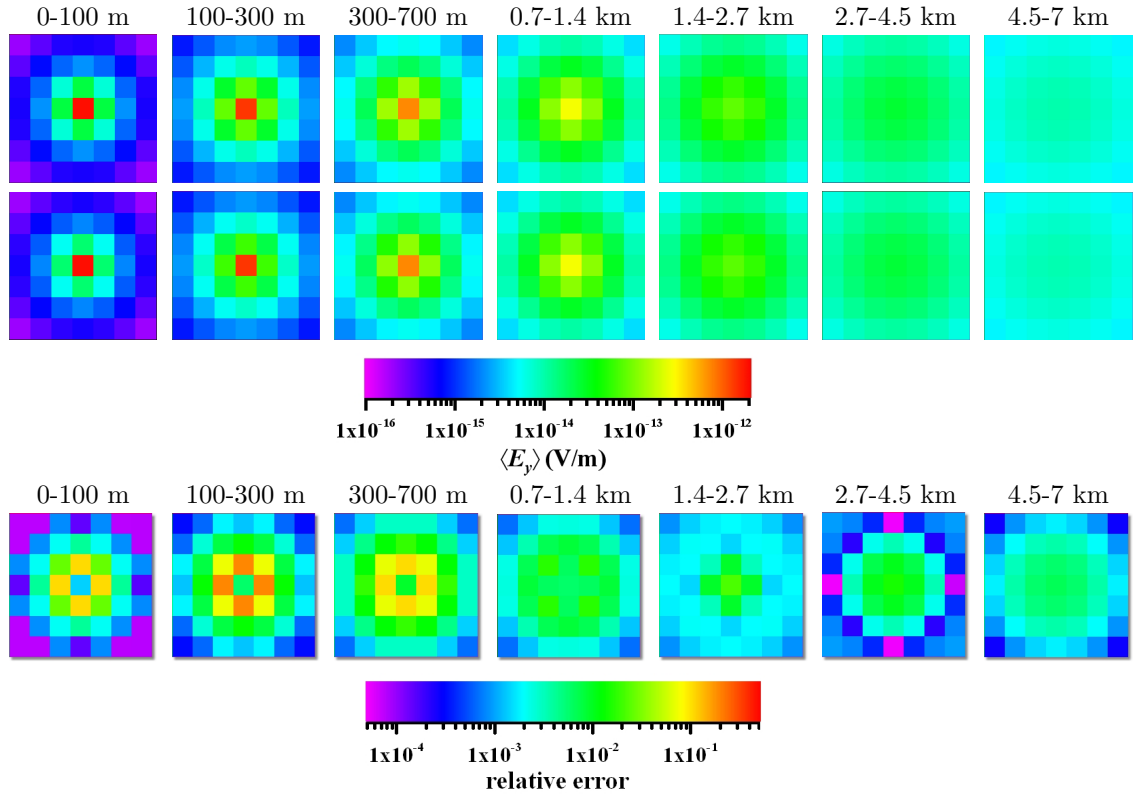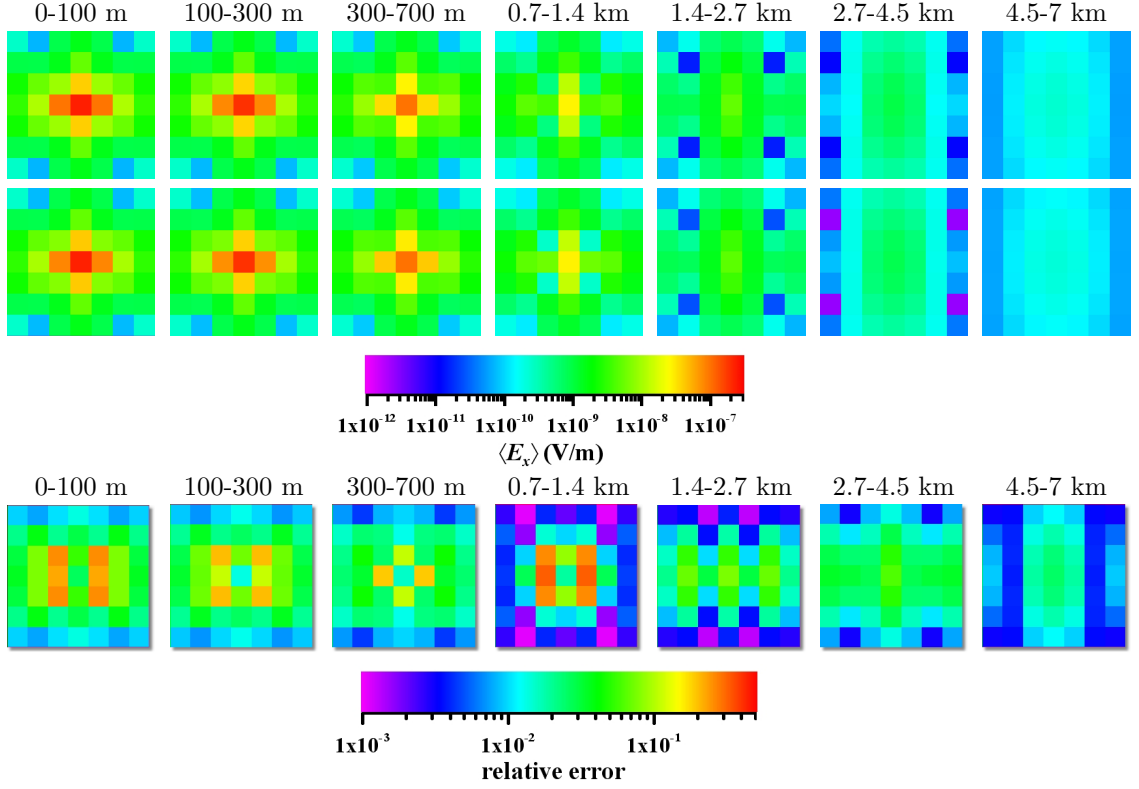

Figure 4.1.: Comparisons of averaged $\langle E_y \rangle$ for a uniform space excited by a magnetic dipole. Each row presents 7 horizontal $(x-y)$ slices starting from the top (left) to the bottom (right). The 1st row corresponds to $\langle E_y \rangle$ obtained using *x3d*, the 2nd row - to $\langle E_y \rangle$ obtained from equations 4.26b, 4.27 and 4.28. The 3rd row shows the relative error between averaged $\langle E_y \rangle$ obtained by *x3d* and those obtained from equations 4.26b, 4.27 and 4.28.

Using the *x3d* code, we calculated the 10-s electric fields for a 100 Ωm uniform space. The modelling domain was comprised of $N_x \times N_y \times N_z = 32 \times 32 \times 7 = 7168$ rectangular prisms, with $dx = dy = 1$ km. The magnetic dipole was situated in the centre of the upper face of the central cell. For each of the prisms we computed

an average of the electric field $\mathbf{E}$ and compared it with the analytical solution of equation 4.26. This comparison for the y-component of the electric field, $\langle E_y \rangle = \{ \int_{V_{\alpha\beta\gamma}} E_y dv \}/V_{\alpha\beta\gamma}$, is presented in Figure 4.1. In order to calculate analytically the average $\langle E_y \rangle$ for the most complicated central prism, where the dipole is seated, we make use of the fact that this prism is located at the near zone, $|\kappa r| << 1$. For the near zone from equation 4.26b we approximate the average as

$$\langle E_y \rangle_{\alpha_{tr}\beta_{tr}0} = \frac{\int\limits_{V_{\alpha_{tr}\beta_{tr}0}} E_y dv}{V_{\alpha_{tr}\beta_{tr}0}} \approx -i\omega\mu \frac{M_x}{2dxdy} \left\{ \frac{1 + dz_0/d - \sqrt{1 + (dz_0/d)^2}}{dz_0/d} \right\}, \quad (4.27)$$

where $d = \sqrt{dxdy/\pi}$, dz_0 is the thickness of the prism, and subscript tr stands for transmitter, as the source is located at the upper face of this central prism. For other cells we use the following formula

$$\langle E_y \rangle_{\alpha\beta\gamma} = E_y(x^c_{\alpha\beta\gamma}, y^c_{\alpha\beta\gamma}, z^c_{\alpha\beta\gamma}), \quad (4.28)$$

where $(x^c_{\alpha\beta\gamma}, y^c_{\alpha\beta\gamma}, z^c_{\alpha\beta\gamma})$ means the centre of the $\alpha\beta\gamma$-th cell and E_y in the right hand side is given by 4.26b. In the figure we present, for the sake of resolution, only 7×7 cells located around the magnetic dipole for first 7 horizontal slices, 0 - 7 km depth. From the figure we can see very good agreement between results produced by *x3d* and the analytical solution. We also compared the *x3d* solution and the analytical one for all other components of the electric field (not presented here) and found very good agreement.

We performed similar comparisons for the horizontal electric dipole with moment $(M_x, 0, 0)$. For this experiment we used the same uniform space with a resistivity of 100 Ωm and the same frequency of 10 s. We also used the same numerical grid of $N_x \times N_y \times N_z = 32 \times 32 \times 7 = 7168$ rectangular prisms, with $dx = dy = 1$ km. The analytical expressions for the electric field components in this case are as following:

$$E_x = \frac{M_x a(r)}{\sigma r^2} \left[(\kappa^2 r^2 + 3\kappa r + 3)\frac{x^2}{r^2} - (\kappa^2 r^2 + \kappa r + 1) \right], \quad (4.29a)$$

$$E_y = \frac{M_x a(r)}{\sigma r^2} \left[(\kappa^2 r^2 + 3\kappa r + 3)\frac{xy}{r^2} \right], \quad (4.29b)$$

$$E_z = \frac{M_x a(r)}{\sigma r^2} \left[(\kappa^2 r^2 + 3\kappa r + 3)\frac{xz}{r^2} \right]. \quad (4.29c)$$

Figure 4.2.: Comparisons of $\langle E_x \rangle$ for a uniform space excited by an electric dipole. Each row presents 7 horizontal $(x - y)$ slices starting from the top (left) to the bottom (right). The 1st row corresponds to $\langle E_x \rangle$ obtained using *x3d*, the 2nd - to $\langle E_x \rangle$ obtained from equations 4.29a, 4.30 and 4.31. The 3rd row shows the relative error between averaged $\langle E_x \rangle$ obtained by *x3d* and those obtained from equations 4.29a, 4.30 and 4.31.

As mentioned above we need the average values of electric fields over the prisms. To approximate these averages over the central cell (the cell where the electric dipole is situated) for the x-component of electric field we use the following formula:

$$\langle E_x \rangle_{\alpha_{tr}\beta_{tr}0} = \frac{\int\limits_{V_{\alpha_{tr}\beta_{tr}0}} E_x dv}{V_{\alpha_{tr}\beta_{tr}0}} \approx -\frac{M_x}{4\sigma dxdy}\frac{1}{\sqrt{dz_0^2 + d^2}}. \tag{4.30}$$

This formula is obtained by integrating equation 4.29a over the prism and assuming the near zone, $|\kappa r| << 1$. For other cells we again use

$$\langle E_x \rangle_{\alpha\beta\gamma} = E_x(x^c_{\alpha\beta\gamma}, y^c_{\alpha\beta\gamma}, z^c_{\alpha\beta\gamma}), \tag{4.31}$$

where E_x in the right hand side is given by 4.29a. The comparison of $\langle E_x \rangle$ obtained

from *x3d* and obtained from the analytical approximations 4.30 and 4.31 is presented in Figure 4.2. We also performed the comparison for all other components of the electric field and obtained good agreement.

Our conclusion from the above experiments is that we can use the *x3d* code for the calculation of the derivatives 4.25.

4.1.2. Regularization technique

As previously mentioned in Section 2.3, in order to alleviate the ill-posedness of the inverse problem we use a regularization function of the form 2.39. In our implementation the matrix $\mathbf{W}$ represents a finite-difference approximation to the Laplace operator. Therefore, the regularization function φ_s has the following form:

$$\varphi_s = dxdy \sum_{\alpha\beta\gamma} [\Delta\sigma(x,y,z)]^2_{\alpha\beta\gamma} \, dz_\gamma = dxdy \sum_{\alpha\beta\gamma} \left[\frac{\partial^2\sigma}{\partial x^2} + \frac{\partial^2\sigma}{\partial y^2} + \frac{\partial^2\sigma}{\partial z^2} \right]^2_{\alpha\beta\gamma} dz_\gamma \quad (4.32)$$

where dx, dy and dz_γ are the sizes of the cells in x, y and z directions, respectively. Note that dx and dy are constant throughout the numerical grid, although dx can be different from dy. At the same time, dz_γ can change with depth, the index γ corresponds to the number of the γ-th layer. These requirements on the cell sizes are imposed by the *x3d* code.

In equation 4.32 the second derivative operator is approximated as follows:

$$\left[\frac{\partial^2\sigma}{\partial x^2} \right]_{\alpha\beta\gamma} \approx A_\alpha^1 \sigma_{\alpha-1\beta\gamma} + A_\alpha^2 \sigma_{\alpha\beta\gamma} + A_\alpha^3 \sigma_{\alpha+1\beta\gamma} + A_\alpha^4 \sigma_\gamma^b \,, \qquad (4.33)$$

$$\left[\frac{\partial^2\sigma}{\partial y^2} \right]_{\alpha\beta\gamma} \approx B_\beta^1 \sigma_{\alpha\beta-1\gamma} + B_\beta^2 \sigma_{\alpha\beta\gamma} + B_\beta^3 \sigma_{\alpha\beta+1\gamma} + B_\beta^4 \sigma_\gamma^b \,, \qquad (4.34)$$

$$\left[\frac{\partial^2\sigma}{\partial z^2} \right]_{\alpha\beta\gamma} \approx C_\gamma^1 \sigma_{\alpha\beta\gamma-1} + C_\gamma^2 \sigma_{\alpha\beta\gamma} + C_\gamma^3 \sigma_{\alpha\beta\gamma+1} + C_\gamma^4 \sigma_{N_z+1}^b \,. \qquad (4.35)$$

In equations 4.33-4.35, $\alpha = 1, ..., N_x$, $\beta = 1, ..., N_y$, $\gamma = 1, ..., N_z$ and σ_γ^b is the conductivity of the background medium. Whether σ_γ^b appears in the stabilizer φ_s depends on the boundary conditions. We implemented two different types of boundary conditions that we will describe below. We also set $\sigma_{0\beta\gamma} = \sigma_{\alpha 0\gamma} = \sigma_{\alpha\beta 0} = \sigma_{N_x+1\beta\gamma} = \sigma_{\alpha N_y+1\gamma} = \sigma_{\alpha\beta N_z+1} = 0$.

When we use the Neumann boundary conditions, $\partial\sigma/\partial\nu|_{\partial V} = 0$, where ν is the normal to the boundary ∂V, the coefficients A_α, B_β and C_γ have the following form:

$$
A_\alpha^1 = \begin{cases} dx^{-2}, & \alpha \neq 1, N_x \\ 0, & \alpha = 1 \\ dx^{-2}, & \alpha = N_x \end{cases},
$$

$$
A_\alpha^2 = \begin{cases} -2dx^{-2}, & \alpha \neq 1, N_x \\ 0, & \alpha = 1 \\ 0, & \alpha = N_x \end{cases},
$$

$$
A_\alpha^3 = \begin{cases} dx^{-2}, & \alpha \neq 1, N_x \\ dx^{-2}, & \alpha = 1 \\ 0, & \alpha = N_x \end{cases},
$$

$$
A_\alpha^4 = \begin{cases} 0, & \alpha \neq 1, N_x \\ -dx^{-2}, & \alpha = 1 \\ -dx^{-2}, & \alpha = N_x \end{cases}.
$$

(4.36)

The coefficients B_β are derived in the same manner as the A_α, one just has to substitute α to β, dx to dy and N_x to N_y in equation 4.36. Finally,

$$
C_\gamma^1 = \begin{cases} \frac{2}{h_\gamma^{(1)}(dz_\gamma + dz_{\gamma-1})}, & \gamma \neq 1, N_z \\ 0, & \gamma = 1 \\ \frac{2}{h_\gamma^{(3)}(dz_\gamma + dz_{\gamma-1})}, & \gamma = N_z \end{cases},
$$

$$
C_\gamma^2 = \begin{cases} \frac{-8}{(dz_{\gamma+1} + dz_\gamma)(dz_\gamma + dz_{\gamma-1})}, & \gamma \neq 1, N_z \\ \frac{-2}{h_\gamma^{(2)}(dz_{\gamma+1} + dz_\gamma)}, & \gamma = 1 \\ 0, & \gamma = N_z \end{cases},
$$

$$
C_\gamma^3 = \begin{cases} \frac{2}{h_\gamma^{(1)}(dz_{\gamma+1} + dz_\gamma)}, & \gamma \neq 1, N_z \\ \frac{2}{h_\gamma^{(2)}(dz_{\gamma+1} + dz_\gamma)}, & \gamma = 1 \\ 0, & \gamma = N_z \end{cases},
$$

$$
C_\gamma^4 = \begin{cases} 0, & \gamma \neq 1, N_z \\ 0, & \gamma = 1 \\ \frac{-2}{h_\gamma^{(3)}(dz_\gamma + dz_{\gamma-1})}, & \gamma = N_z, \end{cases}.
$$

(4.37)

where

$$h_\gamma^{(1)} = \tfrac{1}{4}(dz_{\gamma-1} + 2dz_\gamma + dz_{\gamma+1}) \ ,$$

$$h_\gamma^{(2)} = \tfrac{1}{4}(dz_\gamma \quad + 2dz_\gamma + dz_{\gamma+1}) \ , \tag{4.38}$$

$$h_\gamma^{(3)} = \tfrac{1}{4}(dz_{\gamma-1} + 2dz_\gamma + dz_\gamma \quad) \ .$$

In this case the regularization given by equation 4.32 has a strong effect and depends strongly on the background conductivity σ_γ^b. We will call this strong regularization. This type of regularization should be used only when we have a very good idea about the conductivity of the 1D background model. As an example, strong regularization was used for a simple two-layered model considered in Section 4.2.1.

Another type of the boundary conditions we used in our research is those following from the continuity of the gradient at the boundary of the inversion domain, i.e.

$$\left.\frac{\partial \sigma}{\partial \nu}\right|_{\partial V^-} = \left.\frac{\partial \sigma}{\partial \nu}\right|_{\partial V^+} .$$

In this case the background conductivity, σ_γ^b, is not included in the stabilizer φ_s at all, and hence, the coefficients $A_\alpha^4 = B_\beta^4 = C_\gamma^4 = 0$, for all α, β and γ. All other coefficients A_α are

$$A_\alpha^1 = \begin{cases} dx^{-2}, & \alpha \in [2, N_x - 1] \\ 0, & \text{else} \end{cases} ,$$

$$A_\alpha^2 = \begin{cases} -2dx^{-2}, & \alpha \in [2, N_x - 1] \\ 0, & \text{else} \end{cases} , \tag{4.39}$$

$$A_\alpha^3 = \begin{cases} dx^{-2}, & \alpha \in [2, N_x - 1] \\ 0, & \text{else} \end{cases} .$$

The coefficients B_β are derived in the same manner as the A_α. The coefficients C_γ

have the following form

$$
C_\gamma^1 = \begin{cases} \frac{2}{h_\gamma^{(1)}(dz_\gamma + dz_{\gamma-1})}, & \gamma \neq 1, N_z \\ 0, & \text{else} \end{cases},
$$

$$
C_\gamma^2 = \begin{cases} \frac{-8}{(dz_{\gamma+1} + dz_\gamma)(dz_\gamma + dz_{\gamma-1})}, & \gamma \neq 1, N_z \\ 0, & \text{else} \end{cases}, \qquad (4.40)
$$

$$
C_\gamma^3 = \begin{cases} \frac{2}{h_\gamma^{(1)}(dz_{\gamma+1} + dz_\gamma)}, & \gamma \neq 1, N_z, \\ 0, & \text{else} \end{cases}.
$$

It is this type of regularization we call weak and we use in most of our numerical experiments (see Section 4.2).

4.1.2.1. Choice of parameter λ

As mentioned in the previous chapter, when a stabilizer φ_s is used in the inversion, we encounter the additional problem of finding the optimum regularization parameter λ. In Section 3.1.2 we proposed an approach for finding the regularization parameter λ for the 1D MT inversion case. There we solve several inverse problems with a fixed value of λ, starting from the same initial guess model, in order to find the optimum regularization parameter.

For the 3D case, the inversion can take several days to compute and this procedure becomes too time consuming. Therefore, for the 3D case, we choose the regularization parameter λ in a manner similar to the idea of Haber *et al.* (2000). A relatively large value of λ is initially assigned, and then gradually reduced. Then each new problem is solved using the solution of the previous problem (i.e. the model obtained using the previous value of λ) as an initial guess. How to choose the initial value for the regularization parameter λ and how fast it should be reduced at this moment purely depends on the experience of the user, and some automatic schemes still have to be developed.

4.2. Model study

To investigate the robustness and effectiveness of the inversion solution developed we performed a number of numerical experiments. These are described below.

For all of these experiments, we calculate the 2×2 matrices $\mathbf{D}_{ij}$ of "observed" impedances using the *x3d* code and added random noise to these data. The relative errors ε_{ij} of the impedance (see equation 4.3) were taken as 0.05. This value of ε_{ij} means that the misfit φ_d defined in equation 4.2 drops to 1, when the

$$rms = \left(\frac{1}{N_S N_T} \sum_{i=1}^{N_S} \sum_{j=1}^{N_T} \frac{tr\left[\overline{(\mathbf{Z} - \mathbf{D})}_{ij}^T (\mathbf{Z} - \mathbf{D})_{ij} \right]}{tr\left[\overline{\mathbf{D}}_{ij}^T \mathbf{D}_{ij} \right]} \right)^{\frac{1}{2}} \tag{4.41}$$

drops to 5%. We think that using the same forward code for the predicted and to generate the "observed" data is sufficient for testing the inversion, because the forward modelling code *x3d* has been tested against many other forward modelling codes (see, for example, MT3DINV[1] webpage) and the difference between the responses from different codes is less than the noise we add to the data.

4.2.1. Two-layered half-space

We first consider a simple two-layered model. This model consists of a 10 Ωm, 10 km-thick layer on top of a 100 Ωm uniform half-space. Our modelling domain, presented in Figure 4.3, comprises of $N_x \times N_y \times N_z = 19 \times 19 \times 7 = 2,527$ rectangular prisms, with $dx = dy = 950$ m and dz grows with depth (see Table 4.1). Our inversion domain coincides with the modelling domain. Thus $N = 2,527$ conductivities σ_k ($k = 1, ..., N$) of the prisms need to be recovered. Below are the results of the inversion, obtained while inverting the data from just a single MT site and from 4 MT sites.

γ	dz_γ [m]	z_γ [m]
1	1000	0
2	1500	1000
3	2000	2500
4	2500	4500
5	3000	7000
6	3000	10000
7	3000	13000

Table 4.1.: Thicknesses and depths of the layers. γ corresponds to the number of the layer

---

[1]MT 3D Inversion Workshop, DIAS, March, 2008,
http://www.dias.ie/lang/en/cosmic/geo/mt_workshop2008.html
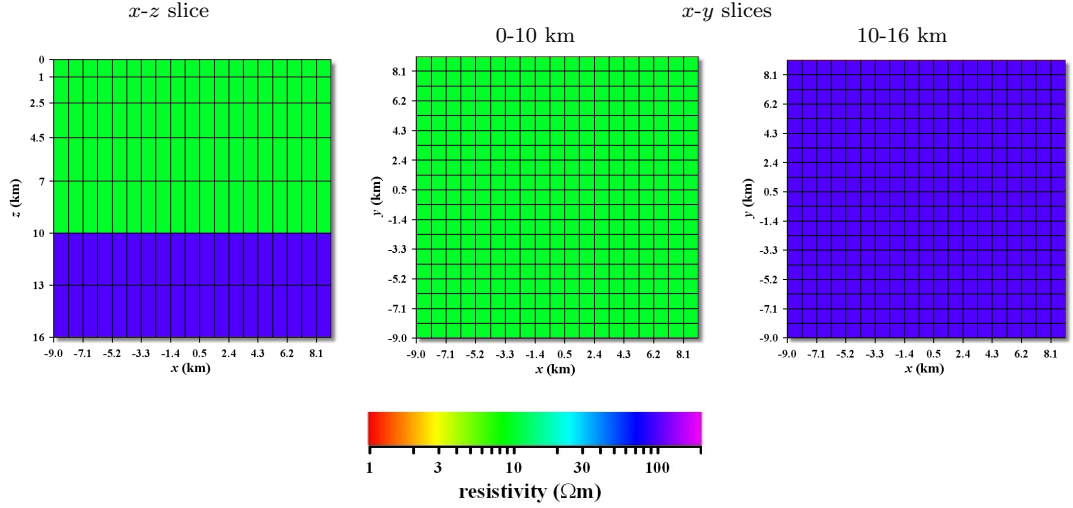
Figure 4.3.: Two-layered conductivity model used for testing the inversion. The left most panel shows a vertical (x-z) slice through the modelling domain. The other two panels show the horizontal (x-y) slices for two ranges of depths, 0-10 km and 10-16 km.

Single MT site

For a period of 100 s ($N_T = 1$) and for one MT site ($N_S = 1$), located on the surface ($z = 0$), at the centre of the numerical grid ($\alpha_s = \beta_s = 10$), all 4 complex-valued elements of MT impedance tensor, $\widetilde{\mathbf{D}}_{ij}$ (see page 49), were calculated. We added 1% noise to these "observed" data, this means that $\mathbf{D}_{ij} = \widetilde{\mathbf{D}}_{ij}(1 + \xi_{ij})$, where ξ_{ij} are random numbers between -0.01 and 0.01. The initial guess model, described in equation 4.6, was a model with the conductivities $\sigma_k^{(0)} = 50$ Ωm for all the cells of the inversion domain. Its background coincided with the background of the true model. The values of the conductivities of the background model do not change during the inversion, only conductivity values of the cells inside inversion domain are sought. For this experiment we used the strong regularization (see page 60) and the regularization parameter λ was kept unchanged and equal to 10^6. In fact, this high value of λ means that the process of inversion is mostly governed by the stabilizer φ_s, rather than φ_d. Indeed $\varphi_d/\lambda\varphi_s \approx 3\%$, and hence, practically $\varphi \approx \varphi_s$.

The inversion was stopped at $n_{fg} = 289$ since it could not generate any significant improvements. The objective functional at this iteration was $\varphi = 113.5$ and the data misfit $\varphi_d = 2.9$. This value of the data misfit corresponds to an *rms* of 8.5% (see equation 4.41). Let us recall here that the index n_{fg} increases by one after each
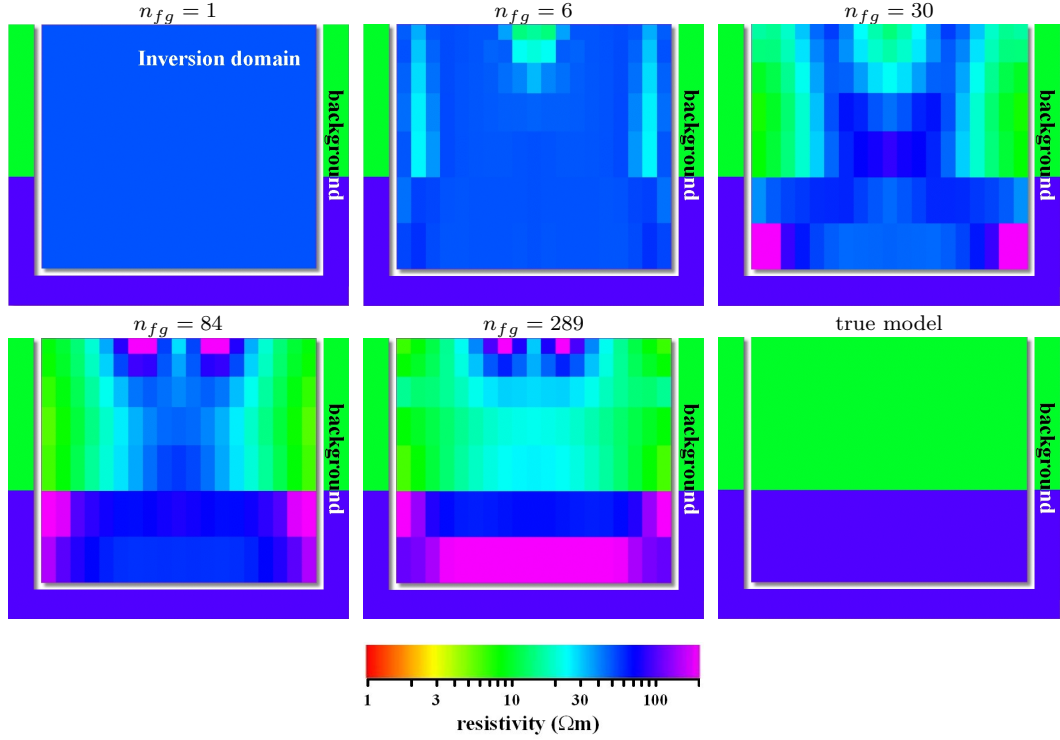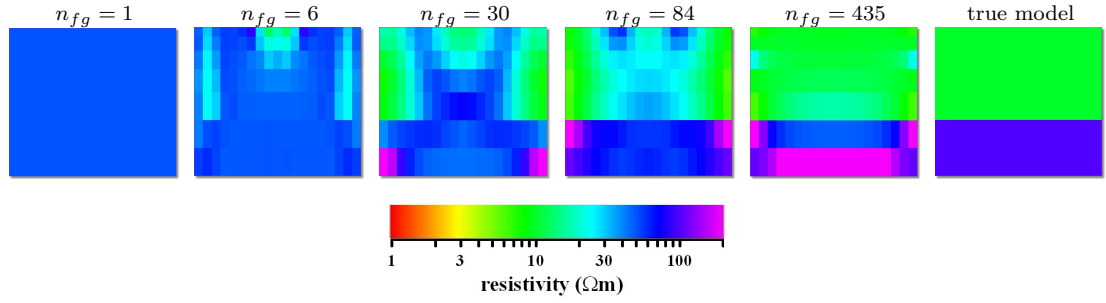
Figure 4.4.: The process of the inversion. The panels present vertical (x-z) cross-sections through the middle ($y = 0$) of the model starting from the initial guess model. The iteration number is written over the panels. True model is also presented for comparison.
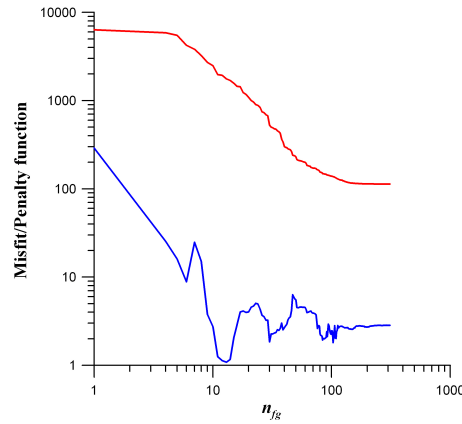

Figure 4.5.: The convergence curves for data misfit φ_d (blue) and penalty function φ (red). The curves are plotted as a function of n_{fg}.

evaluation of a pair φ and **g**. This index is proportional to the time of the inversion and a little larger than the number of the QN iterations n_{it}. Note that for the true model $\varphi = 203$, whereas the initial guess model gives $\varphi = 6342$. Figure 4.4 shows

a vertical slice through the middle of the models, obtained after various number of iterations. From the figure we can see how the inversion progresses from iteration to iteration. We can see that a resistive circular artifact appears around the MT site in the upper part of the models, when n_{fg} reaches a value between 30 and 84. The regularization does not help to remove this artifact and it still remains at the end of the inversion process, when $n_{fg} = 289$. In contrast, at larger depths the resistivities of the cells approach the resistivity of the true model. The conclusion from this example is that the inversion process stagnates after $n_{fg} = 289$, still not giving the true image. It is interesting to see what happens if we include more MT sites in the inversion.

4 MT sites

Let us consider the same two-layered model with the same grid. We chose $N_S = 4$ MT sites on the surface of the earth. The locations of the sites coincides with the centres of the cells and are shown in Figure 4.6 together with the grid. We again computed the "observed" MT impedance tensor, $\widetilde{\mathbf{D}}_{ij}$, and then added 1% noise to it. It should be noted that the values for the elements of noiseless $\widetilde{\mathbf{D}}_{ij}$ are identical for all 4 MT sites, as it may be expected for a 1D model.
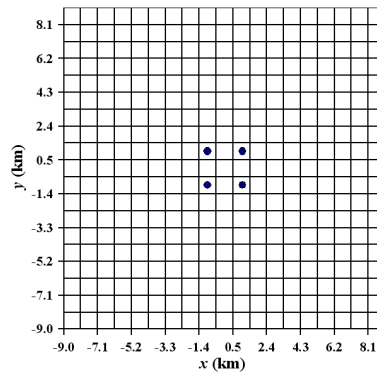
Figure 4.6.: Location of the MT sites.

Figure 4.7 shows the process of the inversion. This process is presented in a similar manner as before for 1 MT site, but now we only show the inversion domain. We again used strong regularization and the regularization parameter λ was kept constant and equal to 10^6 for the whole process of the inversion. Comparing Figures 4.4 and 4.7, we can see very similar behaviour of the inversion for the first 30 function and gradient evaluations. However, now we do not get the resistive artifact at later

Figure 4.7.: The process of the inversion. The row of panels presents vertical (x-z) slice through the middle ($y = 0$) of the model starting from the initial guess model (left) to the true model (right). The iteration number is written over the panels. True model is also presented for comparison.
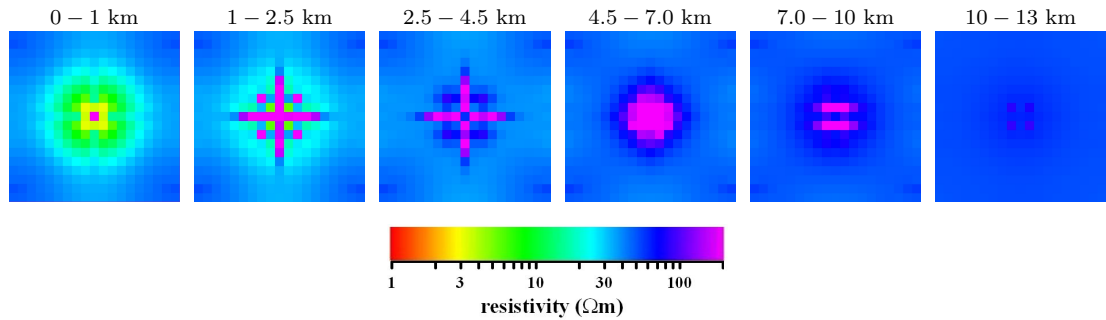
Figure 4.8.: 3D electrical resistivity model for 4 MT sites without regularization. The row of panels presents 6 horizontal (x-y) slices through the model starting from the top (left) to the bottom (right). The range of depths is given right above each panel.

iterations and we obtain a model very similar to the true model, when $n_{fg} = 435$ and the data misfit $\varphi_d = 0.4$, corresponding to an *rms* of 3%, which is smaller than was obtained using one MT site.

In contrast, if we do not apply the regularization functional (λ is set to zero), it is equivalent to the minimization of the data misfit φ_d only. The recovered model obtained in this case is presented in Figure 4.8. From the figure we can see that the inversion result has little similarity with the true model. At first, this result might seem surprising, because we consider a two-layered model as simple, however 3D inversion does not have any idea about 1D nature of the model and seeks any model which would explain the data. It happens that the model presented in Figure 4.8 is simple for the inversion.

Comparing Figures 4.7 and 4.8 one can conclude that the stabilizer φ_s greatly

helps to obtain a reasonable image. However, for the sake of objectivity, we should mention that the good image presented in Figure 4.7 may be just a result of the strong regularization used. With this strong regularization, the inversion tends to extend the background conductivity inside inversion domain, as can be seen from the form of strong regularization, given in Section 4.1.2. When inverting the real data we usually do not know the conductivity of the background, and hence, we should not use strong regularization in the inversion. That is why we use weak regularization for most of the experiments described below.

4.2.2. Buried conductive dyke
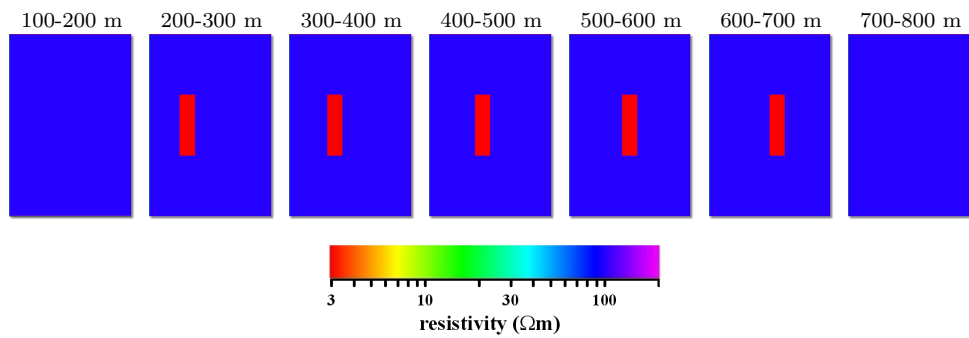
Figure 4.9.: 3D electrical resistivity model. The row of panels presents 7 horizontal (*x*-*y*) slices through the model starting from the top (left) to the bottom (right). The range of depths is given right above each panel.
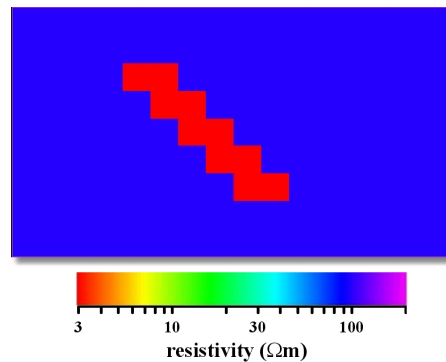
Figure 4.10.: (*x*-*z*) slice through the centre of the 3D resistivity model.

The second example employs a truly 3D model, which is presented in Figures 4.9 and 4.10. One of the reason to consider this model is that it was previously used to test a 3D MT inversion algorithm in Zhdanov and Tolstaya (2004). This model
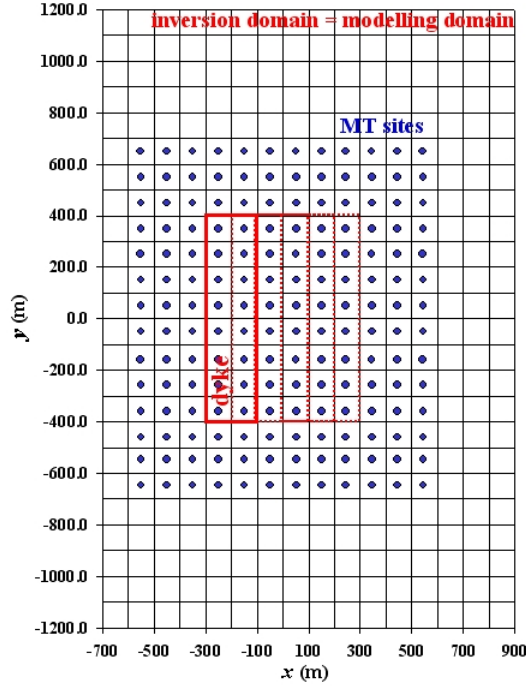
Figure 4.11.: Numerical mesh and location of the MT sites for the model presented in Figures 4.9 and 4.10.

consists of a tilted 3 Ωm dyke embedded into a 100 Ωm half-space. The dyke is located at a depth of 200 m to 700 m and it consists of 5 shifted adjacent blocks of $200 \times 800 \times 100$ m^3 size each. Our modelling domain comprises of $N_x \times N_y \times N_z = 16 \times 24 \times 8 = 3,072$ rectangular prisms of $100 \times 100 \times 100$ m^3 size that cover the dyke and some part of the surroundings. Notice that the modelling volume lies at depths of 100-900 m and during the forward problem solution *x3d* embeds this modelling volume into 100 Ωm background.

The inversion domain coincides with the modelling domain. This means that $N = 3,072$ conductivities σ_k $(k = 1, ..., N)$ of the prisms need to be recovered. For this model we calculate 2×2 matrices $\widetilde{\mathbf{D}}_{ij}$ of "observed" impedances at $N_T = 4$ frequencies $(f_i = 1/T_i, \ i = 1, ..., N_T)$ of 1000, 100, 10 and 1 Hz. For real MT surveys usually more frequencies are used, however our experiments are mainly for understanding and improving the inversion software and using the realisticly higher number of frequencies would lead to a very long times for the inversion and therefore to less experiments. The impedances were computed at $N_S = 168$ sites $\mathbf{r}_j$ $(j = 1, ..., N_S)$ coinciding with the centres of a homogeneous $n_x \times n_y = 12 \times 14$ grid, with a 100 m distance between adjacent nodes (see Figure 4.11).

With this synthetic example we perform a number of numerical experiments, which are described below.

4.2.2.1. Regularization by simple bounds

For our first numerical experiment with this model we did not apply the stabilizer φ_s of equation 2.39, i.e. the regularization parameter λ was assigned a zero value. Instead, we constrained the conductivity values to lie between $l_k = 200$ Ωm and $u_k = 1$ Ωm of equation 4.4. Subsequently this turned out to play a similar role to that of regularization. It should be noted that without putting these constraints on σ_k the iteration method without a stabilizer (i.e. when $\lambda = 0$) stagnates, when the data misfit φ_d drops to a value of 0.7 (see Figure 4.12) and it fails to produce a good conductivity image.
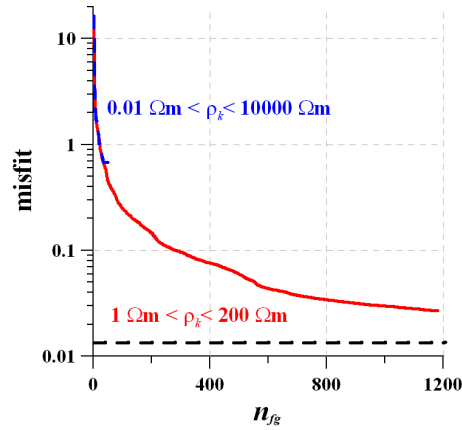
Figure 4.12.: Convergence rates of the inversions without use of a stabilizer φ_s, but with some limits imposed on the conductivities of the cells. The horizontal dashed line shows the value of the data misfit for the true model and for the data with 1% noise added.

The curves in Figure 4.12 are shown as a function of the number n_{fg} of evaluations of the penalty function of equation 4.1 and its gradient given in equation 2.25. To obtain these results we have chosen a number $n_{cp} = 6$ of correction pairs, a 100 Ωm homogeneous half-space as an initial guess and 1% random noise was added to the impedance matrix $\widetilde{\mathbf{D}}_{ij}$.

The convergence rates for various numbers n_{cp} of correction pairs is presented in Figure 4.13(a). From this figure it can be seen that for $n_{cp} = 6$ we get an even better convergence rate than for $n_{cp} = 20$. Therefore, for all simulations presented later in this section we used $n_{cp} = 6$. Surprisingly, for 2 correction pairs we only

get a slightly worse convergence and we manage to obtain a data misfit as small as $\varphi_d = 0.03$. Figure 4.13(b) presents the comparison of the convergence rates of the various inversions of datasets with different amounts of noise (0%, 1% and 5%) added. From this figure we can see that even with 5% noise added a reasonable data misfit is reached. As mentioned above, the noise floor ε_j is 0.05 for all of our experiments, and therefore the final misfit levels we try to achieve are different for different noise levels.
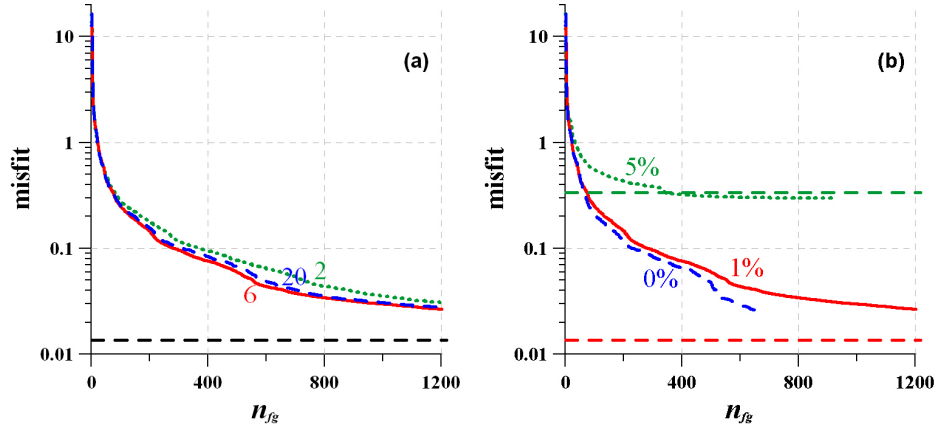
Figure 4.13.: Comparisons of convergence rates of the inversions for different cases: (a) various numbers of correction pairs: $n_{cp} = 2$ (dotted line), $n_{cp} = 6$ (solid line) and $n_{cp} = 20$ (dashed line). 1% noise was added to the data; (b) various levels of the data noise: 5% noise (dotted line), 1% (solid line) and no noise (dashed line). $n_{cp} = 6$. The horizontal dashed lines show the level of the data misfit φ_d calculated for the true model and noisy data (1%, 5%).

It should be noted that it takes 5 minutes for a single penalty function and its gradient evaluation to be computed on a serial PC. This means that it takes 4 days to obtain results for the synthetic data with 1% noise added.

4.2.2.2. Acceleration of convergence

The numerical experiment presented in Section 4.2.2.1 was undertaken with some limits imposed on possible values of the conductivities of the cells. Since these limits ($l_k = 200$ Ωm and $u_k = 1$ Ωm, $k = 1, ..., N$) for the conductivities are not very realistic, we now extend these values to $l_k = 10000$ Ωm and $u_k = 0.01$ Ωm, but restart the inversion process every n_{rs}-th iteration in order to obtain a better convergence rate and smaller data misfit. In other words, a model obtained after n_{rs}

iterations is taken as a new initial guess model and the inversion process is repeated. From the point of Newton-type optimization the latter means that after each n_{rs} iterations QN search direction of equation 2.28 is modified to be a steepest descent direction, $\mathbf{p}^{(k)} = -\mathbf{g}^{(k)}$, $k = n_{rs} * i, i = 0, 1, \ldots.$
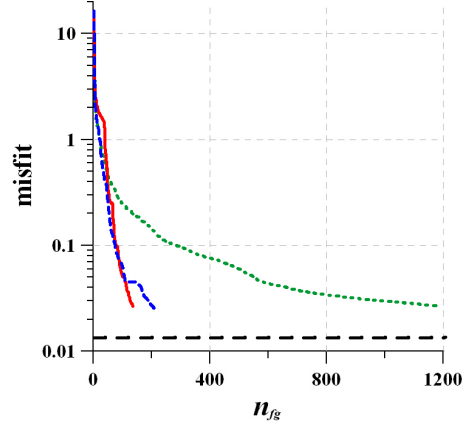
Figure 4.14.: Convergence rates of the inversions with the stabilizer and with gradually diminishing regularization parameter λ (solid line), with restart every 20-th iteration (dashed line) and without restart and stabilizer, but with limits on the cells conductivities (dotted line). The curves present the data misfit versus the number of evaluations of the penalty functional and its gradient. The dashed horizontal line shows the value of the data misfit for the true model and data with 1% noise added.

The comparison of convergence rates for restarted and non-restarted inversions is presented in Figure 4.14. Again, the convergence curves are shown as a function of n_{fg}. It can be seen that the inversion converges to the solution faster if it is restarted every 20-th iteration. In addition, only 1 day instead of 4 days of CPU time is required to reach an acceptable data misfit on a serial PC. One of the possible explanations of such an improvement is that in order to achieve a good convergence rate, the limited memory QN approximation of the inverse of the Hessian should be as close as possible to the true inverse. However, the curvature of the objective function may change rapidly and gradient information even from the previous n_{cp} iterations does not improve the inverse of the Hessian approximation at the current iteration. It therefore can be better to discard this information and restart the inversion process taking the steepest descent as a search direction. However, this explanation is very speculative and requires further analysis and investigation.

4.2.2.3. Regularization by smoothing

The experiments presented in Sections 4.2.2.1 and 4.2.2.2 were done without the stabilizer φ_s of equation 2.39 involved, i.e. with $\lambda = 0$. In this section we use the stabilizer φ_s and choose the regularization parameter λ, as explained in Section 4.1.2.1. For this experiment we start with $\lambda = 10^6$ and then gradually diminish it to 10^3. The result of the inversion is presented in Figures 4.15 and 4.16. The
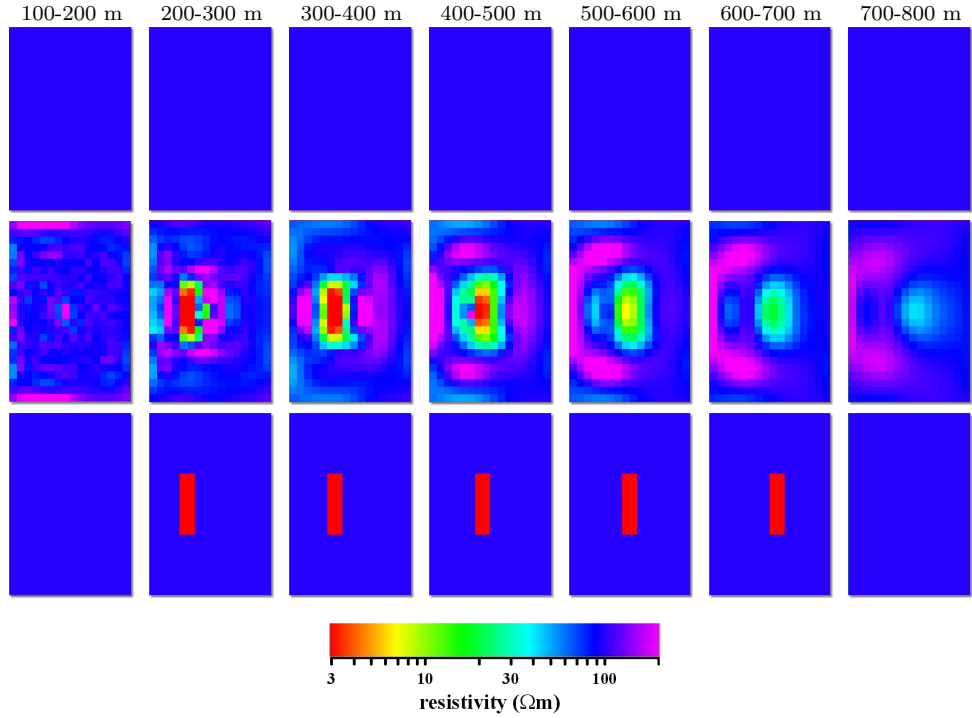

Figure 4.15.: Inversion result with 168 MT sites and 4 frequencies. The row of panels presents 7 horizontal (x-y) slices through the model starting from the top (left) to the bottom (right). The upper row of panels presents the initial guess model, the middle row - the image recovered using smoothing regularization and gradually diminishing regularization parameter λ, the lower row is for the true model.

comparison with the true model, shown in the same figures, demonstrates good results when we combine the inversion technique with smoothing regularization and with gradually diminishing regularization parameter λ. From the figure we can see that the position, shape and amplitude of the true anomaly is successfully recovered, although there are few resistive artifacts. This is especially true for the upper part of the model. As we can expect for MT inversion, the deeper layers are not recovered as sharp as the upper ones - the bottom part of the recovered model is naturally
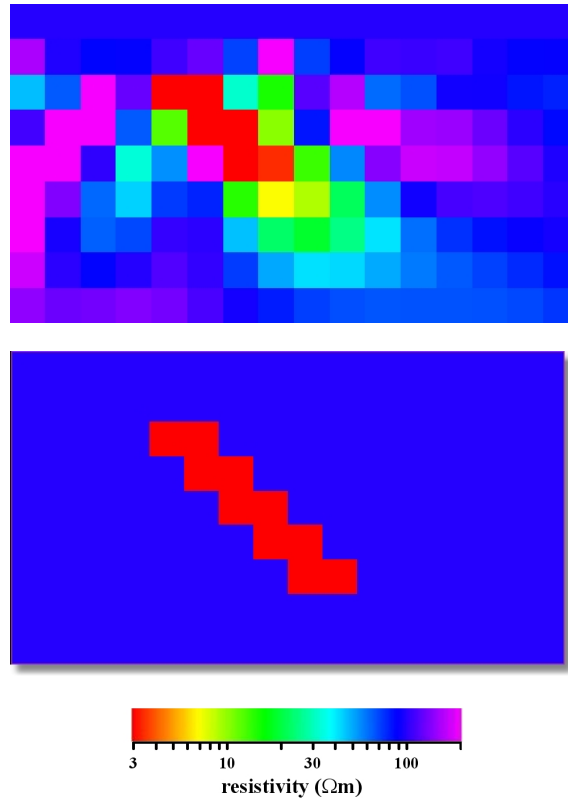
Figure 4.16.: Comparison for a central (x-z) cross-section. The upper panel presents the inversion result, whereas the lower panel presents true model. We used responses at 168 MT sites and 4 frequencies.
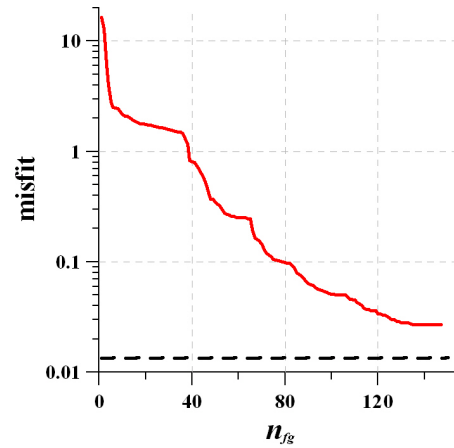
Figure 4.17.: Convergence of the data misfit φ_d. 168 MT sites and 4 frequencies were used.

smeared out, delivering only a hint on the presence of the conductive dyke. The convergence curve for this inversion is presented in Figure 4.17.
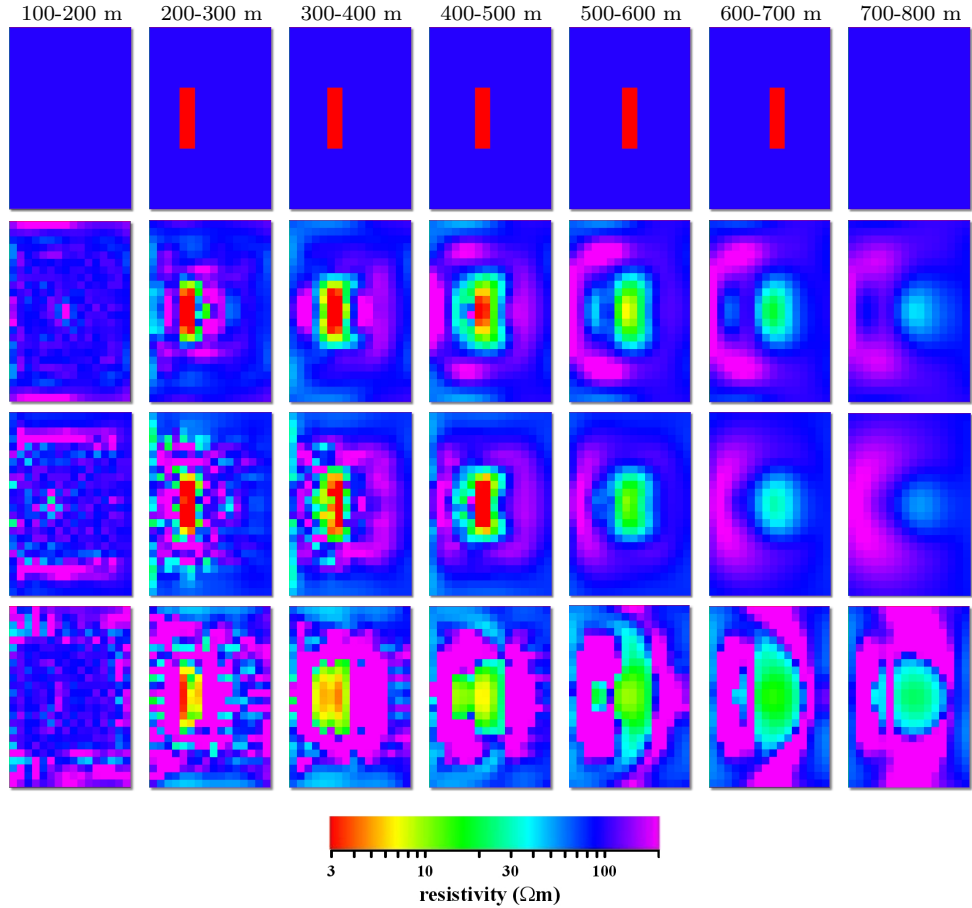
Figure 4.18.: Comparison of the inversion results obtained for various regularization techniques. Each row of panels present seven horizontal $(x - y)$ slices of the model starting from 150 m (left) to 750 m (right) depth (z). 1-st row corresponds to the true model; 2-nd row - to the result of the inversion with use of the stabilizer and with gradually diminishing regularization parameter λ; 3-rd row - to the result of the inversion with $n_{rs} = 20$ and without use of the stabilizer, and the last row corresponds to the result of the inversion without use of the stabilizer, but with limits imposed on conductivities.

The comparison of the results using this approach (i.e. reducing the regularization parameter) and those results without the stabilizer is presented in Figure 4.18. In all cases the inversions were terminated when the data misfit φ_d could not be improved significantly, and it dropped to 0.027. This value of the data misfit corresponds to an rms of 0.8% (see equation 4.41), which is just below the actual noise level. We observe that the inversion using the stabilizer φ_s and with gradually diminishing regularization parameter λ produces a much better result. The results of the inver-

100-200 m   200-300 m   300-400 m   400-500 m   500-600 m   600-700 m   700-800 m

resistivity (Ωm)
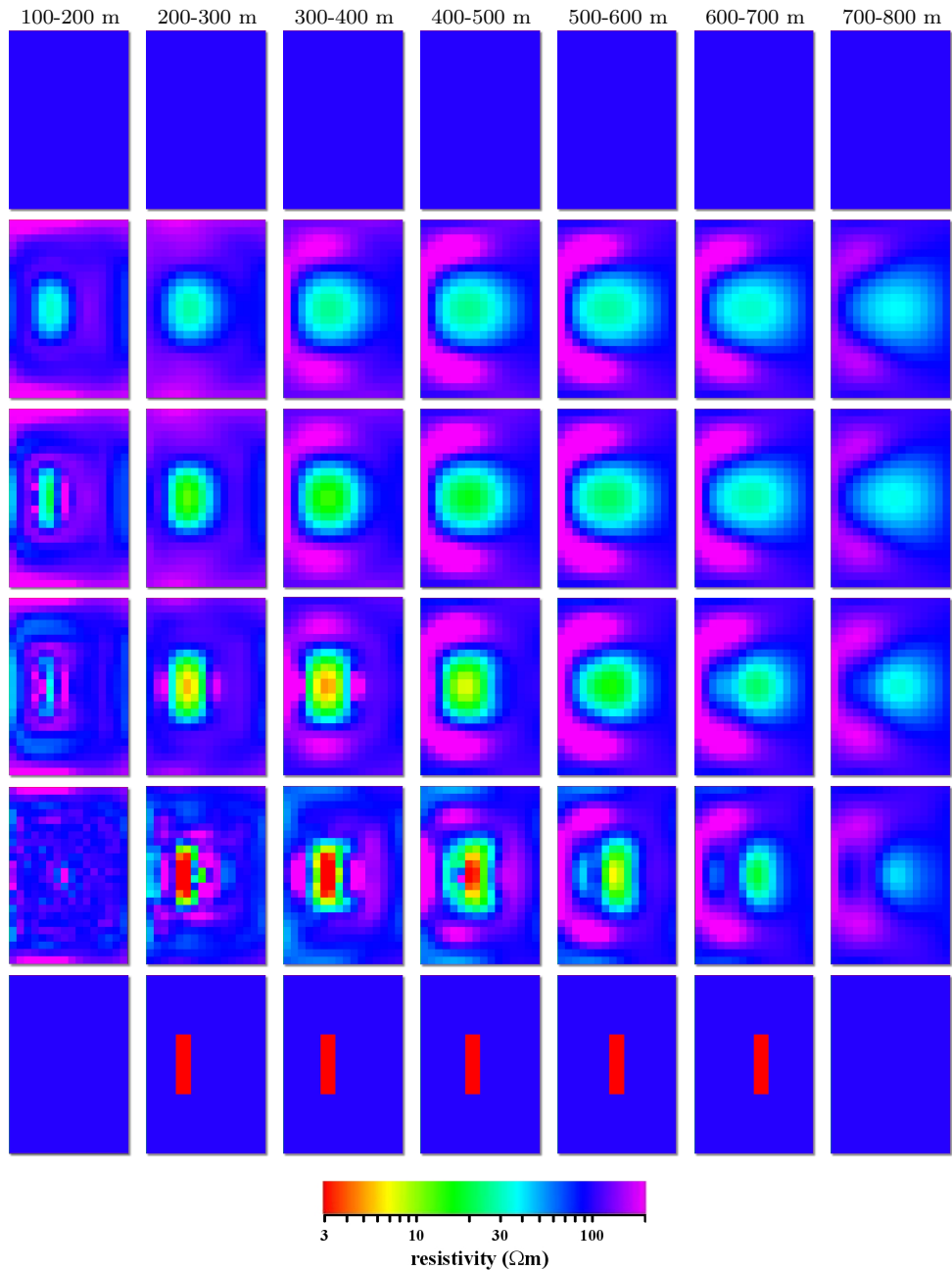
Figure 4.19.: Convergence of the inversion with use of the stabilizer and with gradually diminishing regularization parameter λ. 1-st row - the initial guess 100 Ωm model ($\varphi_d = 16.44$); 2-nd row - model obtained after $n_{fg} = 34$ ($\varphi_d = 1.51$); 3-rd row - model after $n_{fg} = 40$ ($\varphi_d = 0.83$); 4-th row - model after $n_{fg} = 64$ ($\varphi_d = 0.25$); 5-th row - after $n_{fg} = 147$ ($\varphi_d = 0.027$), the last row corresponds to the true model ($\varphi_d = 0.013$).

sions without the stabilizer produce highly erratic images, especially for the upper

slices. We obtained the worst result when the conductivity values were constrained between 1 Ωm and 200 Ωm (see the last row in Figure 4.18). One of the reasons for such a poor result is that it is very easy to reach the boundaries in the process of the inversion and the method tends to stick to these boundaries. In all of the following experiments we are not using such close limits for the conductivities, but instead employ the stabilizer φ_s.

Finally, a set of 3D models recovered at various iterations is presented in Figure 4.19 for the inversion that uses the stabilizer and with the parameter λ gradually diminishing from 10^6 to 10^3. From this figure we can see that the inversion quickly senses the presence of the conductor, although the value of the conductivity and its shape are defocused. When the number of objective function and its gradient evaluations increases the inversion focuses more and more and when we reach the n_{fg} of 147 we get the true shape, resistivity and the location of the conductor at the upper layer of the model. Still, some resistive halo persists.

4.2.3. Outcropping conductive dyke
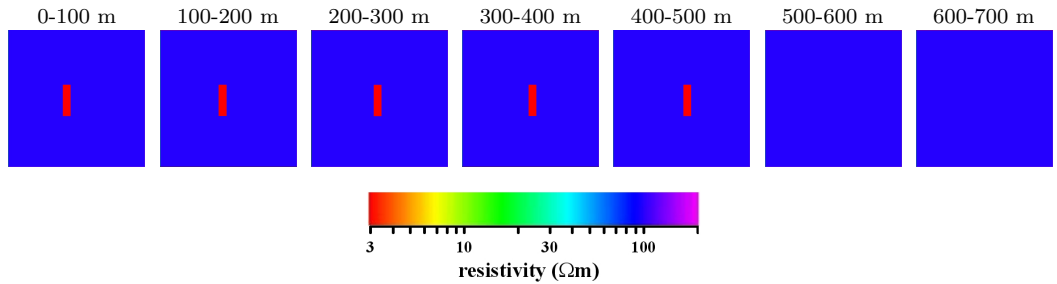
Figure 4.20.: 3D electrical resistivity model. The row of panels presents 7 horizontal (x-y) slices through the model starting from the top (left) to the bottom (right).

The third model is similar to the previous one, but now the 3D conductive dyke reaches the surface (see Figures 4.20 and 4.21). This model is more challenging, due to numerical difficulties that arise from the outcropping of the dyke, and we expect erratic behaviour of the conductivities in the near surface layers. For the calculation of the gradients of the data misfit φ_d we have to calculate the adjoint electric field $\mathbf{u}_j$, which is the solution of the system of adjoint Maxwell's equations 4.18. As it follows from this equation, the adjoint field $\mathbf{u}_j$ is some combination of electric fields of horizontal electric and magnetic dipoles. This combination should be averaged
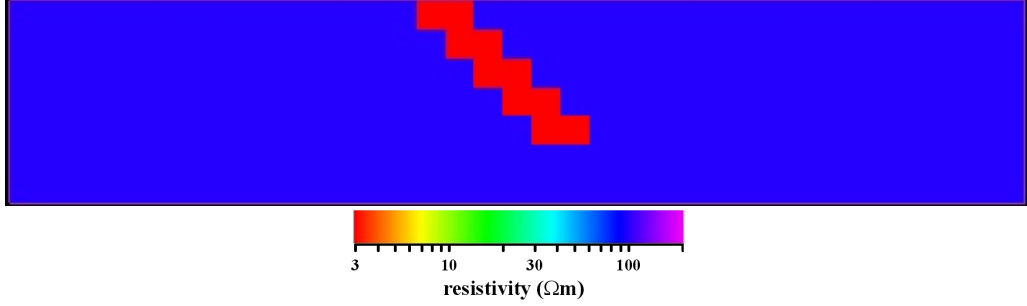
Figure 4.21.: $(x\text{-}z)$ slice through the centre of the 3D resistivity model.

over each cell of the inversion domain. The dipoles are positioned in the locations of the MT sites. For an outcropped dyke, the upper cells of the inversion domain touch the dipoles, which makes averaging over the cells a difficult problem. Closer examination of the problem shows that it is rooted in the physics of MT problem, rather than numerical - the derivatives of the data misfit for the cells touching the dipoles are significantly greater than for all other cells. This reflects the fact that the cells are far more sensitive to the MT data.

Returning to the model, the 3 Ωm dyke is located at a depth of 0 m to 500 m and consists of the same 5 shifted adjacent blocks of $200 \times 800 \times 100$ m^3 size each. The modelling domain comprises of $N_x \times N_y \times N_z = 35 \times 35 \times 7 = 8,575$ rectangular prisms of $100 \times 100 \times 100$ m^3 size that cover the dyke and some part of the surroundings, and extends from 0 to 700 m depth. The inversion domain is smaller than the modelling domain and it comprises of $N_x \times N_y \times N_z = 16 \times 24 \times 7 = 2,688$ cells that cover the dyke and some part of the surrounding (see blue box in Figure 4.22).

4.2.3.1. 168 MT sites

For this model we again calculate 2×2 matrices $\widetilde{\mathbf{D}}_{ij}$ of "observed" impedances at $N_T = 1$ frequency of 10 Hz, and then add 1% noise to this data. The impedances are computed at $N_S = 168$ sites $\mathbf{r}_i$ $(i = 1, ..., N_S)$ coinciding with the centres of a homogeneous $n_x \times n_y = 12 \times 14$ grid, with a 100 m distance between adjacent nodes (see Figure 4.22). Of course it is unrealistic to use a single frequency for the inversion, however with one frequency it is easier to examine and understand the behaviour of the inversion algorithm. In this case we start the inversion with the initial guess model, which has 50 Ωm everywhere inside the inversion domain, in contrast to 100 Ωm we had for the buried dyke. Figure 4.23 presents the result of the inversion together with the initial and true models. The vertical cross-section
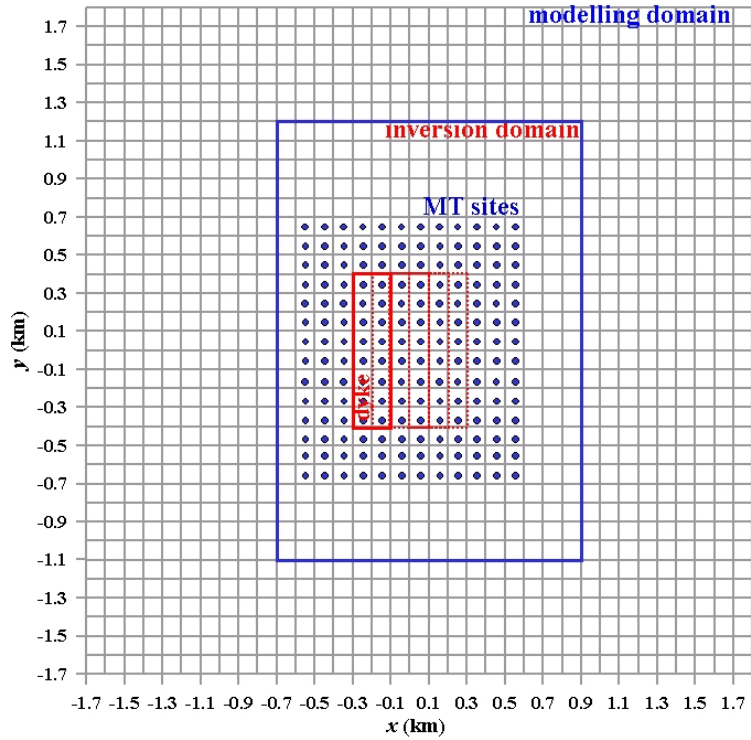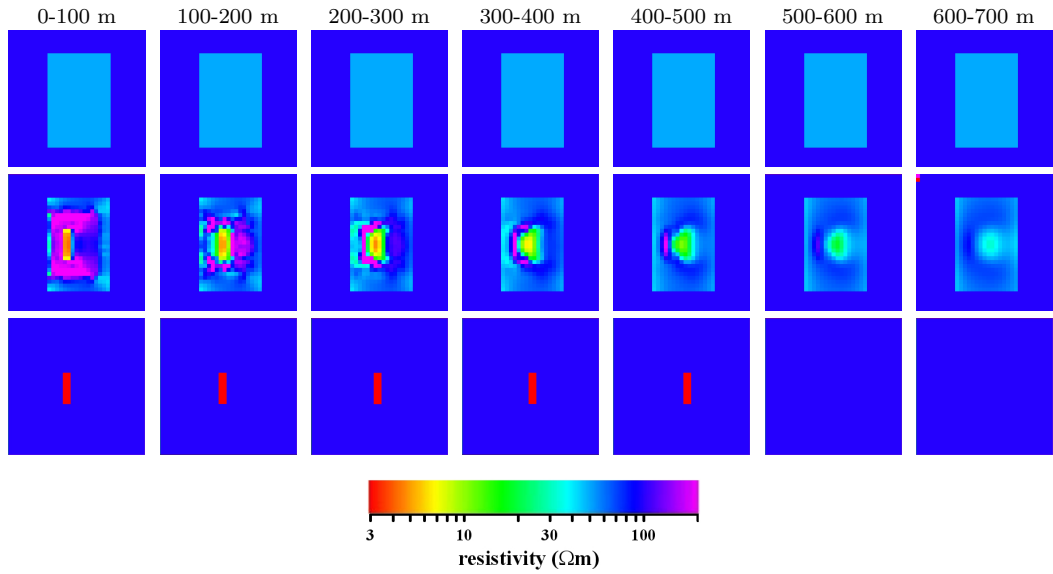
Figure 4.22.: Location of 168 MT sites.

Figure 4.23.: Inversion result with 168 MT sites and 10-Hz responses. The row of panels presents 7 horizontal (x-y) slices through the model starting from the top (left) to the bottom (right). The upper row of panels presents the initial guess model, the middle row shows the image recovered, the lower row is for the true model.
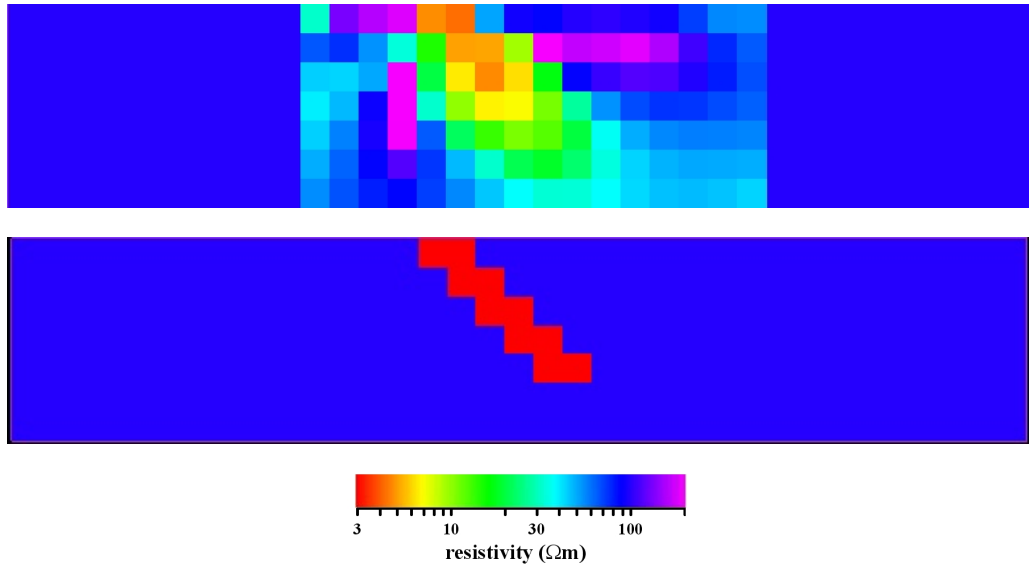
Figure 4.24.: Comparison for a central (x-z) cross-section. The upper panel presents the inversion result, whereas the lower panel presents true model. 10-Hz responses at 168 MT sites were used.
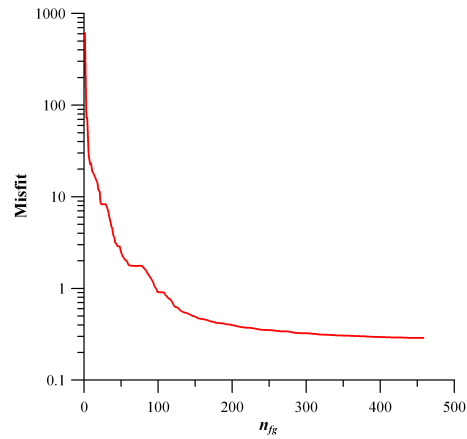
Figure 4.25.: Convergence of the inversion. 10-Hz responses at 168 MT sites were used. The inversion was terminated when no significant improvement could be made and when we reached a misfit $\varphi_d = 0.29$ which corresponds to rms of 2.5%.

through the middle of the model is shown in Figure 4.24. Interestingly, only a single frequency happens to be enough to more or less recover the true position and shape of the dyke.

The reason for such a good result is obvious - we use a very refined grid of MT sites. However, it should be mentioned that the value of the dyke's resistivity is overestimated by a factor of 1.5-2. We also can see remnants of the initial model at the edges of the inversion domain and some resistive artifacts, especially at the upper layer of the model. Figure 4.25 presents the convergence curve for this inversion. In our next experiment we consider how decreasing of the number of MT sites deteriorates the result of inversion.

4.2.3.2. 42 MT sites
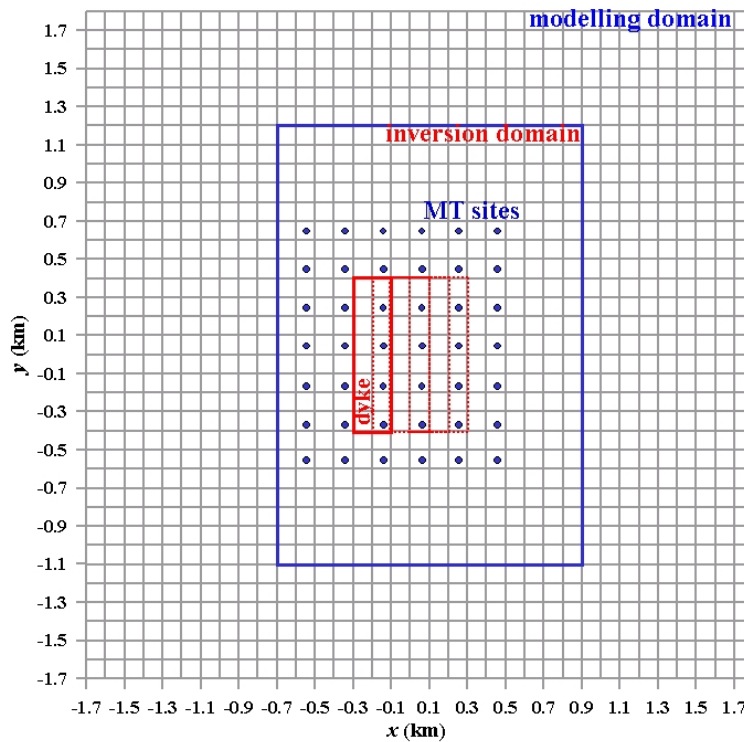
Figure 4.26.: Location of 42 MT sites.

In this experiment we cover the surface with 42 MT sites, as shown in Figure 4.26. Again we only invert 10 Hz responses with 1% added noise. The result of the inversion is shown in Figures 4.27 and 4.28. Similar to Figures 4.23 and 4.24, we get a blury image of the conductor at the lower part of the model, but now it extends
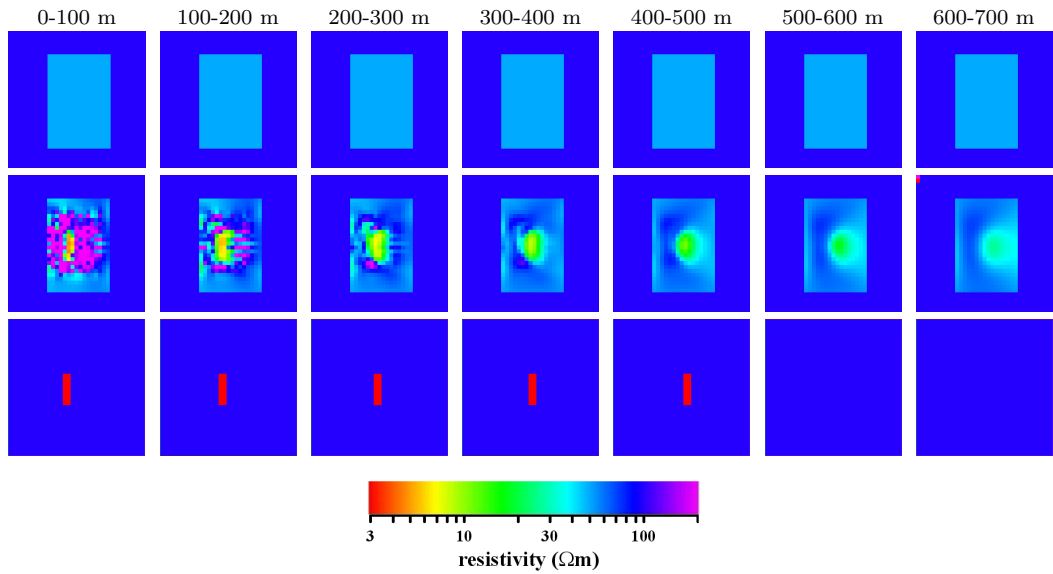
Figure 4.27.: Inversion result with 42 MT sites and 10-Hz responses. The row of panels presents 7 horizontal (x-y) slices through the model starting from the top (left) to the bottom (right). The upper row of panels presents the initial guess model, middle row shows the image recovered, the lower row is for the true model.
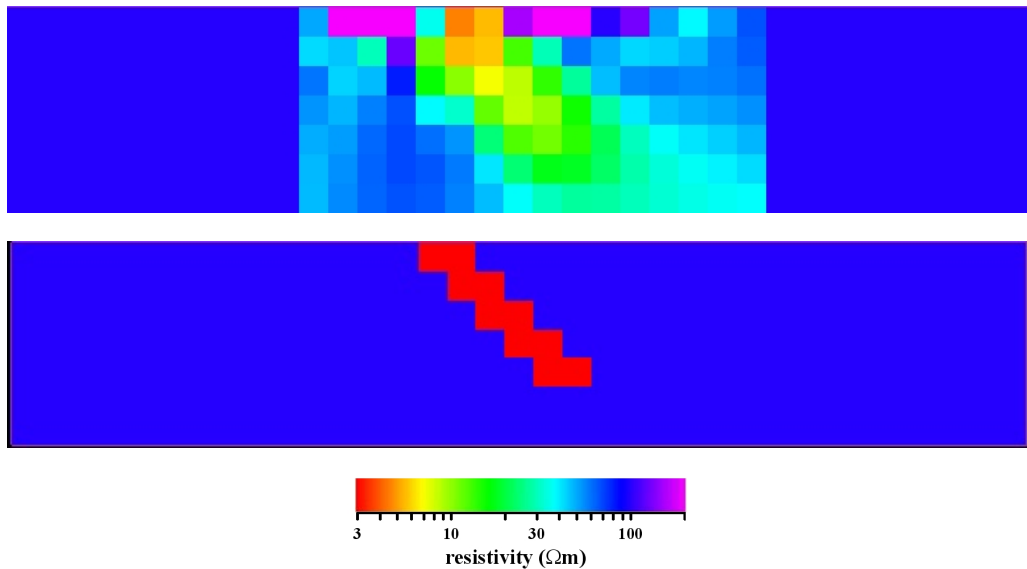

Figure 4.28.: Comparison for a central (x-z) cross-section. The upper panel presents the inversion result, whereas the lower panel presents true model. 10-Hz responses at 42 MT sites were used.

slightly deeper. We also obtained a lot of strange resistive artifacts, especially in the very first layer. From the figures we can see that although the shape of the dyke is
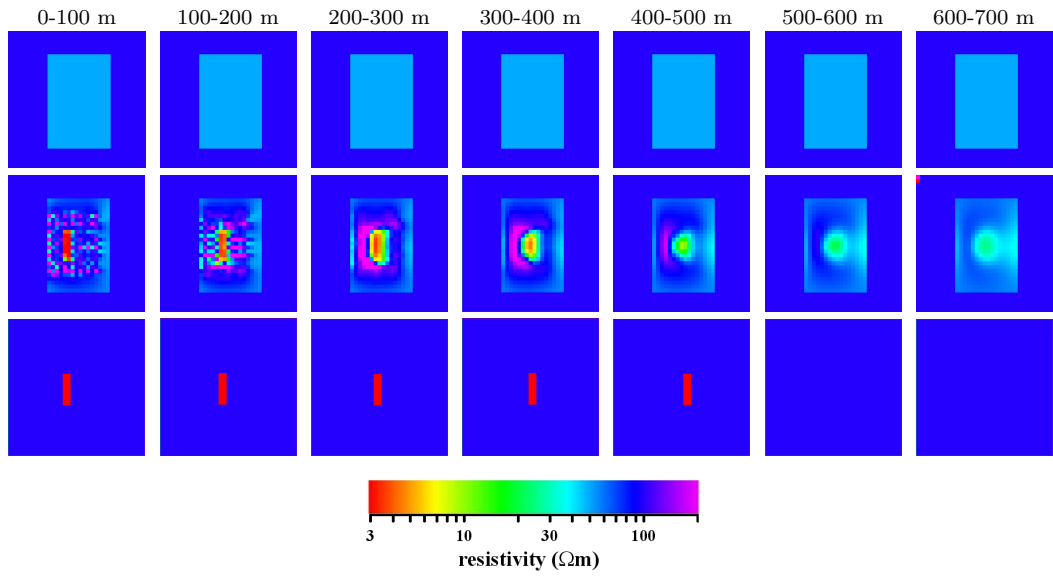
Figure 4.29.: Inversion result for 42 MT sites and 4 frequencies. The row of panels presents 7 horizontal (x-y) slices through the model starting from the top (left) to the bottom (right). The upper row of panels presents the initial guess model, the middle row shows the image recovered, the lower row is for the true model.
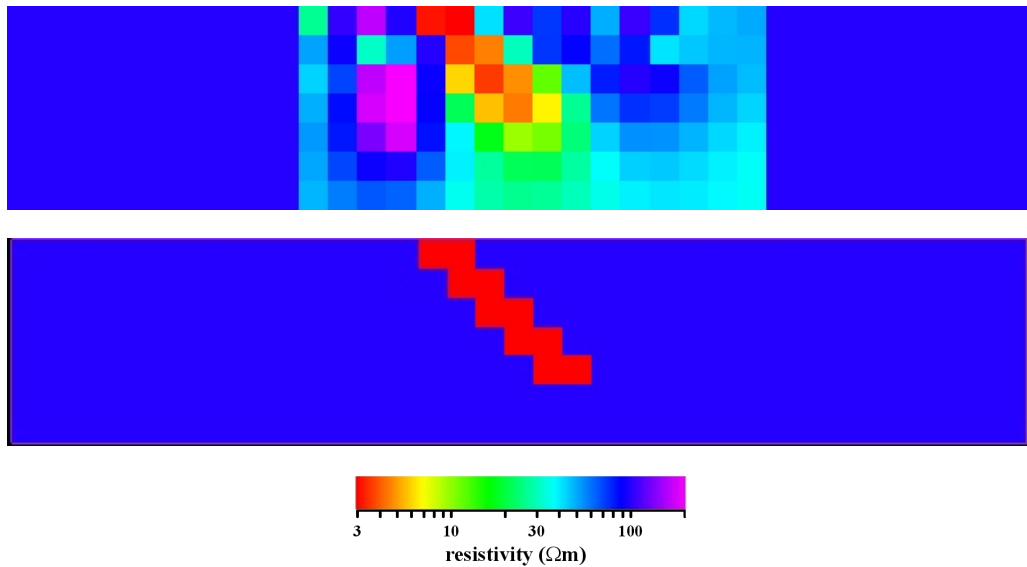

Figure 4.30.: Comparison for a central (x-z) cross-section. The upper panel presents the inversion result, whereas the lower panel presents the true model. 42 MT sites and 4 frequencies were used.

recovered, the upper part of it is shifted to the right by one cell. The first obvious explanation is that there are no data that covers the uppermost left margin of the
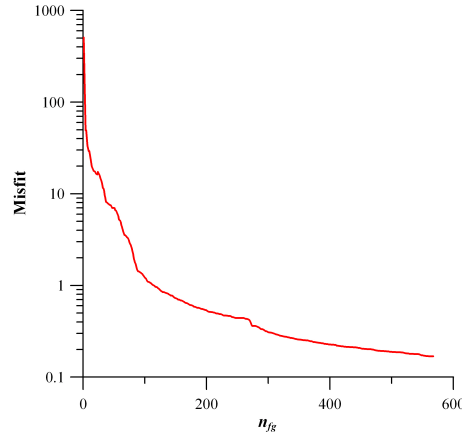
Figure 4.31.: Convergence of the inversion. 42 MT sites and 4 frequencies were used. The inversion was terminated when φ_d drops to 0.18, which corresponds to rms of 2%.

dyke.

We analyze whether increasing the number of frequencies helps to obtain a more accurate image. So we repeat the experiment with data at $N_T = 4$ frequencies of 1000, 100, 10 and 1 Hz and plot the result in Figures 4.29 and 4.30, and convergence curve in Figure 4.31. Not surprisingly we obtain much better result and this time the shape, position and even the value of the conductivity of the dyke are accurately recovered. The bottom of the dyke is now better resolved and we obtain much less resistive artifacts at the top. One can conclude that an increased number of frequencies, involved in inversion, helps a lot to improve the inversion result.

So far we dealt with only a relatively simple problem with around 3000 unknown conductivities. Although the results are promising they only give a first indication of the reliability and stability of the method. Hence, more complicated situations are studied below.

4.2.4. Two adjacent blocks

This section is very important for the whole work. Running ahead, let us state that this model for the first time allowed us to realize a problem that is crucial for reliable inversion of 3D MT dataset. The below experiments imply that Tikhonov-type regularization, which we included in our inversion solution, in certain cases is not powerful enough to suppress the non-smoothness of the resistivity image, especially for the upper part of the model. In order to construct reliable resistivity images
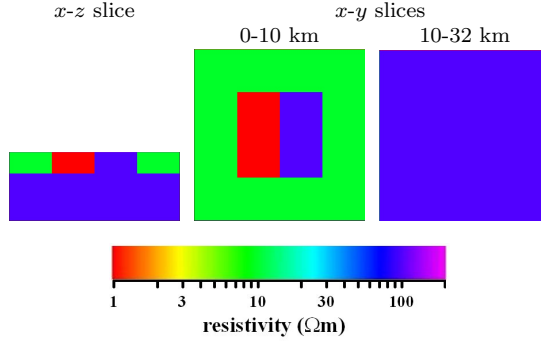
Figure 4.32.: The synthetic test model. The left most panel presents a vertical (x-z) slice through the middle of the model. The other two panels show horizontal (x-y) slices for two ranges of depths, 0-10 km and 10-32 km.

one has to put more strong constraints on the model parameters, stronger than those imposed by traditional Tikhonov-type regularization. In Chapter 5 we suggest different types of the preconditioners in our inversion to overcome this problem.

This more complex model is somewhat famous. It was previously considered in various 3D forward modelling papers (Wannamaker, 1991; Mackie *et al.*, 1994; Avdeev *et al.*, 1997, among others). Moreover, the inversion code by Siripunvaraporn *et al.* (2005) was also tested using this model. The model consists of resistive and conductive blocks buried in a two-layered earth. The horizontal and vertical slices presented in Figure 4.32 completely describe the model.

To select the appropriate frequency range for the inversion, we perform a simple sensitivity analysis. This analysis involves the comparison of apparent resistivity, ρ^{app}, and phase, ϕ, curves calculated for 4 two-layered models, constructed from the true and initial guess models used in the inversion. Resistivity values of the 10-km upper layer for these 1D models are 1, 10, 50 and 100 Ωm, respectively, while resistivity of the lower layer is 100 Ωm. The 1D curves are shown in Figure 4.33 as a function of period. From the figure, we can see that the frequency range from 10^{-4} to 10^{-1} Hz is appropriate in order to sense the important parts of the true model. Although we only start to sense the 100 Ωm lower layer for 1 Ωm (red) curve at the frequency of 10^{-4} Hz, this frequency is the realistic lower limit for the long period MT data. Note that Siripunvaraporn *et al.* (2005) used higher frequencies of 10^{-3}, 10^{-2}, 10^{-1}, 1 and 10 Hz.

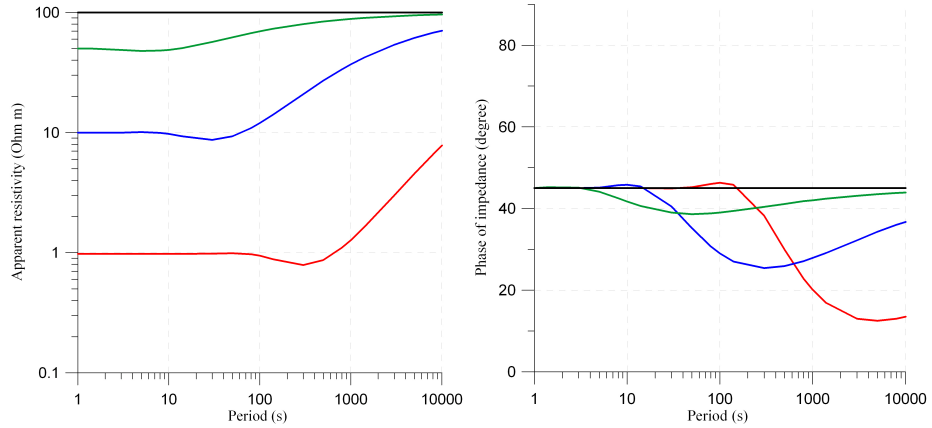We perform a set of experiments for the model shown in Figure 4.32. These are described in the following sections.

Figure 4.33.: Apparent resistivity and phase curves for 4 different two-layered models. These models have the resistivity of 100 Ωm for the lower layer, while the resistivity values of the 10-km upper layer are 1 (red), 10 (blue), 50 (green) and 100 Ωm (black), respectively.

4.2.4.1. Coarse numerical grid

In this section we use a coarse grid for the horizontal dimensions, we will refine this grid in the next Section 4.2.4.2.

First we choose an inversion domain of $N_x \times N_y \times N_z = 20 \times 20 \times 9 = 3,600$ rectangular cells with $dx = dy = 4000$ m. The inversion domain volume reaches a depth of 32 km, and the modelling domain coincides with the inversion domain.

400 MT sites.

For our first experiment with this grid we cover the surface ($z = 0$) of the inversion domain with 400 MT sites ($N_S = 400$), located at the centres of a homogeneous $n_x \times n_y = 20 \times 20$ grid, with 4000 m distance between adjacent nodes (see Figure 4.34). For these MT sites we simulated data at 3 frequencies of 0.01, 0.0033 and 0.001 Hz ($N_T = 3$). We again added 1% noise to the simulated data. We also used the stabilizer φ_s and the technique of gradually diminishing regularization parameter λ (see Section 4.1.2.1) in the inversion. The result of the inversion is shown in Figures 4.35 and 4.36 together with the true and initial guess models. It should be noted here that the initial guess model has the conductivity of 50 Ωm in all cells of the inversion domain, assuming that outside conductivity coincides with the true background. For this model the true background is just a two-layered structure with a 10-km thick 10 Ωm layer on the top of the 100 Ωm halfspace.

Comparing the recovered image with the true model, we obtain a satisfactory result: the shape and position of the blocks are recovered. The value of the resistiv-
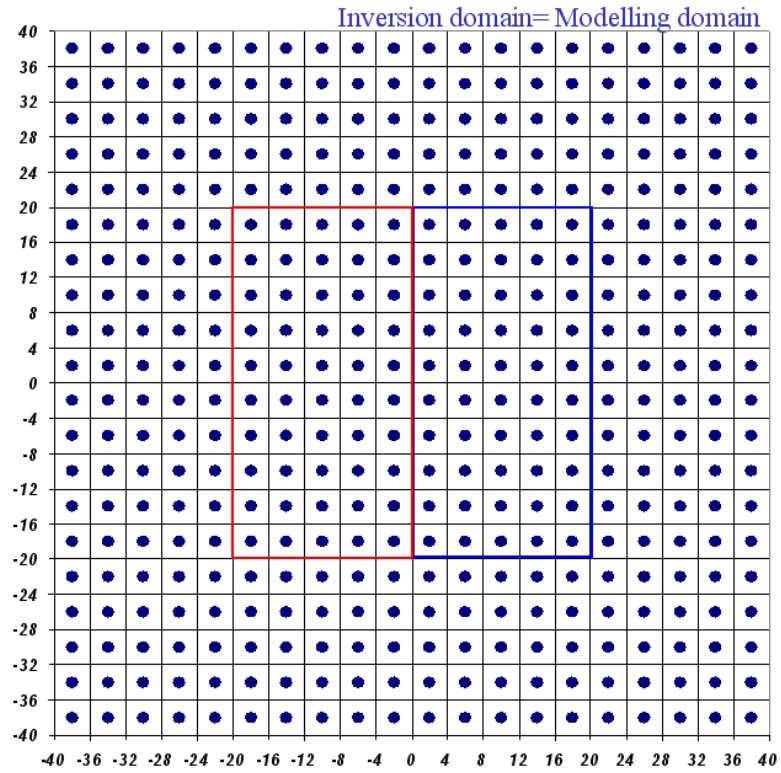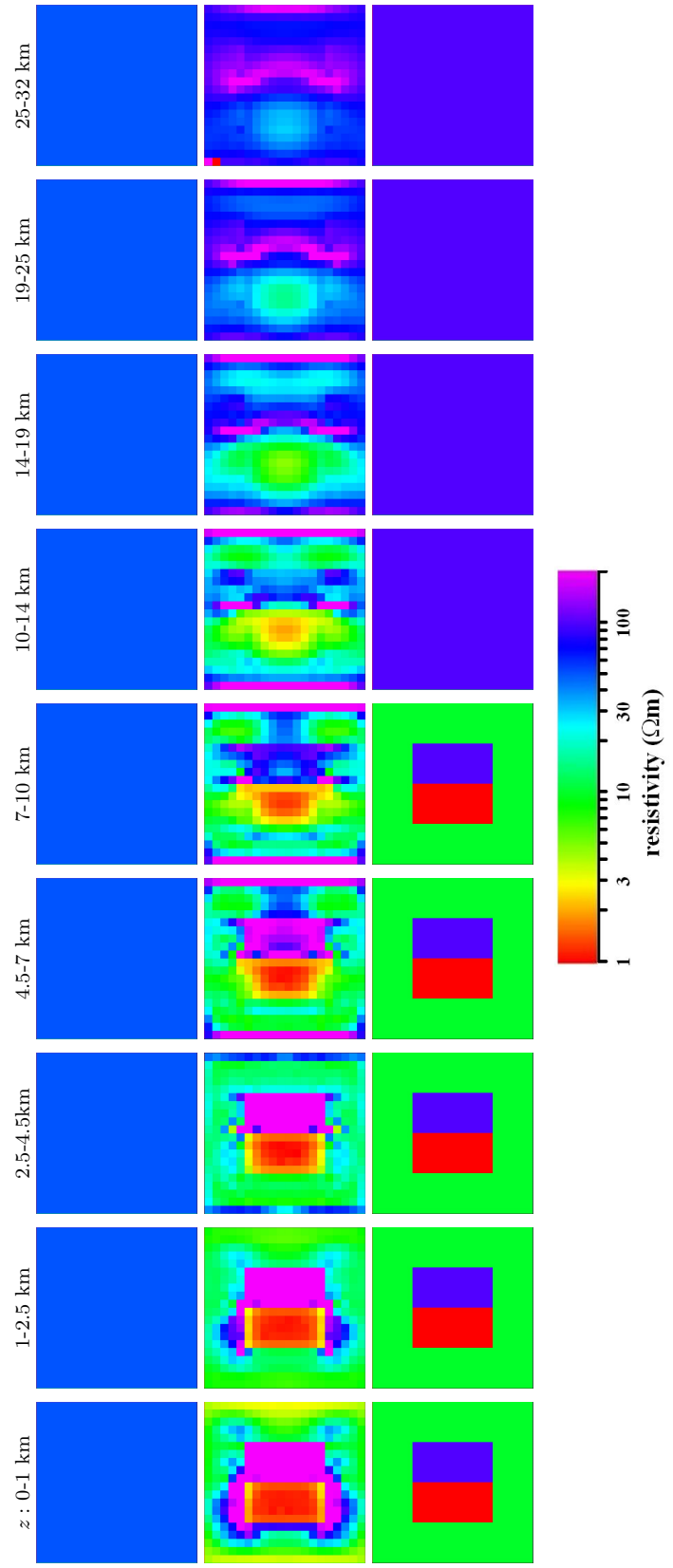
Figure 4.34.: Location of 400 MT sites.

Figure 4.35.: Result of the inversion for 400 MT sites and 3 frequencies. Each row presents nine horizontal $(x - y)$ slices through the model starting from the top (left) to the bottom (right). 1st row corresponds to the initial guess model, 2nd to the result of the inversion and 3rd to the true model.
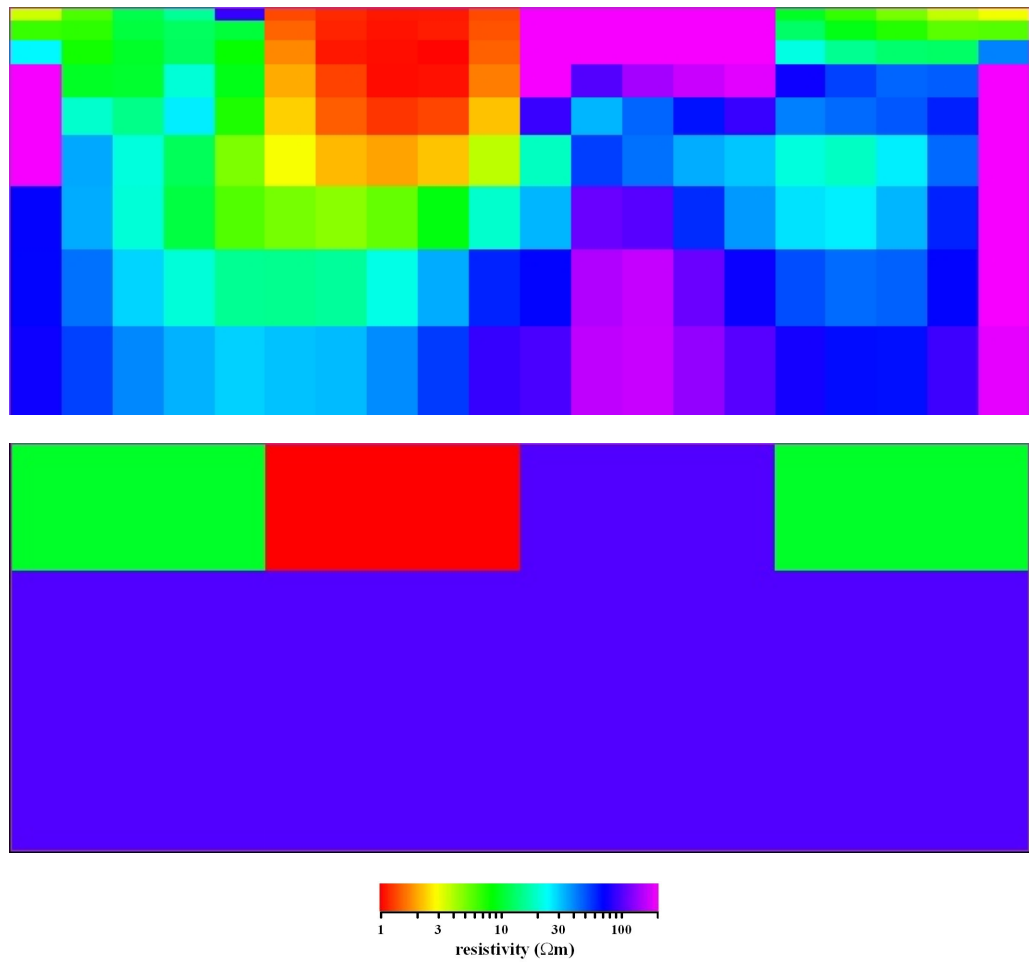
Figure 4.36.: Comparison for a central (x-z) cross-section. The upper panel presents the inversion result, whereas the lower panel presents true model. 400 MT sites and 3 frequencies were used.

ity for the conductive block is retrieved correctly, although it is overestimated for the resistive block. As usual for MT inversion, the position of the bottom of the conductive block is somewhat obscured.
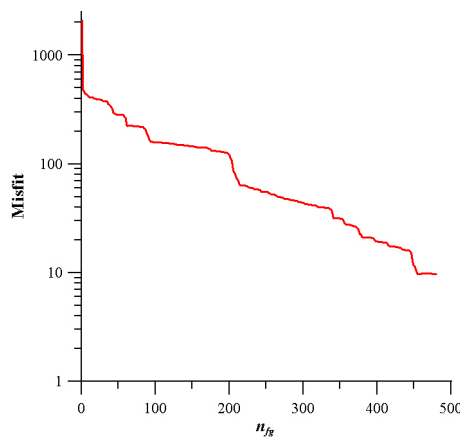

Figure 4.37.: Convergence of the inversion. 400 MT sites and 3 frequencies were used. The inversion was terminated when φ_d drops to 9.7.

We stopped the inversion process when the value of the data misfit φ_d could not be improved anymore and it dropped to 9.7. The whole convergence curve is shown in Figure 4.37. A single calculation of the penalty function together with its gradient for this experiment takes about 7 minutes on a serial PC, resulting in a total time of ≈ 50 hours.

80 MT sites.

We now diminish the number of MT sites used for the inversion to 80. These sites are randomly placed, however, we prevent two sites from being placed in directly adjacent cells. The locations of these MT sites are shown in Figure 4.38. Everything else was kept as in the previous experiment, we only changed the number of MT sites.

Figures 4.39 and 4.40 present the result of the inversion together with the true and initial guess models. We observe that the recovered image is very different from the true model. It has a very erratic behaviour, especially for the upper part of the model, with a lot of artificial structure. This result cannot be considered satisfactory. It is interesting that if we plot the locations of the MT sites on top of the recovered image (see Figure 4.41) we see that reasonable resistivity values occur exactly for those cells that contain MT sites. For these selected cells it is obviously possible to retrieve the underground structure, at the same time it is absolutely impossible to utilize the resistivity of the other cells.
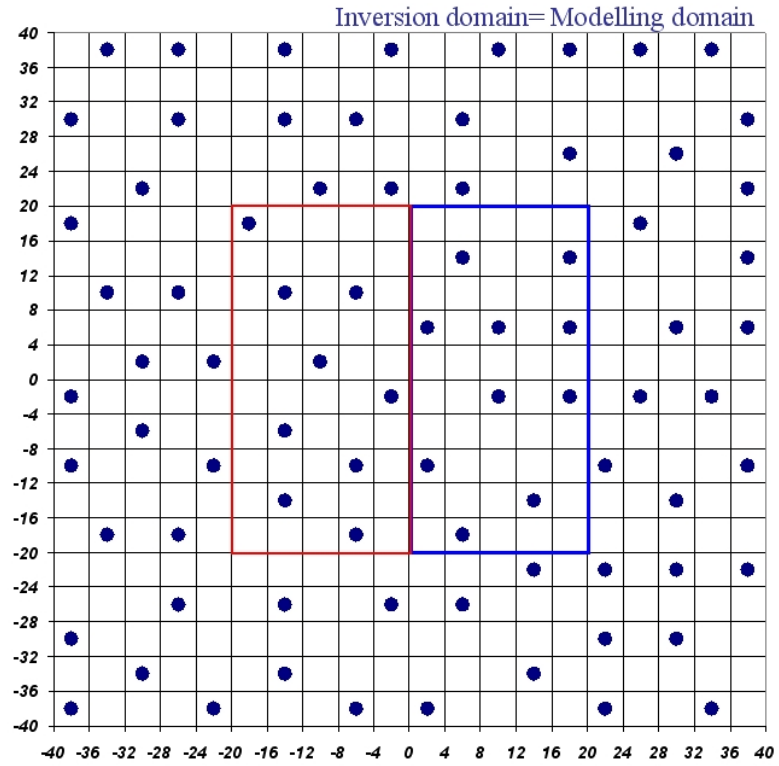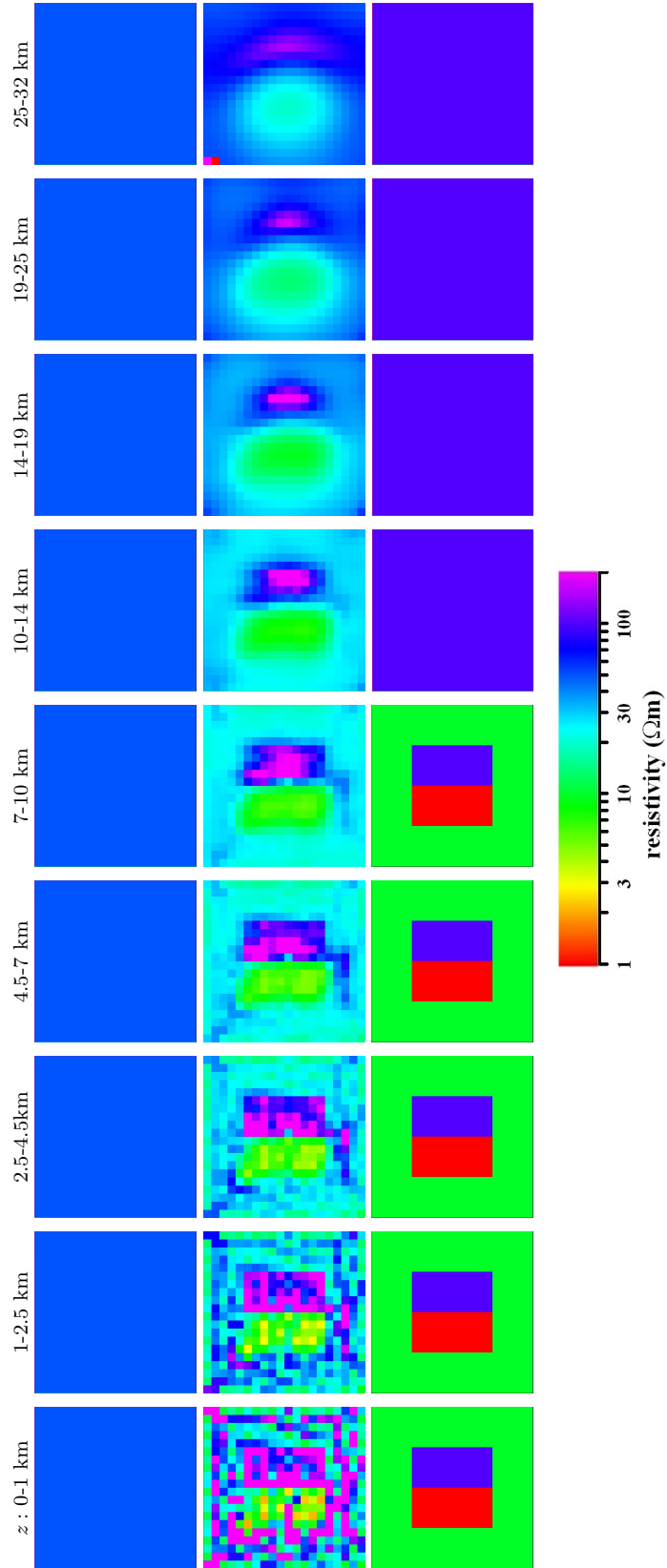
Figure 4.38.: Location of 80 MT sites.

Figure 4.39.: Result of the inversion. Each row presents nine horizontal ($x-y$) slices through the model starting from the top (left) to the bottom (right). 1st row corresponds to the initial guess model, 2nd to the result of the inversion and 3rd - the true model. 80 MT sites and 3 frequencies were used.
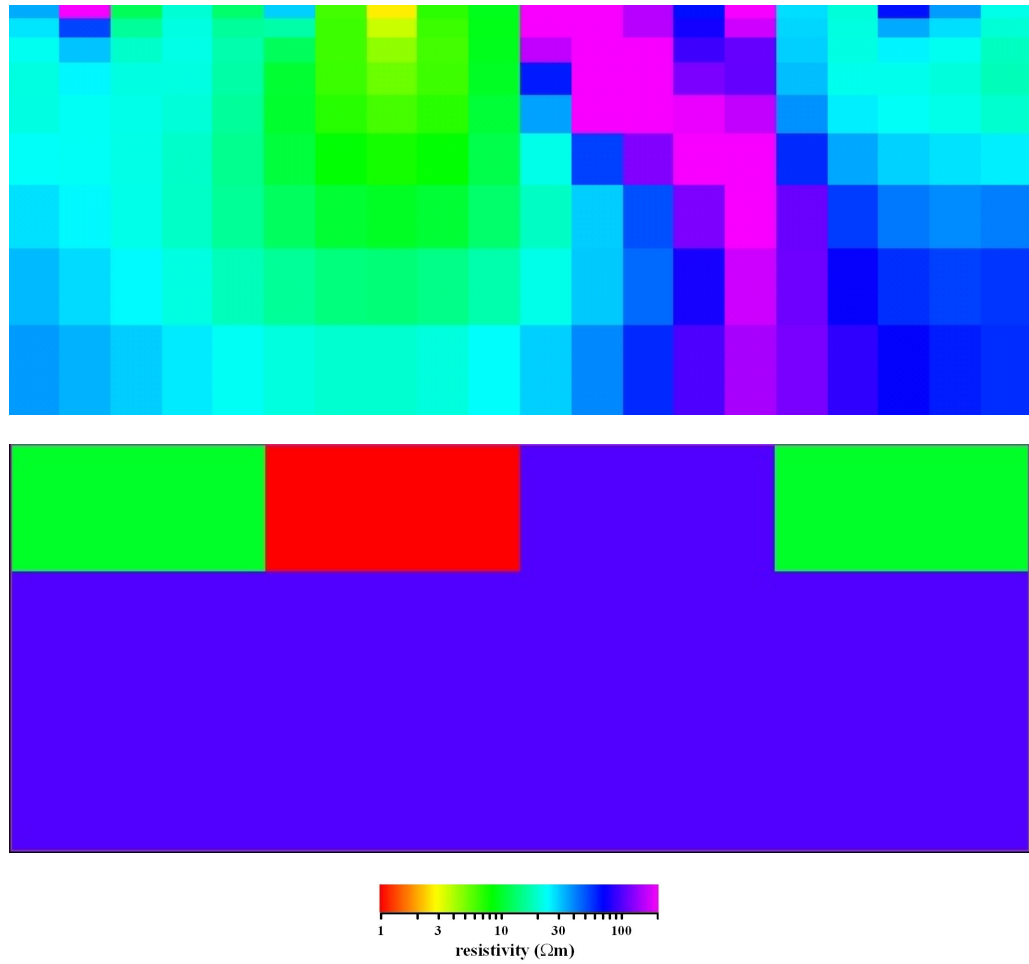
Figure 4.40.: Comparison for a central (x-z) cross-section. The upper panel presents the inversion result, whereas the lower panel presents true model. 80 MT sites and 3 frequencies were used.
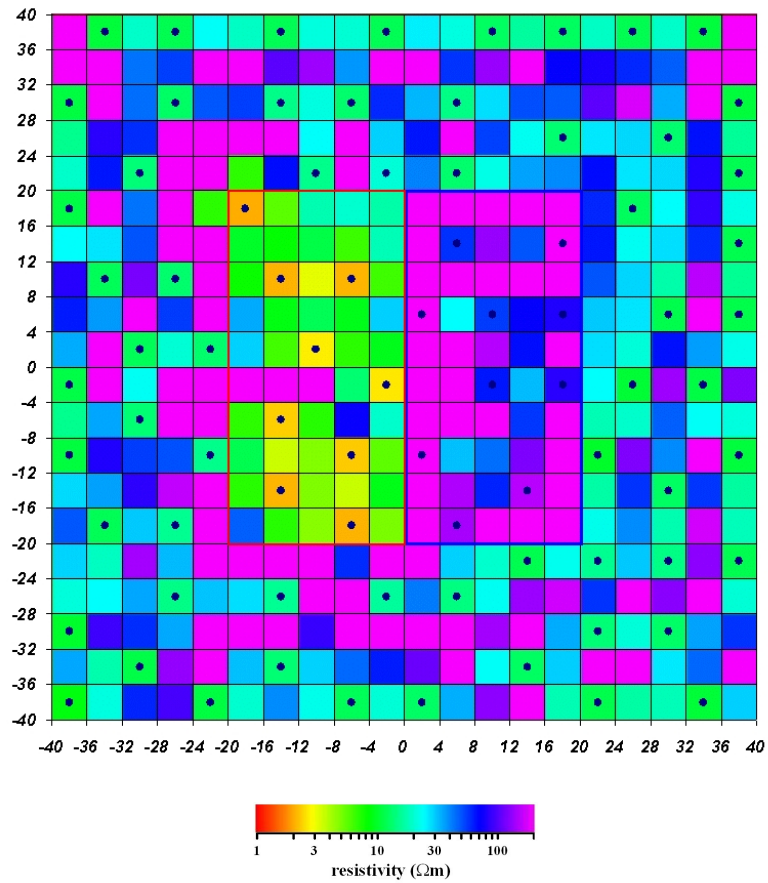
Figure 4.41.: The location of 80 MT sites plotted on top of the upper layer of the recovered image.

To better understand how our inversion works, we refine the grid, hoping that the above result is just a consequence of a too coarse grid used for forward modelling.

4.2.4.2. Refined numerical grid

We chose our inversion domain to be $N_x \times N_y \times N_z = 40 \times 40 \times 5 = 8000$ with $dx = dy = 2000$ m, compared with $dx = dy = 4000$ m in the previous section. Again the modelling domain coincides with the inversion domain. In order to save computational time we invert only for the first 5 layers up to 10 km depth.

1444 MT sites.
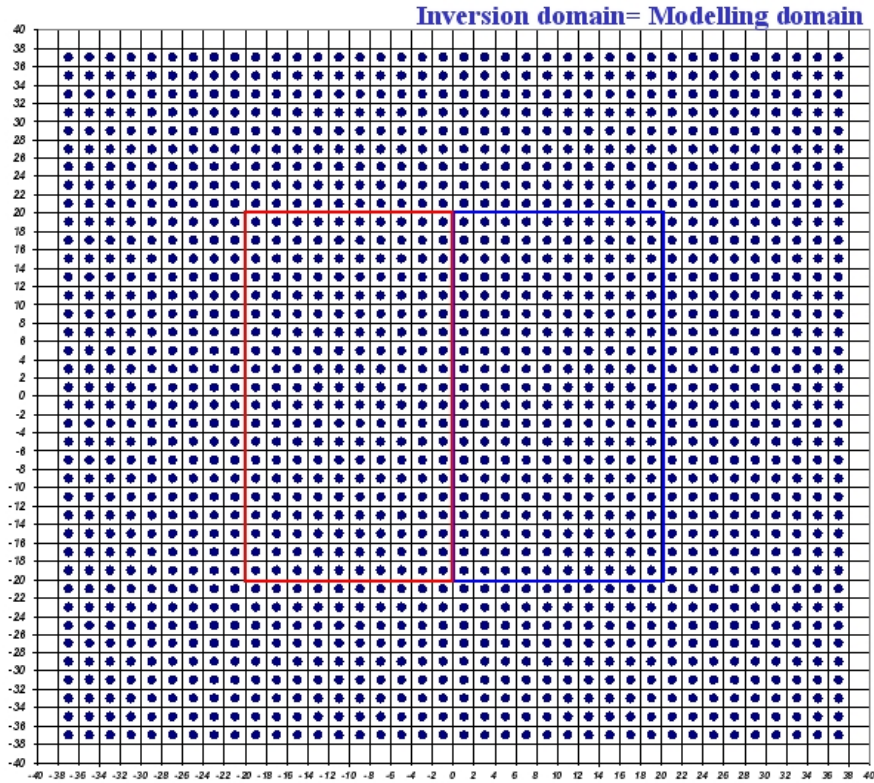
Figure 4.42.: Location of 1444 MT sites.

For the first experiment with this refined grid we cover the surface of the inversion domain with 1444 MT sites ($N_S = 1444$). The exact locations of the sites are shown in Figure 4.42. For these MT sites we simulated data at 3 frequencies of 0.033, 0.01 and 0.0033 Hz ($N_T = 3$), slightly higher than in the previous setup. We again add 1% noise to the simulated data. For the initial guess model we assign a resistivity value of 50 Ωm to all the cells of the inversion domain. The inverted model is shown

z : 0-1 km   1-2.5 km   2.5-4.5km   4.5-7 km   7-10 km
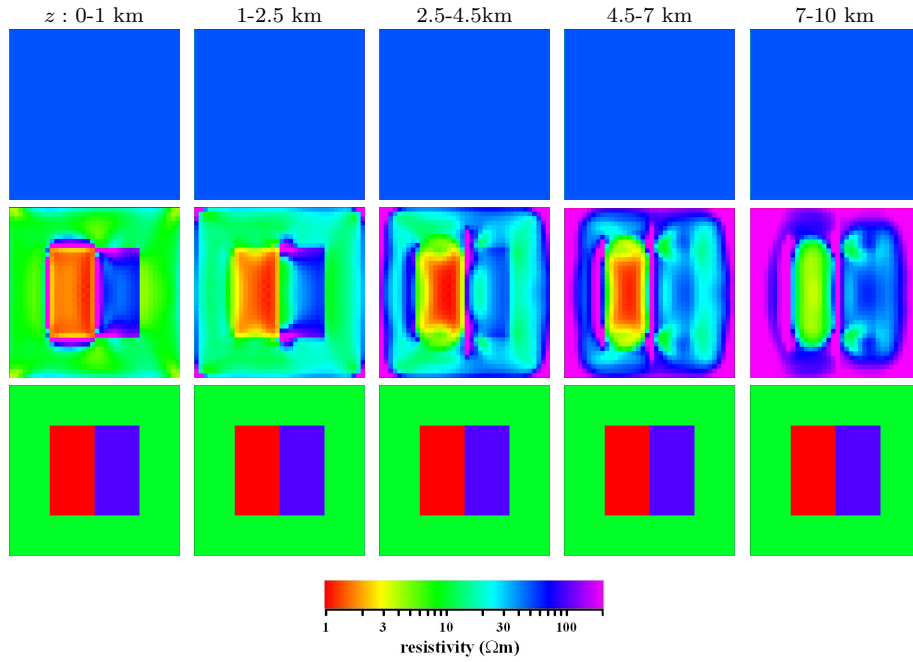
resistivity (Ωm)

Figure 4.43.: 3D electrical resistivity models. Each row presents five horizontal ($x-y$) slices through the model starting from the top (left) to the bottom (right). 1st row corresponds to the initial guess model, the 2nd row - to the result of the inversion and the 3rd - to the true model. 1444 MT sites and 3 frequencies were used for the inversion.

resistivity (Ωm)
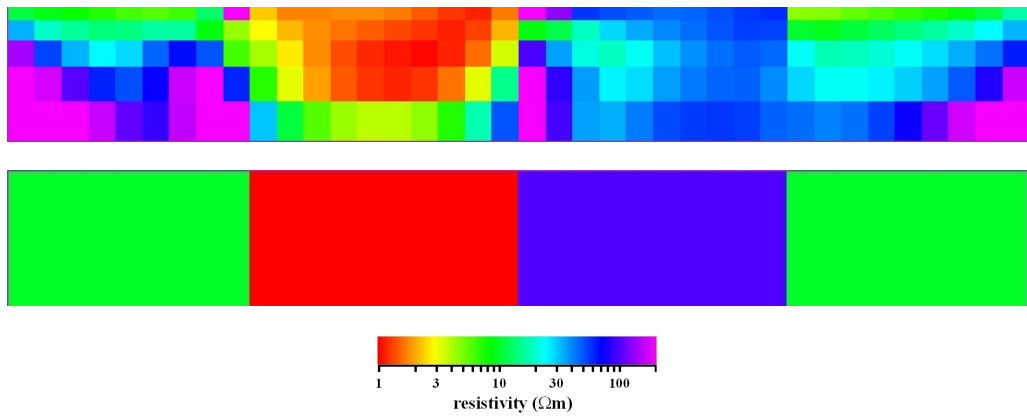
Figure 4.44.: Comparison for a central (x-z) cross-section. The upper panel presents the inversion result, whereas the lower panel presents the true model. 1444 MT sites and 3 frequencies were used.

on Figure 4.43 and 4.44 along with the true and initial guess models.

As in Section 4.2.4.1 for the coarse grid with a dense site coverage, we obtain a very satisfactory result. From the figures, we can see that the position and the true

resistivity of the anomalies are retrieved correctly. Although the boundaries of the anomalies are not so sharp, they are much sharper than for the coarse grid and these smooth transitions are the normal effect of the regularization. The background resistivity of 10 Ωm is not well resolved at depth, if compared with the result obtained on the coarse grid. This can be explained by the fact that for this inversion we used higher frequencies.
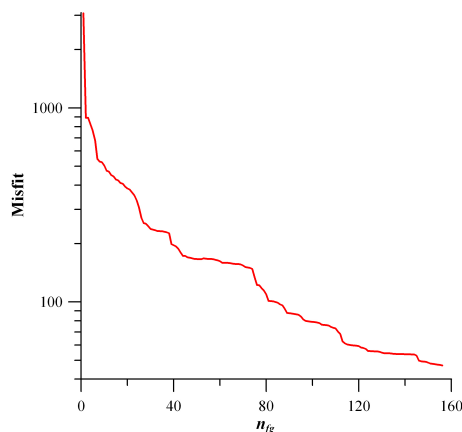
Figure 4.45.: Convergence of the inversion. The inversion was terminated when we reached a data misfit $\varphi_d = 47$. 1444 MT sites and 3 frequencies were used.

The inversion process was stopped when φ_d dropped to 47. The full convergence curve is shown in Figure 4.45. For the grid used in this experiment a single calculation of the penalty function together with its gradient takes about 6 minutes on a serial PC. Even though we used finer grid, the smaller number of layers in z-direction reduced the computational time (we needed 7 minutes for a single calculation of the penalty function together with its gradient for the coarse grid).

It is also interesting to compare the results obtained for various numbers and values of frequencies involved in the inversion. In Figures 4.46 and 4.47 we compare the recovered images when 1, 2 or 3 frequencies are used in the inversion. When we use just one period of 100 s we can resolve surprisingly well the resistivity, position and shape of the conductive anomaly. This anomaly extends all the way to the bottom of the inversion domain, as it does for the true model. The shape and position of the resistor are also retrieved, however its resistivity is overestimated. The background resistivity cannot be resolved for this single frequency. If we use period of 300 s instead of 100 s we again can retrieve the conductor quite well, however the resistive anomaly and the 10 Ωm background are full of strange artifacts. To use 2 or 3 fre-

96
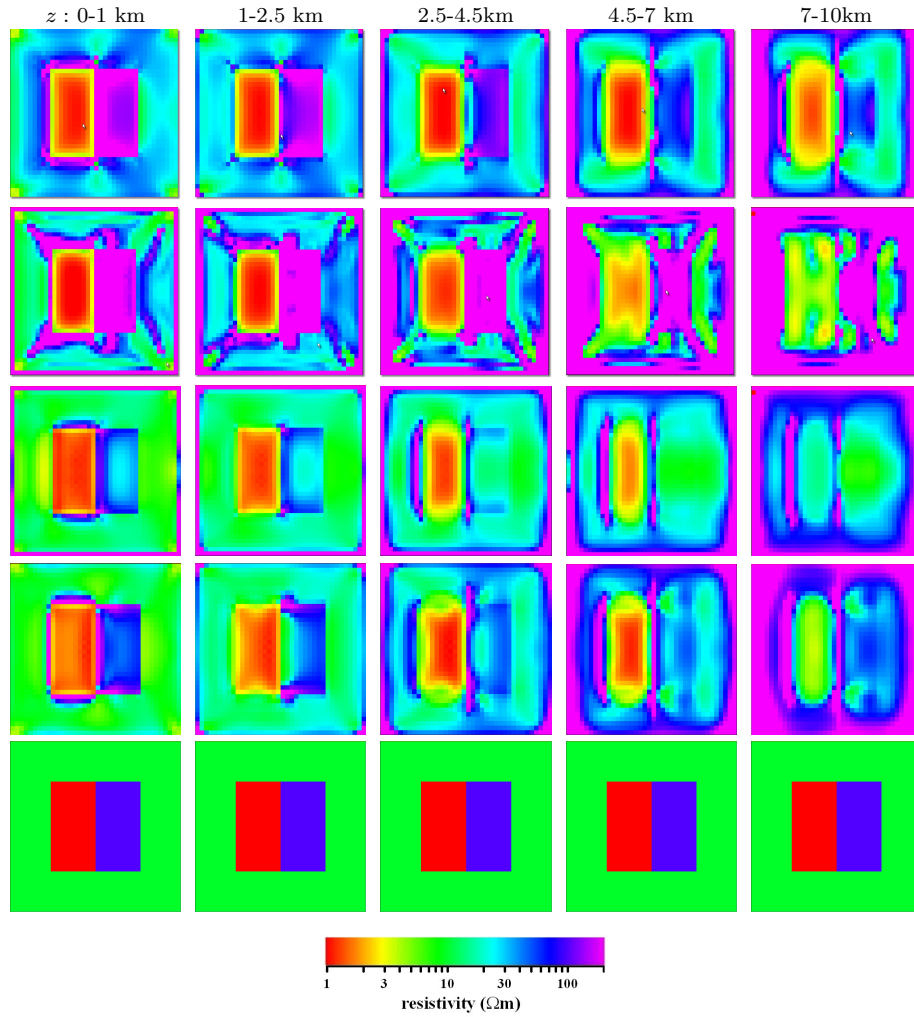
Figure 4.46.: Comparison of the results of inversions with different number of frequencies. Each row presents five horizontal $(x - y)$ slices through the model starting from the top (left) to the bottom (right). The 1st row corresponds to the inversion result obtained using only 1 frequency of 0.01 Hz, a data misfit of $\varphi_d = 75$ was reached in this case, the 2nd row presents the result for a frequency of 0.0033 Hz and we obtained $\varphi_d = 33$, the 3rd row shows the result when 2 frequencies of 0.01 and 0.033 Hz were used, there $\varphi_d = 53$, in the 4th row - we used 3 frequencies of 0.0033, 0.01 and 0.033 Hz and the data misfit dropped to $\varphi_d = 47$. Finally, the 5th row displays the true model. We used 1444 MT sites for these results.

quencies helps to resolve the background resistivity, especially for the 3 upper layers. The conductor is reasonably well resolved for both of these cases and we can better see the resistor if 3 frequencies are used. The main conclusion from the comparison
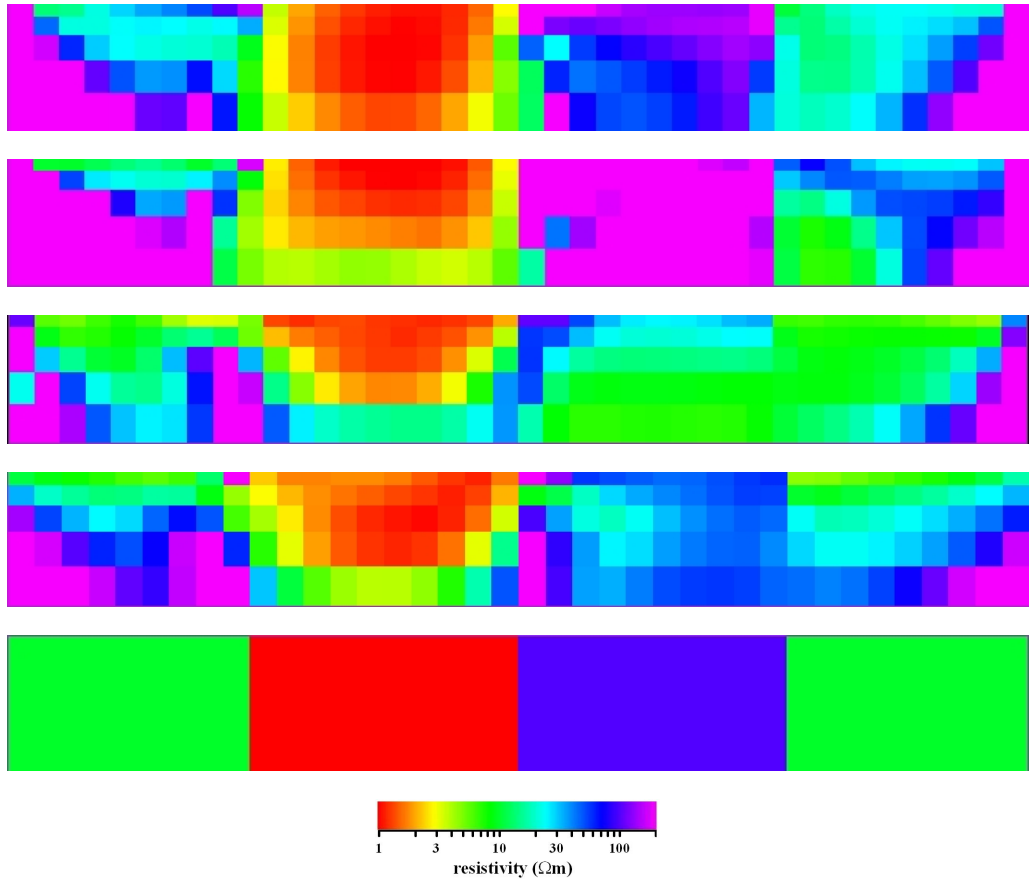
Figure 4.47.: Comparison for a central (x-z) cross-section. The four upper panels present the inversion results for the various numbers of frequencies used in the inversion, whereas the lower panel corresponds to the true model. Please see the caption for the Figure 4.46 for the used frequencies and the obtained values of the data misfits φ_d. 1444 MT sites were used.

is that the increased number of frequencies again, as in Subsection 4.2.3.2, helps to improve quality of the inversion.

Let us see how the problem found with the coarse grid and few sites manifests itself for the case of the refined grid. For this analysis we diminish the number of MT sites used in the inversion from 1444 to 500.

500 MT sites.

We randomly choose the locations of the MT sites, these are shown in Figure 4.48 together with the modelling cells. Due to the random distribution it happened that there are regions where MT sites grouped closely together and regions with hardly any sites. This observation is important for understanding the inversion results and is a typical situation in a real field survey. The grid was kept as in the previous
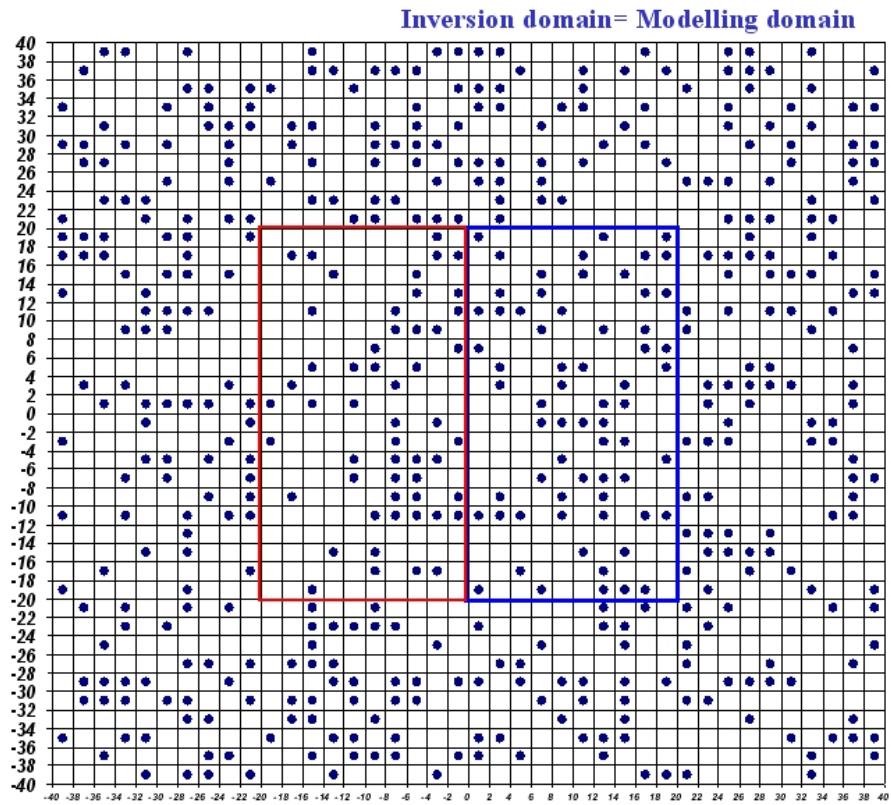
Figure 4.48.: Location of 500 MT sites.
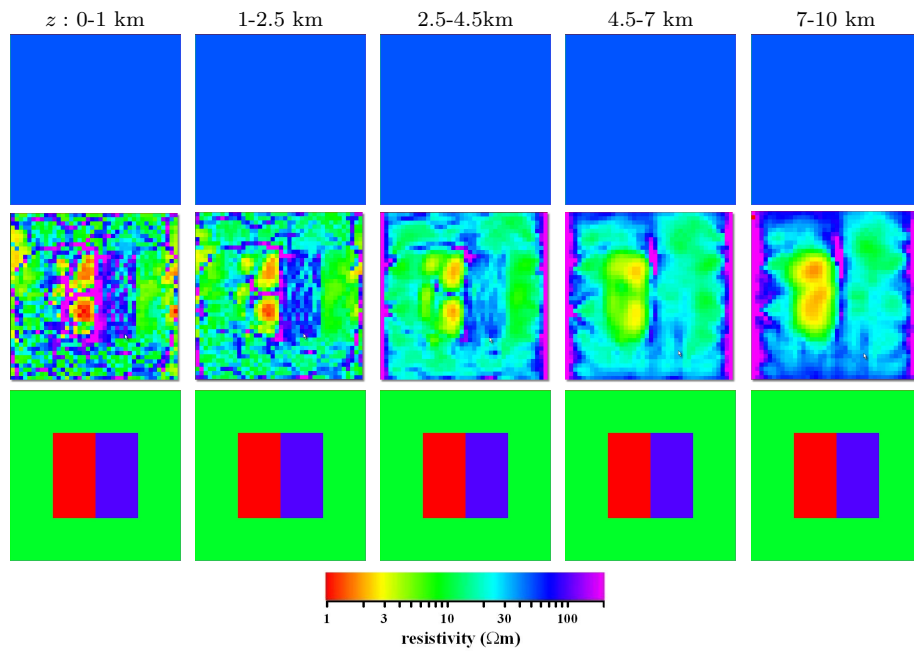
Figure 4.49.: Result of the inversion. Each row presents five horizontal $(x - y)$ slices through the model starting from the top (left) to the bottom (right). 1st row corresponds to the initial guess model, 2nd to the result of the inversion and 3rd - the true model. 500 MT sites and 4 frequencies of 0.033, 0.01, 0.0033 and 0.001 Hz were used.
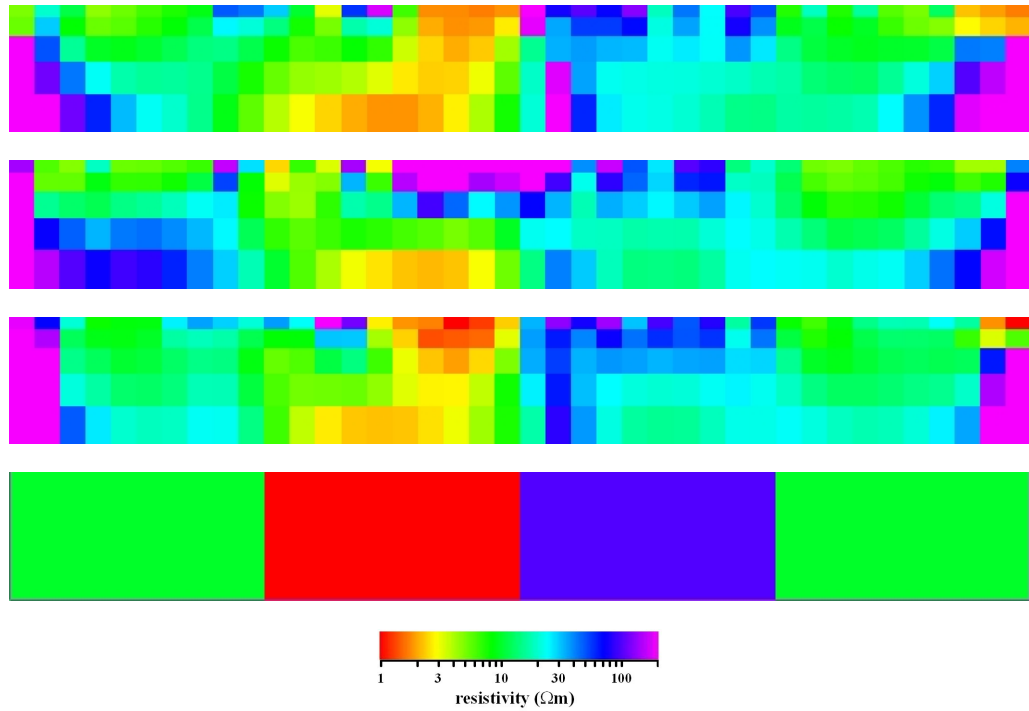
Figure 4.50.: Comparison for (*x-z*) cross-sections. The recovered resistivity image is presented for north (upper panel), central (2nd panel), south (3rd panel) profiles. The lowermost presents the true image. 500 MT sites and 4 frequencies were used.

experiment with 1444 MT sites.

For the inversion we used data calculated at 4 frequencies of 0.033, 0.01, 0.0033 and 0.001 Hz ($N_T = 4$). Figures 4.49 and 4.50 present the result of the inversion together with the true and initial guess models. From these figures we can see that the recovered image is different from the true model, except at the volumes located under regions with densely located sites. In sparsely covered regions the resistivity shows the erratic behaviour we already observed in some of the previous examples. Again the upper part of the model is particularly affected.

We plot the recovered image for the surface layer together with the locations of the MT sites in Figure 4.51. From this figure we can see that reasonable resistivity values are recovered exactly under the cells beneath the MT sites. For these selected cells it is possible to see the underground structure, at the same time it is difficult to reconstruct the resistivity elsewhere.

We present some thoughts and ideas about possible reasons for this phenomena in the next chapter.

102

Figure 4.51.: The location of 500 MT sites plotted on top of the upper layer of the recovered image.

Chapter 5.

Additional regularization

In this chapter we will investigate why our current solution for the 3D MT inverse problem sometimes cannot resolve the resistivity immediately beneath the surface, in regions that are not covered by MT sites. With this aim in mind, we write down an explicit formula for the first model update:
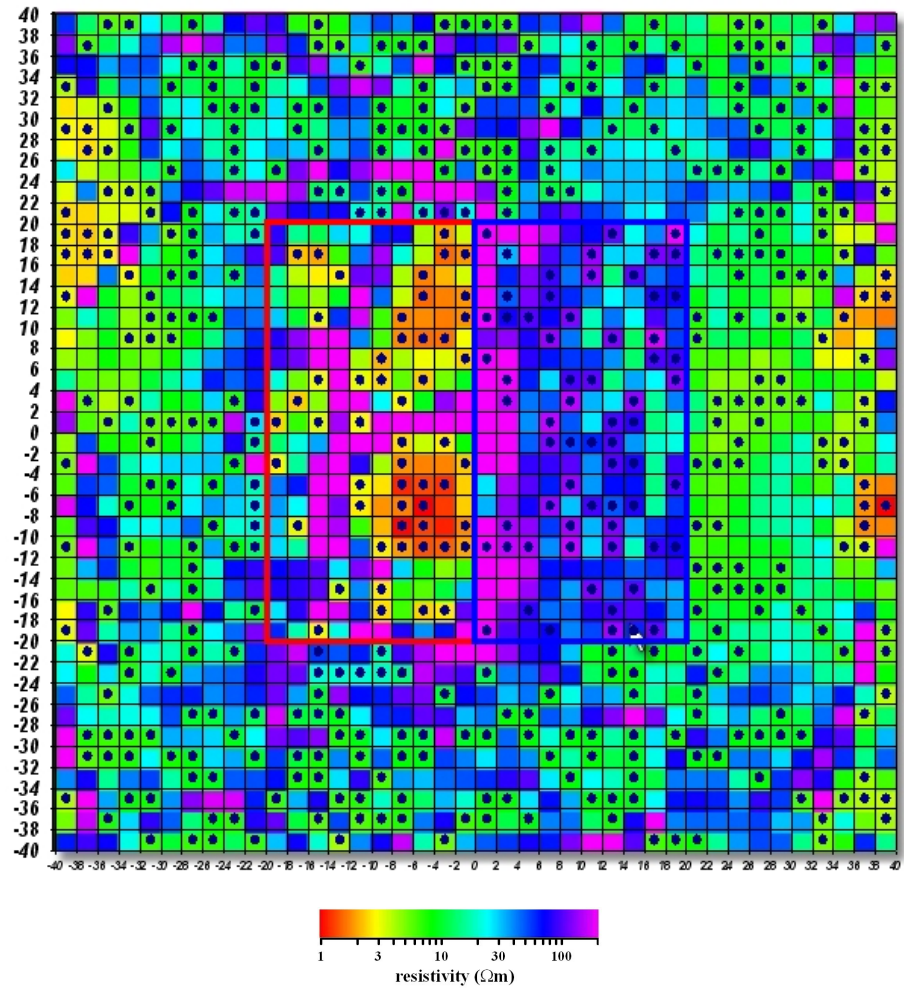
$$\sigma_k^{(1)} = \sigma_k^{(0)}(1 + \alpha p_k^{(0)}). \tag{5.1}$$

This expression straightforwardly follows from equation 2.27, if one recalls that $m_k^{(1)} = \sigma_k^{(1)}/\sigma_k^{(0)}$, $(k = 1, \dots, N)$ (see equation 4.5). Here $\sigma_k^{(0)}$ is the conductivity of the k-th cell of the initial guess model. Further,

$$p_k^{(0)} = -\sigma_k^{(0)} \left(\frac{\partial \varphi_d}{\partial \sigma_k} + \lambda \frac{\partial \varphi_s}{\partial \sigma_k} \right) \bigg|_{\boldsymbol{\sigma}=\boldsymbol{\sigma}^{(0)}}, \tag{5.2}$$

as follows from equations 2.21, 2.25, 2.28 and 2.31. Substituting equation 5.2 into equation 5.1, we get

$$\sigma_k^{(1)} = \sigma_k^{(0)} \left(1 - \alpha\sigma_k^{(0)} \left(\frac{\partial \varphi_d}{\partial \sigma_k} + \lambda \frac{\partial \varphi_s}{\partial \sigma_k} \right) \bigg|_{\boldsymbol{\sigma}=\boldsymbol{\sigma}^{(0)}} \right). \tag{5.3}$$

This expression for the first update $\sigma_k^{(1)}$ means that the smoothness of $\sigma_k^{(1)}$ is directly related to the smoothness of $\partial \varphi_d/\partial \sigma_k$. Indeed, equation 5.3 can be rewritten as

$$\sigma_k^{(1)} = \sigma_k^{(0)} - \alpha\sigma_k^{(0)2} \frac{\partial \varphi_d}{\partial \sigma_k}, \tag{5.4}$$

since in many cases the initial guess model $\boldsymbol{\sigma}^{(0)}$ is chosen as a uniform half-space and consequently $\partial \varphi_s/\partial \sigma_k|_{\boldsymbol{\sigma}=\boldsymbol{\sigma}^{(0)}} = 0$.

As an example of the first update, in Figure 5.1 we show the resistivities $\rho_k^{(1)} = 1/\sigma_k^{(1)}$ for the model example with two adjacent blocks described on page 89. In that example, 80 MT sites were inverted and the inversion domain was discretized by $N_x \times N_y \times N_z = 20 \times 20 \times 9 = 3,600$ rectangular cells. Note that these MT sites covered only 80 surface cells, leaving 320 surface cells uncovered.
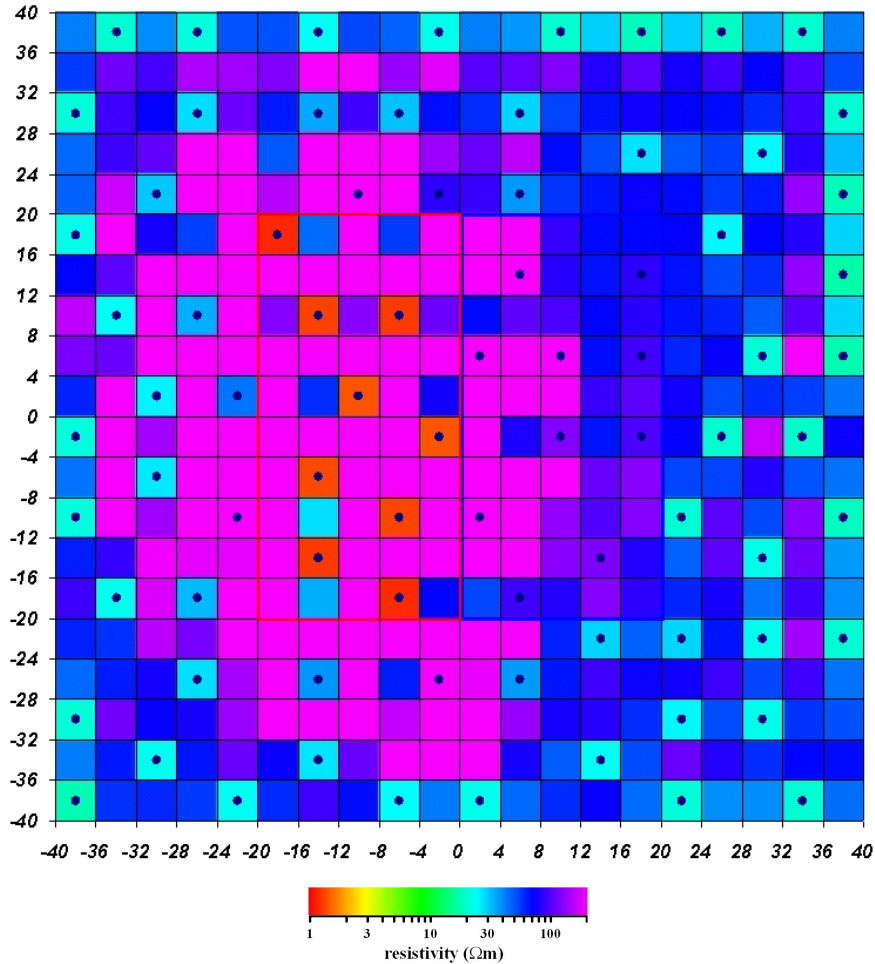
Figure 5.1.: Resistivity of the uppermost layer after the first iteration when starting from a homogeneous half-space. The resistivity values are proportional to the elements of the gradient. The locations of 80 MT sites are shown as black dots.

We can clearly see that the values of $\sigma_k^{(1)}$ are dramatically higher for the 80 cells covered with sites and nearly vanish for the other 320 cells. In other words, the first update $\boldsymbol{\sigma}^{(1)}$ looks very rough. Moreover, the smoothness of this image cannot be improved by Tikhonov-type regularization at all. This conclusion follows from equation 5.4, since the right hand side of the equation does not depend on φ_s. The

regularization may help only with improving this erratic image $\boldsymbol{\sigma}^{(1)}$ in the course of consequent iterations $\boldsymbol{\sigma}^{(n)}$. Our experience, and the examples considered in this work, demonstrate that this type of regularization does not always help, but its effectiveness depends on many factors.

Summing up, the singularity of the gradient $\partial\varphi_d/\partial\sigma_k$ in the vicinity of the MT sites introduces erratic structures to the model and this behaviour complicates the solution of the 3D MT inverse problem. This is particularly true with Newton-type optimization approaches that rely heavily on the gradients. It is surprising that, although the problem outlined above reflects the physics of the 3D MT inverse problem, it is not very well reported in literature, but only hinted at. A general solution is to put more constraints on the model conductivity values directly, rather than impose them through the Tikhonov-type stabilizer φ_s. As an example of such an approach, the paper by Siripunvaraporn *et al.* (2005) proposes to put additional constraints on the resistivity of the cells using the so-called model covariance matrix. This operation can be alternatively viewed as a change of unknowns. Gregory Newman, in private communication, has proposed to adjust the gradient using a Hessian matrix.

These two approaches may help us to eliminate the erratic behaviour at the upper part of the model sometimes observed for our currently implemented inverse problem solution. In the following two sections we are trying to solve the problem using these two ideas.

5.1. Preconditioning by a model covariance matrix

We will now use $\widetilde{\mathbf{g}}^{(n)} = \mathbf{M}\mathbf{g}^{(n)}$ instead of our old gradient $\mathbf{g}^{(n)}$, where $\mathbf{M}$ is the so-called model covariance matrix. This means that the new BFGS update formula will get the following form

$$\widetilde{\mathbf{G}}^{(n)} = \left(\mathbf{I} - \frac{\widetilde{\mathbf{y}}^{(n-1)}\mathbf{s}^{(n-1)T}}{\widetilde{\mathbf{y}}^{(n-1)T}\mathbf{s}^{(n-1)}}\right)^T \widetilde{\mathbf{G}}^{(n-1)} \left(\mathbf{I} - \frac{\widetilde{\mathbf{y}}^{(n-1)}\mathbf{s}^{(n-1)T}}{\widetilde{\mathbf{y}}^{(n-1)T}\mathbf{s}^{(n-1)}}\right) + \frac{\mathbf{s}^{(n-1)}\mathbf{s}^{(n-1)T}}{\widetilde{\mathbf{y}}^{(n-1)T}\mathbf{s}^{(n-1)}} \quad (5.5)$$

and

$$\widetilde{\mathbf{G}}^{(0)} = \mathbf{I}, \quad (5.6)$$

where $\widetilde{\mathbf{y}}^{(n-1)} = \mathbf{M}\mathbf{y}^{(n-1)}$. From equation 5.5 one can easily derive that the new matrix $\widetilde{\mathbf{G}}^{(n)}$ satisfies a new secant equation

$$\widetilde{\mathbf{G}}^{(n)}\widetilde{\mathbf{y}}^{(n-1)} = \mathbf{s}^{(n-1)}. \tag{5.7}$$

From equations 2.34 and 5.7 it follows that

$$\widetilde{\mathbf{G}}^{(n)} = \mathbf{G}^{(n)}\mathbf{M}^{-1} \tag{5.8}$$

This means that all the search directions remain exactly the same, except the very first one, in other words

$$\widetilde{\mathbf{p}}^{(n)} = \begin{cases} \mathbf{p}^{(n)}, & n > 0, \\ \mathbf{M}\mathbf{p}^{(n)}, & n = 0. \end{cases} \tag{5.9}$$

From equation 5.9 we get that the matrix $\mathbf{M}$ has to be positive definite in order to obtain always a descent search direction $\widetilde{\mathbf{p}}^{(n)}$. A similar argumentation can be applied to the L-BFGS update formula 2.37.

This means that our optimization method should still work if we multiply the gradient $\mathbf{g}^{(n)}$ by any positive definite matrix $\mathbf{M}$.

Now we are ready to move on to the solution of the problem. We apply the following Gaussian filter to the gradient $\mathbf{g}^{(n)}$,

$$\widetilde{g}_k^{(n)} = \sum_{i=1}^{N_x N_y N_z} f_{i,k} \cdot g_i^{(n)}, \tag{5.10}$$

where

$$f_{i,k} = \begin{cases} \dfrac{e^{-\frac{1}{2}\left[\left(\frac{x_i^c - x_k^c}{a_x dx}\right)^2 + \left(\frac{y_i^c - y_k^c}{a_y dy}\right)^2\right]}}{\sum\limits_{l=1}^{N_x N_y N_z} e^{-\frac{1}{2}\left[\left(\frac{x_l^c - x_k^c}{a_x dx}\right)^2 + \left(\frac{y_l^c - y_k^c}{a_y dy}\right)^2\right]}}, & i \in [N_x N_y(\gamma - 1) + 1, N_x N_y \gamma] \\ 0, & \text{else.} \end{cases} \tag{5.11}$$

This filtering could be alternatively viewed as applying our optimization method to minimize the old objective functional φ, but in a new model space of the new model parameters

$$\widetilde{\sigma}_k = \sum_{i=1}^{N_x N_y N_z} f_{i,k} \cdot \sigma_i. \tag{5.12}$$

In equation 5.11 γ corresponds to the number of the layer, where the cell with conductivity $\widetilde{\sigma}_k$ is located.

Figure 5.2 illustrates the effect of such a filter on the first update model, the first layer of which is shown in Figure 5.1. The conductivity values of the first update have the same behaviour as the gradient $\mathbf{g}^{(1)}$. From this figure we can see that the filter reduces the erratic behaviour for the upper layers and does not significantly change the already smooth lower layers of the model. We also see that higher values of the parameters a_x and a_y produce smoother images.
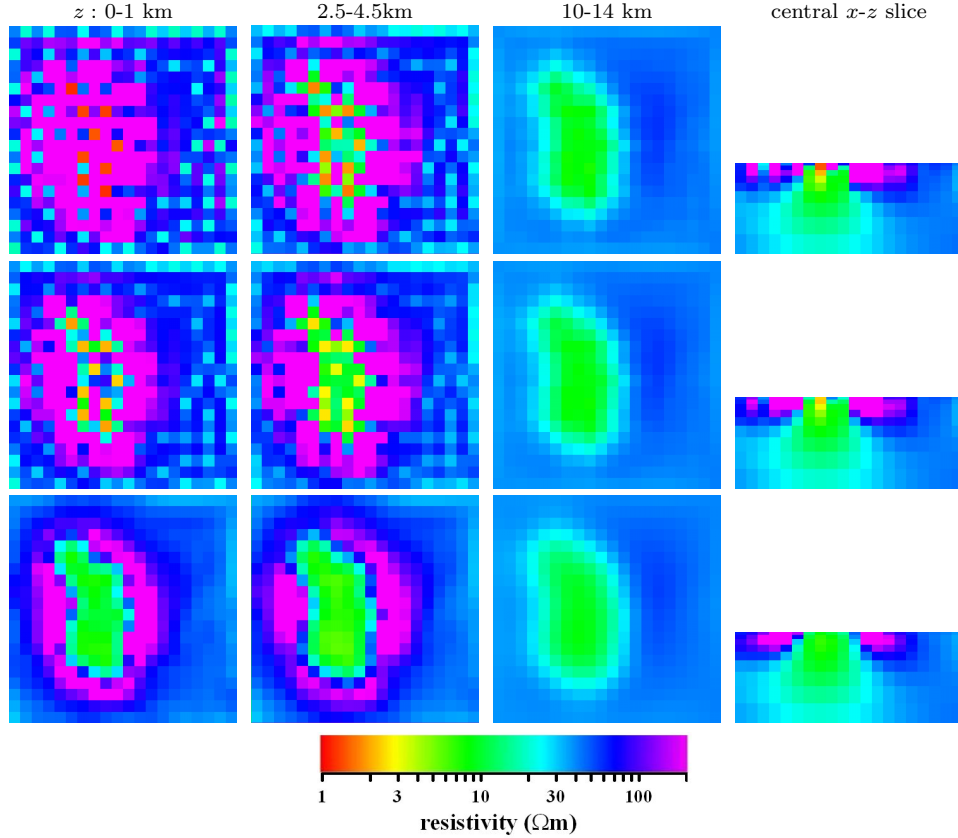
Figure 5.2.: The effect of the Gaussian filter described in equations 5.10, 5.11. The first 3 panels of each row show 3 horizontal $(x - y)$ slices through the model and the last panel shows the central $(x - z)$ cross-section through the middle of the model. The 1st row corresponds to the unfiltered model, the 2nd to the model after applying the filter with $a_x = a_y = 0.5$ and the last row with $a_x = a_y = 1$.

In our implementation $k = 1, \cdots, N_x N_y N_z$ and the model covariance matrix $\mathbf{M} = \{f_{i,k}\}$ is a square matrix. We apply this model covariance matrix $\mathbf{M}$, as a preconditioner, in order to overcome the problem, stated in the beginning of this

chapter. Applying such a preconditioner is similar to the idea of Siripunvaraporn *et al.* (2005).

We will check now how this idea helps in the example of two adjacent blocks, which was introduced in section 4.2.4. For the following experiment, we chose to use the two block model with 80 MT sites described in section 4.2.4.1. As before, the inversion domain coincides with the modelling domain and comprises of $20 \times 20 \times 9 = 3,600$ rectangular cells, extending to a depth of 32 km. Again we covered the surface ($z = 0$) of the inversion domain with 80 MT sites ($N_S = 80$). The coordinates of these MT sites are exactly the same as before (see Figure 4.38). For these MT sites we simulated data at 3 frequencies of 0.01, 0.0033 and 0.001 Hz ($N_T = 3$). We again added 1% noise to the simulated data.

For these data we compare results from two versions of our inverse problem solution, one without the filter ($\mathbf{g}^{(n)}$ used as the gradient), and another one with the filter ($\widetilde{\mathbf{g}}^{(n)}$ used as the gradient). Our initial guess conductivity was 50 Ωm for the whole inversion domain, assuming that the outside conductivity coincides with the true background for both of these solutions. For this initial model the true background is just a two-layered structure with a 10-km thick 10 Ωm layer on the top of the 100 Ωm halfspace.

For the inversion with the filter we now have two extra parameters a_x and a_y. Too large values of these filtering parameters deliver an overly smooth resistivity image, not allowing to get a sufficiently small data misfit φ_d. So in order to reach a satisfactory value of the data misfit we are using a sequence of decreasing filtering parameters a_x and a_y, similarly to the reduction of the regularization parameter λ. We first choose $a_x = a_y = 3$ and then gradually diminish the values of these parameters. With the first values we run first 10 iterations, then we change them to $a_x = a_y = 2$ for another 20 iterations, then to $a_x = a_y = 1$ for additional 20 iterations, and finally run the final 100 iterations without filter at all. We tried various values of the filtering parameters, but all of these experiments show that the exact values of a_x and a_y are not critical for the inversion results.

The comparison of the results of the inversions with and without filtering is shown in Figures 5.3, 5.4 and 5.5.

From these figures one can obviously see that the results with filtering are much more similar to the true model. The positions and the resistivity values of the anomalies are reasonably well matched. The location of the interface between conductor and resistor is found. With depth the image becomes more smooth and the
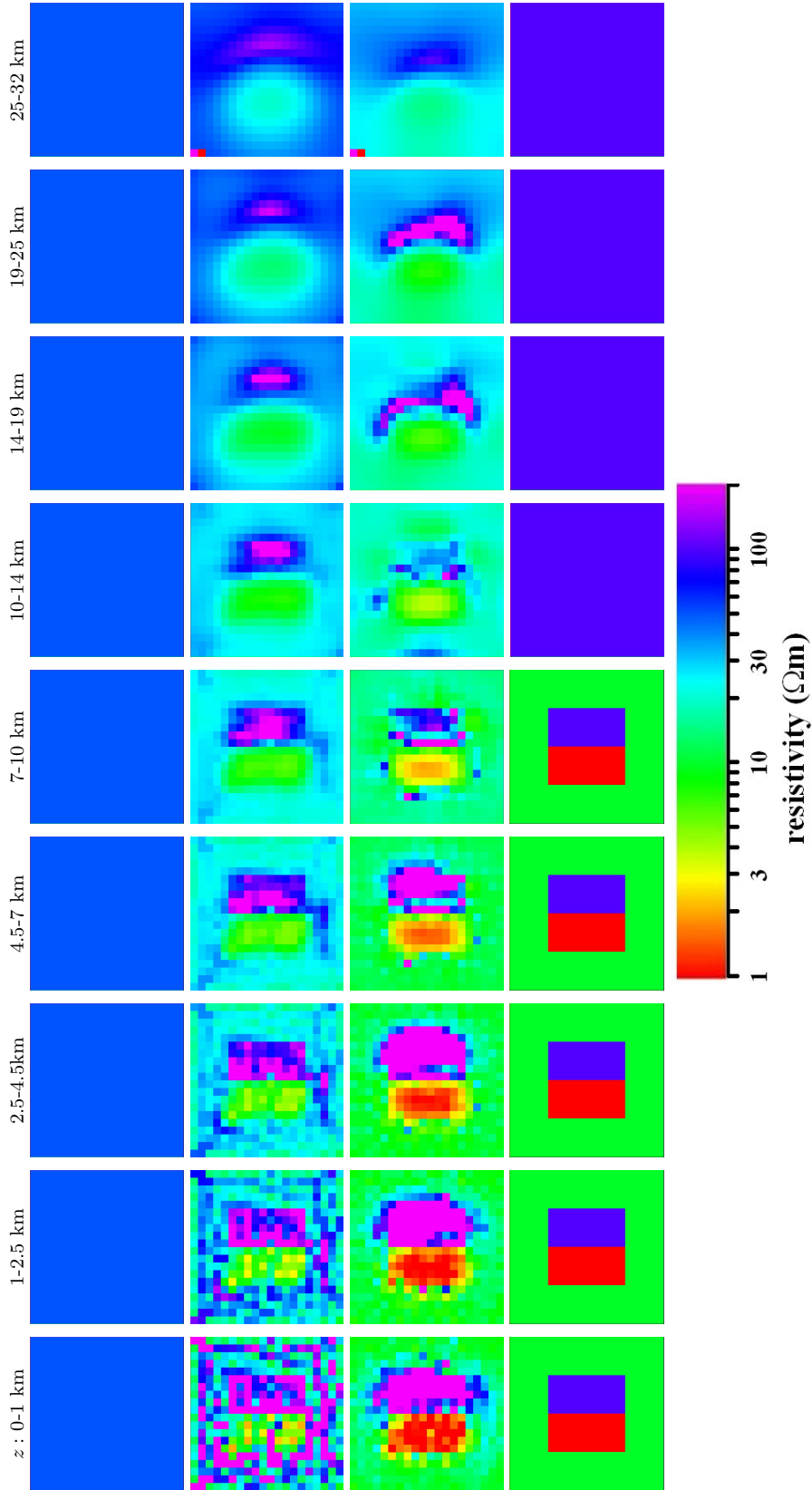
Figure 5.3.: Comparison of different inversion results. Each row presents nine horizontal $(x - y)$ slices through the model starting from the top (left) to the bottom (right). The 1st row corresponds to the initial guess model, the 2nd to the result of the inversion without filtering, the 3rd to the inversion with additional filtering described in equations 5.10, 5.11 and the last row is the true model. 80 MT sites and 3 frequencies were used.
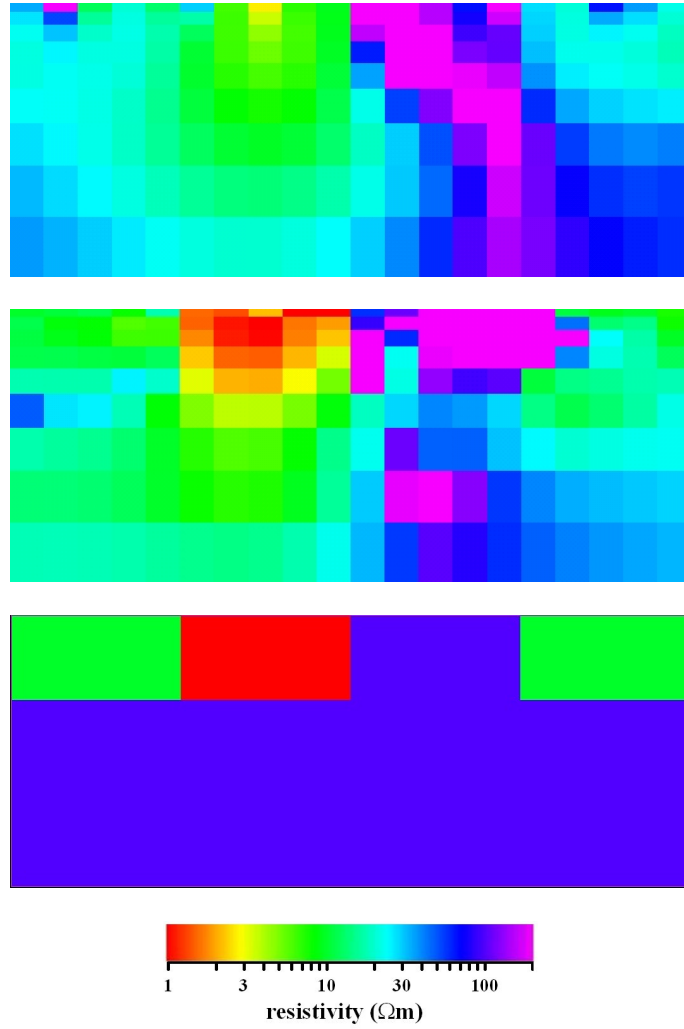
Figure 5.4.: Comparison for a central (x-z) cross-section. The upper panel presents cross-section through the inversion result without any filter, the 2nd - through the result with filtering described in equations 5.10, 5.11, and the lower panel presents cross-section through the true model. 80 MT sites and 3 frequencies were used.
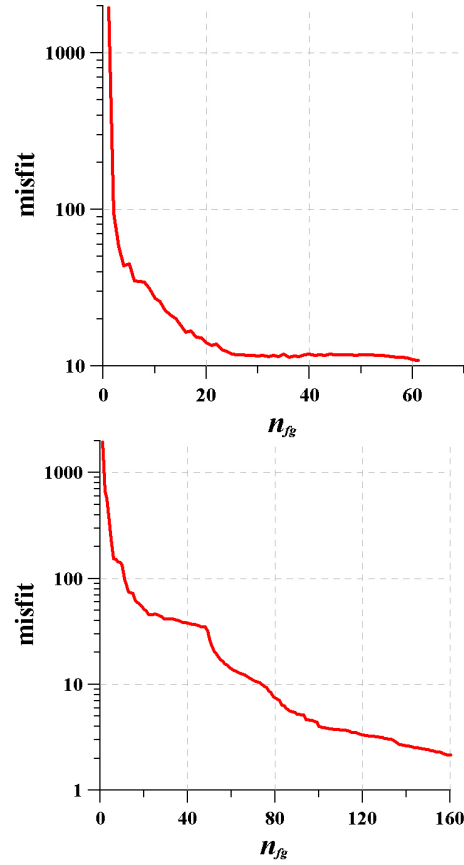
Figure 5.5.: Comparison of the convergence curves. The inversion without the filter (top) converged to a data misfit φ_d of 11, corresponding to an rms of 16.6% and with the filter (bottom) it drops to 2.5 ($rms = 8\%$). 80 MT sites and 3 frequencies were used.

conductor extends slightly deeper, but this can be expected for MT.

5.2. Preconditioning by the Hessian matrix

Another possibility is to smooth the gradient using the inverse of the Hessian matrix. This idea was proposed to us by Gregory Newman in a personal communication. Let us introduce the equations we need to implement this idea. As before

$$\widetilde{\mathbf{g}}^{(n)} = \mathbf{M}^{(n)}\mathbf{g}^{(n)}. \tag{5.13}$$

We use the preconditioner (Newman and Boggs, 2004; Mackie *et al.*, 2007)

$$\mathbf{M}^{(n)} = (\text{diag}(\widetilde{\mathbf{H}}^{(n)}) + \lambda\mathbf{W}^T\mathbf{W})^{-1}, \tag{5.14}$$

where $\mathbf{H}^{(n)}$ and $\mathbf{W}^T\mathbf{W}$ are the Hessian matrices of the data misfit φ_d and stabilizer φ_s, respectively, and λ as before is the regularization parameter. The tilde sign stands here for approximation. The matrix $\mathbf{W}$ in our implementation represents a finite-difference approximation to the Laplace operator (see Sections 2.3 and 4.1.2).

The essential difficulty here is the calculation of those diagonal elements

$$H_{kk} = \frac{\partial^2 \varphi_d}{\partial m_k \partial m_k} = \frac{\partial^2 \varphi_d}{\partial \sigma_k \partial \sigma_k}(\sigma_k^{(0)})^2. \tag{5.15}$$

5.2.1. Calculation of second derivatives $\frac{\partial^2 \varphi_d}{\partial \sigma_k \partial \sigma_k}$

As we showed earlier in Section 4.1.1

$$\frac{\partial \varphi_d}{\partial \sigma_k} = \Re\left\{\sum_{i=1}^{N_S}\sum_{j=1}^{N_T}\beta_{ij}tr\left[\overline{\mathbf{A}}_{ij}^T\frac{\partial \mathbf{Z}_{ij}}{\partial \sigma_k}\right]\right\}, \tag{5.16}$$

From this equation and neglecting the second-order terms one can get the following

$$\frac{\partial^2 \varphi_d}{\partial \sigma_k \partial \sigma_k} = \Re\left\{\sum_{i=1}^{N_S}\sum_{j=1}^{N_T}\beta_{ij}tr\left[\frac{\partial \overline{\mathbf{Z}}_{ij}^T}{\partial \sigma_k}\frac{\partial \mathbf{Z}_{ij}}{\partial \sigma_k}\right]\right\}, \tag{5.17}$$

Recalling (see 4.12 and 4.15) that

$$\frac{\partial \mathbf{Z}_{ij}}{\partial \sigma_k} = (\mathbf{pe}_{jk}(\mathbf{r}_i) - \mathbf{Z}_{ij}\mathbf{ph}_{jk}(\mathbf{r}_i))\mathbf{H}_{ij}^{-1}, \tag{5.18}$$

we obtain the equations

$$\frac{\partial \mathbf{Z}_{ij}}{\partial \sigma_k} = \mathbf{p}(\mathbf{e}_{jk}(\mathbf{r}_i) - \mathbf{p}^T \mathbf{Z}_{ij}\mathbf{p}\mathbf{h}_{jk}(\mathbf{r}_i))\mathbf{H}_{ij}^{-1}, \tag{5.19a}$$

$$\frac{\partial \overline{\mathbf{Z}}_{ij}^T}{\partial \sigma_k} = \overline{\mathbf{H}}_{ij}^{-T}(\overline{\mathbf{e}}_{jk}^T(\mathbf{r}_i)\mathbf{p}^T - \overline{\mathbf{h}}_{jk}^T(\mathbf{r}_i)\mathbf{p}^T\overline{\mathbf{Z}}_{ij}^T). \tag{5.19b}$$

Very similar to the calculation of the gradient in Section 4.1.1 let us write the following equations

$$\nabla \times \nabla \times \mathbf{e}_{jk} - \sqrt{-1}\omega_j\mu\sigma(\mathbf{r})\mathbf{e}_{jk} = \sqrt{-1}\omega_j\mu\chi_k\mathbf{E}_j, \tag{5.20a}$$

$$\nabla \times \nabla \times \mathbf{u}_{ij} - \sqrt{-1}\omega_j\mu\sigma(\mathbf{r})\mathbf{u}_{ij} = \sqrt{-1}\omega_j\mu(\mathbf{j}_{ij}^{ext} + \nabla \times \mathbf{h}_{ij}^{ext}), \tag{5.20b}$$

where

$$\mathbf{j}_{ij}^{ext} = \mathbf{p}^T\delta(\mathbf{r} - \mathbf{r}_i), \tag{5.21}$$

and

$$\mathbf{h}_{ij}^{ext} = -\frac{1}{\sqrt{-1}\omega_j\mu}\mathbf{p}^T\mathbf{Z}_{ij}^T\mathbf{p}\mathbf{j}_{ij}^{ext}. \tag{5.22}$$

It is important to note that, in contrast to equation 4.21b, equation 5.20b is now different for different MT sites (index i). Multiplying equation 5.20a by $\mathbf{u}_{ij}^T$ and equation 5.20b by $\mathbf{e}_{jk}^T$ and integrating the difference of the resulting equations over the whole 3D space, one gets

$$\int_{R^3}\left[\mathbf{e}_{jk}^T\mathbf{j}_{ij}^{ext} + \mathbf{e}_{jk}^T\nabla \times \mathbf{h}_{ij}^{ext}\right]dV = \int_{V_k}\left[\mathbf{u}_{ij}^T\mathbf{E}_j\right]dV. \tag{5.23}$$

However

$$\int_{R^3}\mathbf{e}_{jk}^T\nabla \times \mathbf{h}_{ij}^{ext}dV = \int_{R^3}\nabla \times \mathbf{e}_{jk}^T\mathbf{h}_{ij}^{ext}dV = \int_{R^3}\sqrt{-1}\omega_j\mu\mathbf{h}_{jk}^T\mathbf{h}_{ij}^{ext}dV, \tag{5.24}$$

and hence,

$$\int_{V_k}\left[\mathbf{u}_{ij}^T\mathbf{E}_j\right]dV = \int_{R^3}(\mathbf{e}_{jk}^T - \mathbf{h}_{jk}^T\mathbf{p}^T\mathbf{Z}_{ij}^T\mathbf{p})\mathbf{p}^T\delta(\mathbf{r} - \mathbf{r}_i)dV. \tag{5.25}$$

From the equations 5.19 and 5.25

$$\frac{\partial \mathbf{Z}_{ij}}{\partial \sigma_k} = \int_{V_k}\left[\mathbf{u}_{ij}^T\mathbf{E}_j\right]dV\mathbf{H}_{ij}^{-1}. \tag{5.26}$$

Now we are finally ready to write the equation for the second derivatives of the data misfit φ_d

$$\frac{\partial^2 \varphi_d}{\partial \sigma_k \partial \sigma_k} = \Re \left\{ \sum_{i=1}^{N_S} \sum_{j=1}^{N_T} \beta_{ij} tr \left[\overline{\mathbf{H}}_{ij}^{-T} \int_{V_k} \left[\overline{\mathbf{E}}_j^T \overline{\mathbf{u}}_{ij} \right] dV \int_{V_k} \left[\mathbf{u}_{ij}^T \mathbf{E}_j \right] dV \mathbf{H}_{ij}^{-1} \right] \right\}. \quad (5.27)$$

The formula of equation 5.27 means that the computational load for calculating the second derivatives is equivalent to the solution of $2 \times N_T$ forward problems using standard Maxwell's equations to find $\mathbf{E}_j$ and of $2 \times N_T \times N_S$ adjoint problems using equations 5.20b to find $\mathbf{u}_{ij}$ for all periods $j = 1, ..., N_T$ and for all MT sites $i = 1, ..., N_S$.

In order to reduce the time for caculation of $\mathbf{u}_{ij}$, we calculate these fields for the 1D background model. We perform these calculation just once before the inversion. So instead of the true Hessian matrix, $\mathbf{H}$, we use $\widetilde{\mathbf{H}}$ with the following diagonal elements

$$\widetilde{H}_{kk} = \Re \left\{ \sum_{i=1}^{N_S} \sum_{j=1}^{N_T} \beta_{ij} tr \left[\overline{\mathbf{H}}_{ij}^{-T} \int_{V_k} \left[\overline{\mathbf{E}}_j^T \overline{\mathbf{u}}_{ij}^{1D} \right] dV \int_{V_k} \left[\mathbf{u}_{ij}^{1D^T} \mathbf{E}_j \right] dV \mathbf{H}_{ij}^{-1} \right] \right\} (\sigma_k^{(0)})^2. \quad (5.28)$$

We implemented the theory described in this section and then undertook a number of the synthetic experiments, but so far did not obtain any satisfactory results. It is difficult immediately see whether it is some numerical problem of our implementation or some problem with the approach. This investigation is subject of our ongoing research.

Chapter 6.

Conclusions

3D MT inversion is very large in scale and only a few years ago it seemed to be impossible due to the limited speed and memory of computers. The only way to interpret 3D MT datasets was to use 3D forward modelling codes in order to fit the data through trial and error. In the 3D case this procedure is somewhat cumbersome, tedious, and requires a lot of imagination. That is why 2D approximations were usually used. Trial and error techniques are sometimes used in 2D, however there are also a number of preferable 2D inversion schemes available. To use 2D forward modelling and inversion is a very common practice for interpreting 3D datasets. In some cases this can be done successfully, however in some instances, especially in areas of very complex 3D geology, it can lead to wrong interpretation. Today because of high level of modern computer facilities the numerical solution of 3D inverse problem becomes possible, however it still remains a very difficult and computationally expensive task. Therefore to date there are only a few 3D MT inversion codes available, most of which are not free. Recently, Siripunvaraporn *et al.* (2005) released their code WSINV3DMT and now, judging by the WSINV3DMT[1] webpage, it attracts a large amount of users. This demonstrates the urgent need for 3D MT inversion.

For this thesis we developed and implemented a 3D magnetotelluric inversion method. This method is based on the limited memory quasi-Newton optimization approach. The main advantage of this approach, compared to other Newton-type optimization techniques, is the storage requirement, only a limited number of pairs of vectors have to be stored in memory. This advantage makes it possible to handle large-scale problems, such as 3D MT inversion. As for most other types of optimization methods, the limited memory QN optimization requires the calculation

---

[1]http://mucc.mahidol.ac.th/∼scwsp/wsinv3dmt

of the gradient of the penalty function φ. Using the adjoint method helps to perform this task with a minimum number of forward modellings and we developed and presented the concrete formulae for the gradients in the 1D and 3D MT cases, respectively. The mathematics behind the derivation of these formulae and their numerical implementation are not straightforward. Therefore we assured the accuracy of the implementation by comparing our numerical results with an analytical solution and observe good agreement for the adjoint fields needed for the gradient. Our development is quite general and is not limited to magnetotellurics alone. It can be applied to a variety of EM problems, such as marine controlled-source EM and well induction logging.

Another important part of the inversion is the forward modelling code employed as an engine for the inversion. Most of the existing 3D inversions use finite-difference and finite-element forward modelling codes. We use the integral equation (IE) code *x3d*. To accelerate the forward modelling code, we parallelize its discrete 2D convolution routine, which is the most time-consuming part of the serial solution. The comparison between the serial and parallel versions on both, distributed-memory and shared-memory clusters, shows that we achieve a reasonable acceleration, e.g. a factor of 7 for 16 processors and large models. Another inversion based on IE approach is developed by Zhdanov and Golubev (2003). To speed up the inversion process it uses approximate forward modelling solution, but general reliability and the accuracy of such a solution is still under question. Zhdanov and Tolstaya (2004), to insure the accuracy of the solution, used rigorous forward modelling at the final stage of the inversion.

Due to the fact that the solution of the 3D MT inverse problem is non unique, we need an appropriate regularization approach. We suggest two Tikhonov-type regularizations: strong regularization, which uses the Neumann boundary conditions and ties the resistivity in the inversion domain to the fixed background resistivity, and weak regularization, which only assumes continuity of the gradient at the boundary of the inversion domain. With strong regularization the inversion tends to extend the background resistivity inside the inversion domain. While this helps in synthetic tests cases where the true background resistivity is known, it is impractical for the inversion of real data, as the background resistivity has to be chosen before the inversion process and exerts an overly strong influence on the inversion results. In comparison, the weak regularization keeps the influence of the background resistivity to a minimum and is appropriate for situations where the background resistivity

is not known a priori.

Our tests with a suite of standard synthetic test models (Wannamaker, 1991; Mackie *et al.*, 1994; Avdeev *et al.*, 1997; Zhdanov and Tolstaya, 2004; Siripunvaraporn *et al.*, 2005, among others) demonstrate that with pure Tikhonov-type regularization we only achieve satisfactory results with a dense site coverage. Generally speaking though, we are satisfied by the software developed and by the results of our model experiments. For the conductive dyke model, for example, we can reasonably recover the true resistivity image for both buried and outcropped dykes; and for both coarse and dense MT site coverage. Therefore we believe in the robustness and accuracy of the inversion results obtained for the dyke models.

For the more complicated model, the model with two adjacent blocks, our feelings are controversial. On the one hand side we achieve relatively good results with a dense MT sites coverage. At the same time, for a coarser coverage we found that our inversion solution cannot "see" through numerical cells that are not covered by MT sites. This conclusion promptly implies that Tikhonov-type regularization, which we included in our inversion solution, is not powerful enough to suppress the non-smoothness of the resistivity image, especially for the upper part of the model.

However, we believe that our solution can be used to recover the true resistivity of the lower parts of earth models. As for the upper part of the models its proper recovery depends on many factors, such as the geometry and resistivity of the structures inside the Earth, coverage of the region by MT sites and many others. In order to construct reliable resistivity images one has to put more strong constraints on the model parameters, stronger than those imposed by traditional Tikhonov-type regularization.

We suggest to use different types of the preconditioners in our inversion to overcome this problem. The first one is based on applying a model covariance matrix to smooth the gradient of the penalty functional. This is similar to the idea of Siripunvaraporn *et al.* (2005). In our implementation the model covariance matrix is based on a Gaussian filter. Applying such a preconditioner improves the results dramatically, although some artifacts are still present. A possible explanation is that our filter is too simple and a more complicated filter has to be applied. The second preconditioner is based on the approximation to the inverse of the Hessian matrix. This approach was proposed by Gregory Newman. The mathematics behind this approach is not as trivial as for the first one. We developed and implemented this approach, but so far did not obtain satisfactory results. At the moment we are

trying to understand whether this is because of some numerical error in our current implementation of the approach or due to some problem with this approach itself. This is a subject of ongoing research.

It is difficult to compare different 3D MT inversion codes due to the different forms of the data misfit used, different forward engines employed, the optimization approaches, stopping criteria and so on. Some codes require less memory, but converge slower. Another issue is that different codes can perform better in different situations and that the quantification of the overall quality is difficult. We only can compare the results of the inversion for particular synthetic datasets. One of such an attempts was the MT 3D inversion workshop held by DIAS in March 2008 (see MT3DINV[2] webpage). There the data computed from some secret synthetic model was distributed among 3D MT software developers and the various codes showed more or less similar results, however the time for calculation and memory requirements were not compared. In addition other factors such as noise and incomplete data were not taken into consideration and such issues can be the dominating factors for the quality of an inversion of real data.

For the future a closer examination of the implemented preconditioners and the investigation of possible alternatives would show in how far the efficiency of our approach can be improved. One possibility would be to relax the influence of the gaussian filter for deeper layers where it is not needed. However, it seems that the filter does not affect these layers even in the current version and thus the behaviour should not change fundamentally.

One more promising extension is the application of the automatic relaxation scheme to the regularization in 3D case and possibly to the Gaussian preconditioner. So far we adjust the value of the regularization parameter λ at different stages of the inversion manually based on our experience. This is time consuming as the inversion has to be stopped, the convergence examined manually and restarted with the new value. An automatic scheme would accelerate this process, even though human experience and judgment can never fully be replaced.

Even though the first paper on 3D MT inversion was published over 15 years ago Mackie and Madden (1993), the field is still in its infancy and 3D inversion codes only now become available for a wider range of researchers. With more widespread use the advantages and deficiencies of individual approaches will become more apparent

---

[2]MT 3D Inversion Workshop, DIAS, March, 2008,
  http://www.dias.ie/lang/en/cosmic/geo/mt_workshop2008.html

and give the developers the opportunity to improve their codes. Even though 2D inversion approaches will remain in use for their cost effectiveness and comparative ease of use, 3D inversion will become the standard method for constructing detailed models of the Earth.

Appendix A.

MT impedance

In this appendix we introduce the basic ideas and equations of the magnetotelluric method. The MT method was proposed independently by Tikhonov (1950) and Cagniard (1953) as a method for a one-dimensional sounding of the Earth. They proposed to use an impedance $\mathbf{Z}$ to find the Earth's conductivity. Below we derive the explicit expressions for the impedance for the 1D case.

A.1. Impedance of a layered Earth

Let us consider an $N-$layered Earth model with conductivities σ_k, $(k = 1, ..., N)$ within each layer. Within each layer the Helmholtz equation

$$\Delta \mathbf{E} = -i\omega\mu_0\sigma\mathbf{E} \tag{A.1}$$

holds. Choosing the coordinate system so that the external current $\mathbf{j}^{ext}$ flows in $x-$direction and with the $z-$axis pointing downward, the $x-$component of the electric field inside the k-th layer, $z \in (z_k, z_{k+1})$, have the following form

$$E_{xk} = E_{1k}e^{\kappa_k z} + E_{2k}e^{-\kappa_k z}, \tag{A.2}$$

where $\kappa_k = \sqrt{-i\omega\mu_0\sigma_k}$. Now we can compute the following impedance transfer function of the k-th layer

$$\begin{aligned} Z_k &= \frac{E_{xk}}{H_{yk}} = \frac{i\omega\mu_0 E_{xk}}{\partial_z E_{xk}} \tag{A.3} \\ &= \frac{i\omega\mu_0}{\kappa_k}\frac{E_{1k}e^{\kappa_k z} + E_{2k}e^{-\kappa_k z}}{E_{1k}e^{\kappa_k z} - E_{2k}e^{-\kappa_k z}} = \frac{i\omega\mu_0}{\kappa_k}\frac{\left(1 + A_k e^{-2\kappa_k z}\right)}{\left(1 - A_k e^{-2\kappa_k z}\right)}, \tag{A.4} \end{aligned}$$

where formula A.3 is obtained using the Faraday's law $\nabla \times \mathbf{E} = i\omega\mu_0\mathbf{H}$ and the coefficient $A_k = E_{2k}/E_{1k}$.

We now can derive the transfer functions $Z_k(z_k)$ and $Z_k(z_{k+1})$ at the top and bottom of the k-th layer, respectively:

$$Z_k(z_k) = \frac{i\omega\mu_0}{\kappa_k} \frac{\left(1 + A_k e^{-2\kappa_k z_k}\right)}{\left(1 - A_k e^{-2\kappa_k z_k}\right)}, \tag{A.5a}$$

$$Z_k(z_{k+1}) = \frac{i\omega\mu_0}{\kappa_k} \frac{\left(1 + A_k e^{-2\kappa_k z_{k+1}}\right)}{\left(1 - A_k e^{-2\kappa_k z_{k+1}}\right)}. \tag{A.5b}$$

From equation A.5b we can derive the coefficient A_k as follows

$$A_k = e^{2\kappa_k z_{k+1}} \frac{\frac{\kappa_k}{i\omega\mu_0} Z_k(z_{k+1}) - 1}{\frac{\kappa_k}{i\omega\mu_0} Z_k(z_{k+1}) + 1}, \tag{A.6}$$

Now we substitute formula A.6 into equation A.5a to yield:

$$Z_k(z_k) = \frac{i\omega\mu_0}{\kappa_k} \left[\frac{-\sinh(\kappa_k\Delta_k) + \cosh(\kappa_k\Delta_k)\frac{\kappa_k}{i\omega\mu_0} Z_k(z_{k+1})}{\cosh(\kappa_k\Delta_k) - \sinh(\kappa_k\Delta_k)\frac{\kappa_k}{i\omega\mu_0} Z_k(z_{k+1})} \right]. \tag{A.7}$$

In this equation Δ_k stands for $z_{k+1} - z_k$.

Furthermore, the components of the electric and magnetic fields are continuous at the transition from the k-th to the $(k + 1)$-th layer, and therefore

$$Z_k(z_{k+1}) = Z_{k+1}(z_{k+1}). \tag{A.8}$$

From equation A.8 and equation A.7 we can obtain the following recursive formula for the impedance transfer function:

$$Z_k(z_k) = \frac{i\omega\mu_0}{\kappa_k} \left[\frac{-\sinh(\kappa_k\Delta_k) + \cosh(\kappa_k\Delta_k)\frac{\kappa_k}{i\omega\mu_0} Z_{k+1}(z_{k+1})}{\cosh(\kappa_k\Delta_k) - \sinh(\kappa_k\Delta_k)\frac{\kappa_k}{i\omega\mu_0} Z_{k+1}(z_{k+1})} \right]. \tag{A.9}$$

To find the impedance $Z_1(z_1)$ at the surface of the Earth one should use the fact, that the impedance $Z_N(z_N) = i\omega\mu_0/\kappa_N$ (impedance of a half-space), and apply the recursive formula A.9 iteratively, moving from the top of the lowermost layer to the surface.

A.2. Impedance of 3D Earth

To obtain the impedance tensor in the 3D case one also has to solve a system of Maxwell's equations

$$\nabla \times \mathbf{H} = (\sigma - i\omega\varepsilon)\mathbf{E} + \mathbf{j}^{ext}, \tag{A.10a}$$

$$\nabla \times \mathbf{E} = i\omega\mu(\mathbf{H} + \mathbf{h}^{ext}), \tag{A.10b}$$

but now the fields and the conductivity depend on the Cartesian coordinates (x, y, z).

When we numerically solve the system of Maxwell's equations, in other words find the electric, $\mathbf{E}$, and magnetic, $\mathbf{H}$, fields we can obtain the complex-valued impedance tensor, $\mathbf{Z}$. This tensor relates the orthogonal components of the horizontal electric and magnetic fields as

$$\begin{pmatrix} E_x \\ E_y \end{pmatrix} = \begin{pmatrix} Z_{xx} & Z_{xy} \\ Z_{yx} & Z_{yy} \end{pmatrix} \begin{pmatrix} H_x \\ H_y \end{pmatrix}. \tag{A.11}$$

Appendix B.

Calculation of Digital Convolution

This appendix is the summary of the Appendix C of paper Avdeev *et al.* (1997). To simplify the following explanation instead of a 2D digital convolution we assume a 1D digital convolution

$$h_k = \sum_{k'=1}^{N} g_{k-k'} f_{k'}, k = 1, \cdots, N \tag{B.1}$$

In this equation, the function f_k is defined for $k = 1, \cdots, N$, while the function g_k is defined for $k = 0, \pm 1, \cdots \pm (N-1)$.

If we define the new functions $\widetilde{f}_k$ and $\widetilde{g}_k$ as following

$$\widetilde{f}_l = \begin{cases} f_l, & l = 1, \cdots, N \\ 0, & l = N+1, \cdots, 2N \end{cases} \tag{B.2}$$

$$\widetilde{g}_k = \begin{cases} g_{l-1}, & l = 1, \cdots, N \\ 0, & l = N+1 \\ g_{l-1-2N}, & l = N, \cdots, 2N, \end{cases} \tag{B.3}$$

then the convolution B.1 can be written as

$$h_k = \Phi^{-1} \left[\Phi[\widetilde{g}]\Phi[\widetilde{f}] \right]_k, k = 1, \cdots, N, \tag{B.4}$$

where Φ and Φ^{-1} are direct and inverse Digital Fourier Transforms, respectively and are defined as

$$\Phi[S]_k = \sum_{l=1}^{2N} S_l e^{2\pi i \frac{(l-1)(k-1)}{2N}} \tag{B.5}$$

$$\Phi^{-1}[S]_k = \frac{1}{2N} \sum_{l=1}^{2N} S_l e^{-2\pi i \frac{(l-1)(k-1)}{2N}} \tag{B.6}$$

Appendix C.

How to measure the 3D misfit?

The predicted $\mathbf{Z}$ and observed $\mathbf{D}$ impedances (at a given MT site and at a discrete period) are 2×2 matrices, not scalars. So, the question is how to measure the distance $\rho(\mathbf{Z}, \mathbf{D})$ between them in order to define a proper form of misfit φ_d. The answer is not obvious. A natural way to define such a distance is to consider the matrix $\mathbf{A} = \mathbf{Z} - \mathbf{D}$ and its induced matrix norm

$$\|\mathbf{A}\|_2 = \max \frac{\|\mathbf{A}\mathbf{u}\|_2}{\|\mathbf{u}\|_2} \tag{C.1}$$

where $\|\mathbf{u}\|_2 = \sqrt{|u_1|^2 + |u_2|^2}$, for any vector $\mathbf{u} = (u_1, u_2)^T$, and define $\rho(\mathbf{Z}, \mathbf{D}) = \|\mathbf{Z} - \mathbf{D}\|_2$. It can be shown that for any matrix $\mathbf{A}$,

$$\|\mathbf{A}\|_2 = \sqrt{\lambda_1(\overline{\mathbf{A}}^T \mathbf{A})} \tag{C.2}$$

where $\lambda_1(\overline{\mathbf{A}}^T \mathbf{A})$ is the largest (real) eigenvalue of the Hermitian matrix $\overline{\mathbf{A}}^T \mathbf{A}$. Moreover, for a 2×2 matrix $\mathbf{A}$, it follows that

$$(\|\mathbf{A}\|_2)^2 = \frac{1}{2} \left(tr[\overline{\mathbf{A}}^T \mathbf{A}] + \sqrt{tr[\overline{\mathbf{A}}^T \mathbf{A}]^2 - 4\det[\overline{\mathbf{A}}^T \mathbf{A}]} \right), \tag{C.3}$$

where

$$tr[\overline{\mathbf{A}}^T \mathbf{A}] = |A_{xx}|^2 + |A_{xy}|^2 + |A_{yx}|^2 + |A_{yy}|^2 \tag{C.4}$$

and $\det[\overline{\mathbf{A}}^T \mathbf{A}]$ are respectively the trace and determinant of matrix $\overline{\mathbf{A}}^T \mathbf{A}$. Theoretically, the formula given in equation C.3 is what we are looking for. But, it is too complicated, i.e. not quadratic, to be considered an appropriate form of misfit

function. Somehow, we have to simplify it. From equation C.3 it follows that

$$\frac{1}{2}tr[\overline{\mathbf{A}}^T\mathbf{A}] \leq (\|\mathbf{A}\|_2)^2 \leq tr[\overline{\mathbf{A}}^T\mathbf{A}]. \tag{C.5}$$

The inequalities given in equation C.5 means that the distance $\rho(\mathbf{Z}, \mathbf{D}) = \|\mathbf{Z} - \mathbf{D}\|_2$ is controlled by the trace $tr[\overline{\mathbf{A}}^T\mathbf{A}]$, where $\mathbf{A} = \mathbf{Z} - \mathbf{D}$, and so this trace can be chosen to measure the misfit as

$$\varphi_d = \frac{1}{2}tr[\overline{\mathbf{A}}^T\mathbf{A}]. \tag{C.6}$$

Although it should be mentioned that $tr[\overline{\mathbf{A}}^T\mathbf{A}]$ is not associated with any matrix norm itself.

Appendix D.

More general 3D misfit and its derivative

Equation 4.2 is written for a particular problem where the data misfit φ_d includes the impedance difference matrices $\mathbf{A}_{ij}$ whose entries are equally weighted by the values $\sqrt{\beta_{ij}}$. The generalization of the theory presented in Chapter 4 for the case of the individually weighted entries of $\mathbf{A}_{ij}$ is not straightforward. The main difficulty here is in deriving equations for the derivatives $\frac{\partial \varphi_d}{\partial \sigma_k}$. However, it is still possible to straightforwardly extend the theory to the more general case, if the data misfit

$$\varphi_d = \frac{1}{2} \sum_{i=1}^{N_S} \sum_{j=1}^{N_T} \beta_{ij} tr[\overline{\widetilde{\mathbf{A}}}_{ij}^T \widetilde{\mathbf{A}}_{ij}], \tag{D.1}$$

is written in terms of the weighted matrices

$$\widetilde{\mathbf{A}}_{ij} = \begin{pmatrix} w_{xx} A_{xx} & w_{xy} A_{xy} \\ w_{yx} A_{yx} & w_{yy} A_{yy} \end{pmatrix}_{ij}, \tag{D.2}$$

where the tilde sign means the weighting by the real-valued weights, $w_{xx}, w_{xy}, w_{yx}, w_{yy}$. If we additionally assume that $w_{xy} = w_{yx}$, then it is easy to prove that $\widetilde{\mathbf{B}}^T = \widetilde{\mathbf{B}^T}$ and $tr[\widetilde{\mathbf{B}}\mathbf{C}] = tr[\mathbf{B}\widetilde{\mathbf{C}}]$ for any matrices $\mathbf{B}$ and $\mathbf{C}$. These simple properties allow us to obtain the relevant alterations of equations, presented in Section 4.1.1 of Chapter 4. It can be shown that equations 4.7, 4.14, 4.19, 4.20, 4.24 should be, respectively, altered to the following forms

$$\frac{\partial \varphi_d}{\partial \sigma_k} = \Re \left\{ \sum_{i=1}^{N_S} \sum_{j=1}^{N_T} tr \left[\overline{\widetilde{\mathbf{A}}}_{ij}^T \frac{\partial \widetilde{\mathbf{Z}}_{ij}}{\partial \sigma_k} \right] \right\}, \tag{D.3}$$

$$\frac{\partial \varphi_d}{\partial \sigma_k} = \Re \left\{ \sum_{i=1}^{N_S} \sum_{j=1}^{N_T} tr \left[\overline{\widetilde{\widetilde{\mathbf{A}}}}_{ji}^T \left(\mathbf{E}_{ij,k} - \mathbf{Z}_{ij} \mathbf{H}_{ij,k} \right) \mathbf{H}_{ij}^{-1} \right] \right\}, \tag{D.4}$$

$$\mathbf{j}_j^{ext} = \sum_{i=1}^{N_S} \mathbf{p}^T \overline{\widetilde{\widetilde{\mathbf{A}}}}_{ij} \mathbf{H}_{ij}^{-T} \delta(\mathbf{r} - \mathbf{r}_i), \tag{D.5}$$

$$\mathbf{h}_j^{ext} = -\frac{1}{\sqrt{-1}\omega_j \mu} \sum_{i=1}^{N_S} \mathbf{p}^T \mathbf{Z}_{ij}^T \overline{\widetilde{\widetilde{\mathbf{A}}}}_{ij} \mathbf{H}_{ij}^{-T} \delta(\mathbf{r} - \mathbf{r}_i), \tag{D.6}$$

$$\sum_{i=1}^{N_S} tr \left[\overline{\widetilde{\widetilde{\mathbf{A}}}}_{ij}^T \left(\mathbf{pe}_{jk}(\mathbf{r}_i) - \mathbf{Z}_{ij} \mathbf{ph}_{jk}(\mathbf{r}_i) \right) \mathbf{H}_{ij}^{-1} \right] = \int_{V_k} tr \left[\mathbf{u}_j^T \mathbf{E}_j \right] dV, \tag{D.7}$$

where

$$\widetilde{\widetilde{\mathbf{A}}}_{ij} = \begin{pmatrix} w_{xx}^2 A_{xx} & w_{xy}^2 A_{xy} \\ w_{yx}^2 A_{yx} & w_{yy}^2 A_{yy} \end{pmatrix}_{ij}. \tag{D.8}$$

All the other equations presented in Chapter 4 remains the same, including the key formula of equation 4.25.

Appendix E.

Hydrocarbon reservoir detectability study

In this appendix we present a comparative study about the detectability of a hydrocarbon reservoir in a marine environment, using controlled-source electromagnetic (CSEM) methods both in the time and frequency domain. This work was performed during a two-month visit to the Lawrence Berkeley National Laboratory and the results are published in Avdeeva *et al.* (2007). The target is a thin resistive body buried at a certain depth under the sea floor. The depth of the sea, and depth, thickness and resistivity of the reservoir are variable model parameters. For different sets of these parameters we calculate synthetic electromagnetic (EM) responses using a parallel version of the three-dimensional (3D) time-domain finite-difference forward modelling code by Commer and Newman (2004) and the 3D frequency-domain finite-difference code by Newman and Alumbaugh (1995). To compare the responses quantitatively, signal-to-noise ratios (SNR) were calculated as a function of time/frequency and source-receiver separation. SNR were calculated using the scattered field response of the reservoir as signal and the response of the background, in our case a two-layered model, as noise.

Marine CSEM is a promising yet challenging method in modern geophysical exploration for hydrocarbon reservoirs (MacGregor and Sinha, 2000; Eidesmo *et al.*, 2002; Ellingsrud *et al.*, 2002; Johansen *et al.*, 2005, among others). It is important as a supplementary method to seismic surveys. Recent works on modelling and inversion of marine CSEM data include (Um and Alumbaugh, 2005; Abubakar *et al.*, 2006; Constable and Weiss, 2006; Hoversten *et al.*, 2006, among others).

In contrast to time-domain electromagnetic (TDEM) methods and its corresponding data interpretation tools, the development and application of frequency-domain

(FDEM) methods for marine surveys has made significant progress. In this appendix we investigate the detectability of a 3D hydrocarbon reservoir in a marine environment. The first section presents synthetic responses obtained for different 3D hydrocarbon reservoir models with a time-domain and a frequency-domain finite-difference (FD) forward modelling solutions. Further, the two solutions are compared in their ability to detect a deep hydrocarbon reservoir.

E.1. Numerical examples

In this study a typical 3D hydrocarbon reservoir model, shown in Figure E.1, is employed. The model consists of a thin resistive target buried at a certain depth under the sea floor. Four different seawater depths are considered, $h_1 = 100$, 200, 400 and 1000 m. We also varied the depth ($h_2 = 200$, 400, 1000 m), thickness ($h_3 = 100$, 200, 400 m), and resistivity ($\rho_3 = 20$, 30, 50, 100 Ωm) of the reservoir. The reservoir itself extends 2000 m along the x and y axes, and its centre is located at $x = 0$ m and $y = 0$ m. The EM responses were simulated using the 3D TDEM finite-difference forward modelling code of Commer and Newman (2004) and the 3D FDEM finite-difference code of Newman and Alumbaugh (1995).
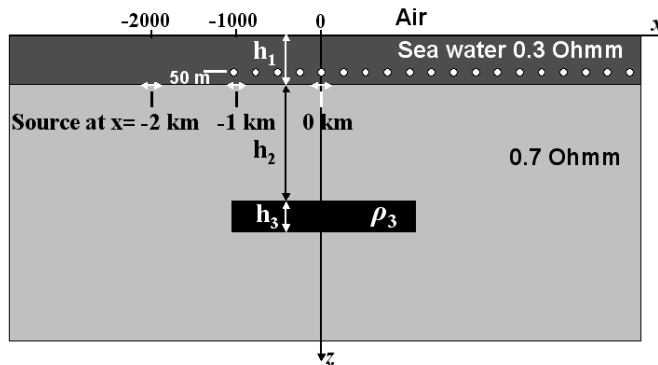

Figure E.1.: The 3D hydrocarbon reservoir model and survey configuration. The white horizontal arrows correspond to the transmitter positions, the white circles show the receiver profile.

E.1.1. Time-domain modelling

We first analyze TDEM responses over the thin resistive target. The signals are excited by a 250-m long x-oriented grounded wire. Three transmitter locations at

the bottom of the sea are considered, marked by the white horizontal arrows in Figure E.1, these are $x_{tr} = -2000, -1000, 0$ m, with $y_{tr} = 0$ m and $z_{tr} = 0$ m constant. The TDEM responses were calculated for a profile of 45 receivers with a receiver spacing of 250 m along the x-axis. The profile is located 50 m above the sea floor.

To choose an optimal 3D grid for our simulations, its responses are calculated for a 1D layered model without the resistive target and compared against a quasi-analytical 1D solution. For the survey scenario depicted in Figure E.1, a grid of $153 \times 153 \times 90$ nodes was used. Its smallest mesh spacing is $\Delta_{min} = 50$ m, hence, the initial time step required by the FD scheme of Commer and Newman (2004) is $\Delta t_0 = 10^{-4}$ s.
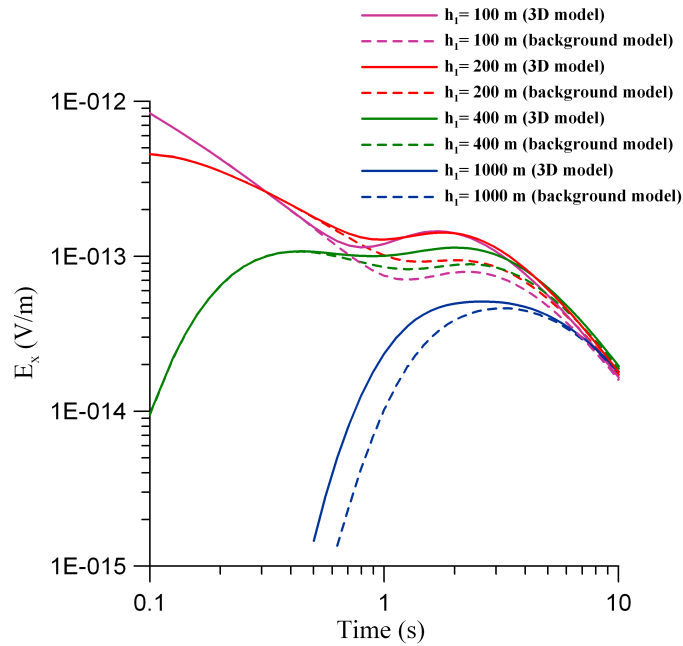

Figure E.2.: Horizontal electric field, E_x, excited by an impulse source. The curves are given for various seawater depths. The transmitter is located at $x_{tr} = -2000$ m and the receiver at $x_{rc} = 2000$ m. The solid lines show the 3D responses, the dashed lines present the background responses. The depth of the reservoir is $h_2 = 1000$ m.

E.1.1.1. Impulse source

First, we consider an impulse signal for source excitation. The horizontal, E_x, and the vertical, E_z, electric fields were calculated for all $(4 \times 3 \times 3 \times 4 = 144)$ possible
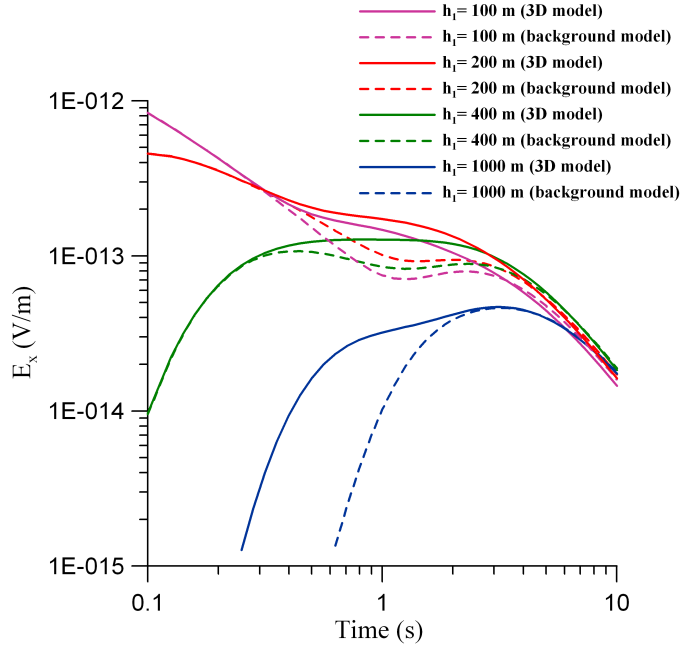
Figure E.3.: The same as Figure E.2, but for the depth of the reservoir $h_2 = 200$ m.

values of the model parameters (h_1, h_2, h_3 and ρ_3). Figure E.2 exemplifies the responses obtained for $h_3 = 200$ m and for $\rho_3 = 50$ Ωm. The figure shows these responses for a source-receiver offset of 4 km, and a source position of $x_{tr} = -2000$ m. Experimenting with different transmitter positions, we found that the position $x_{tr} = -2000$ m yields the highest sensitivity. Moreover, as shown below, for the target geometry considered here, this spacing produces a maximum reservoir effect on E_x (cf. Figure E.6(a)). In Figure E.2 the curves are plotted as a function of time for four seawater depths ($h_1 = 100, 200, 400, 1000$ m). In this figure the responses of the 3D target are solid lines and background responses are dashed lines of the same colour. A visible effect of the reservoir is seen for all four seawater depths. In Figure E.3 the responses are exemplified for a more shallow target ($h_2 = 200$ m). In comparison with Figure E.3, it can be observed that over the four different sea depths considered, the target response increases with the sea depth. Further analysis of these results is undertaken below in the Section "Comparison of time-domain and frequency-domain methods".

E.1.1.2. Step-off source

Keeping the geometry of the model and positions of the sources and receivers unchanged, we also simulated the responses generated by a step-off source signal. Here,

field generation is caused by shutting off an initially steady current within the horizontal grounded line source. Figure E.4 presents the responses again for the source position $x_{tr} = -2000$ m, and the receiver position $x_{rc} = 2000$ m. The curves are shown for $h_1 = 200$ and 1000 m. From here on, we focus our analysis on the case of a target thickness of $h_3 = 200$ m and a resistivity of $\rho_3 = 50$ Ωm. From this plot we can see that the target produces a significant signal. However, the observed differences between the background (dashed lines) and the 3D reservoir model responses (solid lines) mostly occur in the signal's DC limit, rather than during the transient's decay.
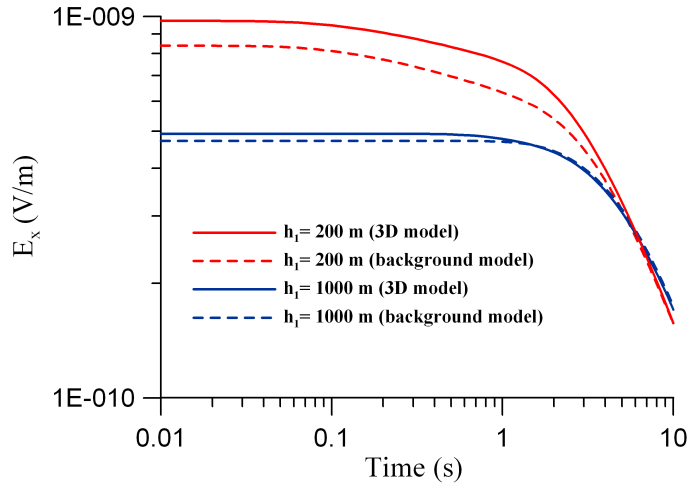

Figure E.4.: Horizontal electric field, E_x, excited by a step-off source signal. The curves are given for various seawater depths. The transmitter is located at $x_{tr} = -2000$ m and the receiver at $x_{rc} = 2000$ m. The solid lines show the 3D responses, the dashed lines present the background responses. The depth of the reservoir is $h_2 = 1000$ m.

E.1.2. Frequency-domain modelling

We now investigate to what extent a target response can be detected by the FDEM method. In order to be able to compare this method with TDEM, the model geometry and survey configuration were kept identical for both methods. The only difference is that now the x-directed horizontal electric dipole is energized with a sinusoidal waveform of a particular frequency.

In this study 6 frequencies are considered, these are 0.01, 0.03, 0.1, 0.3, 1 and 3 Hz. For each of the frequency pairs 0.01/0.03, 0.1/0.3, and 1/3, a separate 3D numerical grid is employed. The 3D frequency-domain FD code by Newman and Alumbaugh

(1995) is used for modelling. In order to verify the responses computed on the FD grids against quasi-analytical 1D solutions, we replaced the 3D resistive target by a continuous resistive layer, thus considering a 5-layered model (air, sea water, seabed, the resistive layer and again seabed). For the frequency pair 0.01/0.03 Hz a grid of size $126 \times 101 \times 126$ nodes is employed, with an uniform grid spacing of 200 m. For the pair 0.1/0.3 Hz, the grid size is $171 \times 101 \times 101$ nodes, and the smallest grid spacing is $\Delta_{min} = 100$ m. For the last two frequencies of 1 and 3 Hz the corresponding grid has $261 \times 181 \times 116$ nodes with $\Delta_{min} = 50$ m. Both horizontal, E_x, and vertical, E_z, electric fields were calculated for the 3D reservoir model using the following model parameters: $h_1 = 200, 1000$ m; $h_2 = 200, 1000$ m; $h_3 = 200$ m and $\rho_3 = 50$ Ωm.

Figure E.5 presents the amplitude of the horizontal electrical field, E_x, as a function of receiver position. The curves are plotted for the frequencies of 0.01, 0.1 and 1 Hz and for two seawater depths of $h_1 = 200$ and 1000 m. The source is located at $x_{tr} = -2000$ m.

Using a frequency of 1 Hz, no difference can be observed between the 3D reservoir model and background model responses for the case of a seawater depth of $h_1 = 200$ m (red line in Figure E.5). However for the deep water example (blue line) the 3D reservoir model starts to produce a larger scattered field and the difference to the background response grows until the receiver position reaches about 2500 m. Beyond this receiver position, the difference diminishes and then vanishes. The signal at this receiver distance is affected by the known effect caused by the air-water interface, when a strong airwave arrives at the sea floor. This airwave contains no information about the resistivity structure of the seabed. For source-receiver offsets larger than twice the seawater depth, the airwave starts to influence the EM signal, which is known as the airwave problem, see for example MacGregor *et al.* (2006). The depth of the sea controls the source-receiver offset, where sensitivity to the target is diminished or lost due to the airwave arrival. Because of this problem it is more difficult to detect the reservoir for shallow sea water. This is a disadvantage of the FDEM method.
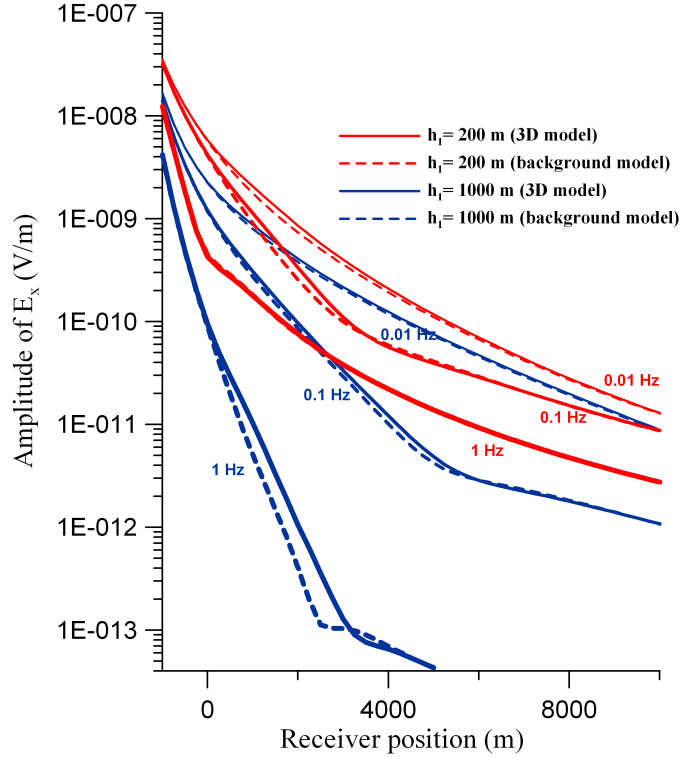
Figure E.5.: Horizontal electric field responses obtained using the 3D FDEM finite-difference code for two seawater depths $h_1 = 200, 1000$ m and for three frequencies of 0.01, 0.1 and 1 Hz. The transmitter is located at $x_{tr} = -2000$ m. The depth of the reservoir is $h_2 = 1000$ m. The solid lines again show the 3D reservoir model responses, the dashed lines present the background responses.

E.2. Comparison of time-domain and frequency-domain methods

To compare TDEM and FDEM responses, signal-to-noise ratios (SNR) were calculated for both methods. In this study signal is defined as the scattered horizontal electrical field of the reservoir, as noise the response of the background medium without the target. We show contour plots of SNR as a function of the source-receiver offset and time (or frequency) for the TDEM (or FDEM) modelling. In Figure E.6 we present the SNR for the model with shallow water ($h_1 = 200$ m) and deep target ($h_2 = 1000$ m), since this case happens to be the most difficult for all the methods considered. Figure E.6(a) presents the SNR for the TDEM method when the model is energized by the impulse signal, Figure E.6(b) shows the SNR for the step-off signal, and Figure E.6(c) shows the ratio for the FDEM method. To detect the
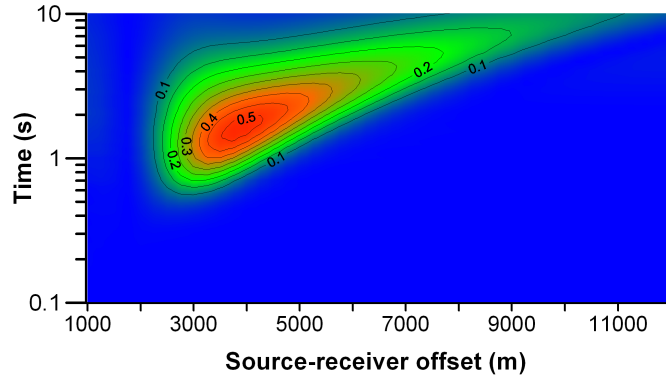
(a)
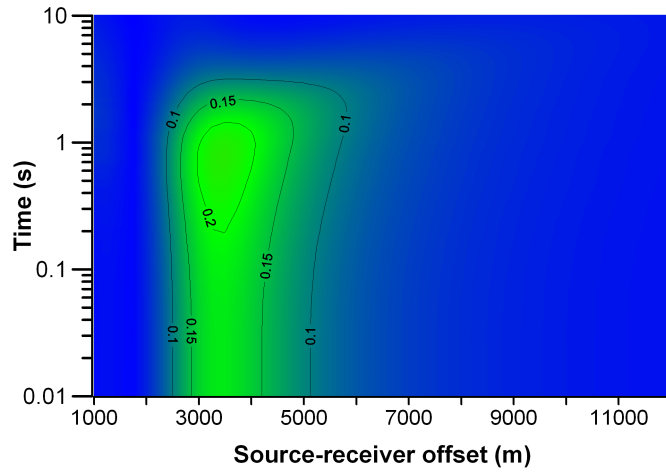
(b)
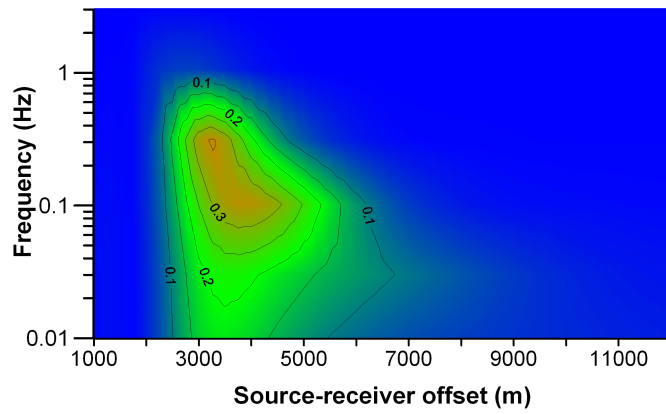
(c)

Figure E.6.: SNR obtained for the 200 m seawater depth and 1000 m depth of the target, the transmitter positioned at $x_{tr} = -2000$ m: (a) the time-domain method when the model is energized by the impulse source; (b) the time-domain method when the model is energized by the step-off source, and (c) the frequency-domain method.

reservoir, we require a minimum SNR of 0.1. When the transmitter is excited by the impulse signal, TDEM yields SNR values as large as 0.5, which indicates a very good target detectability. However, the contour plot in Figure E.6(a) shows that this region is relatively narrow, limited to a time range of 1.3 s to 2 s, and a range of source-receiver offsets between 3750 m and 4000 m. The SNR does not get larger than 0.2 using the step-off source (Figure E.6(b)). Therefore the impulse seems to be a favorable signal form for the TDEM method.

An important result is that TDEM together with the impulse source signal can detect the reservoir over the whole range of the receiver profile. Comparing the SNR values with the ones obtained using the FDEM method, the TDEM results indicate a better reservoir detectability. Also, we found that this is true for other transmitter positions (not presented here). The FDEM method is able to detect the target for source-receivers offsets from approximately 2000 m and up to 7000 m.

E.3. Conclusions

This preliminary study indicates that the TDEM method using an impulse source signal has a potentially better ability for detecting the type of hydrocarbon reservoir considered here. An advantage is that the airwave problem, encountered in FDEM methods, can be overcome. However, we believe that other source signal waveforms should also be analyzed.

References

Abubakar, A., Habashy, T., Druskin, V., Alumbaugh, D., Zerelli, A., and Knizhnerman, L. (2006). Two-and-half-dimensional forward and inverse modeling for marine CSEM problems. In *Expanded Abstracts*, pages 750–754. Society of Exploration Geophysicists.

Avdeev, D. B. (2005). Three-dimensional electromagnetic modelling and inversion from theory to application. *Surveys in Geophysics*, **26**(6), 767–799.

Avdeev, D. B. and Avdeeva, A. D. (2006). A rigorous three-dimensional magnetotelluric inversion. *Progress In Electromagnetics Research, PIER*, **62**, 41–48.

Avdeev, D. B., Kuvshinov, A. V., Pankratov, O. V., and Newman, G. A. (1997). High-performance three-dimensional electromagnetic modeling using modified Neumann series. Wide-band numerical solution and examples. *Journal of Geomagnetism and Geoelectricity*, **49**, 1519–1539.

Avdeev, D. B., Kuvshinov, A. V., Pankratov, O. V., and Newman, G. A. (2002). Three-dimensional induction logging problems, Part I: An integral equation solution and model comparisons. *Geophysics*, **67**, 413–426.

Avdeev, D. B., Utada, H., Kuvshinov, A. V., and Koyama, T. (2004). Three-dimensional electromagnetic modeling of the Hawaiian swell. In *AGU Fall Meeting Abstracts*.

Avdeeva, A. D. and Avdeev, D. B. (2006). A limited-memory quasi-newton inversion for 1D magnetotellurics. *Geophysics*, **71**, G191–G196.

Avdeeva, A. D., Commer, M., and Newman, G. A. (2007). Hydrocarbon reservoir detectability study for marine CSEM methods: Time-domain versus frequency-domain. In *San Antonio 2007 Annual Meeting Expanded Abstracts*, pages 628–632. SEG.

References

Badea, E. A., Everett, M. E., Newman, G. A., and Biro, O. (2001). Finite-element analysis of controlled-source electromagnetic induction using Coulomb-gauged potentials. *Geophysics*, **66**(3), 786–799.

Berdichevsky (1960). Principles of magnetotelluric profiling theory. *Applied Geophysics*, **28**, 70–91.

Byrd, R. H., Lu, P., Nocedal, J., and Zhu, C. (1995). A limited-memory algorithm for bound constrained optimization. *SIAM Journal on Scientific Computing*, **16**, 1190–1208.

Cagniard, L. (1953). Basic theory of the magneto-telluric method of geophysical prospecting. *Geophysics*, **18**, 605–635.

Caldwell, T. G., Bibby, H. M., and Brown, C. (2004). The magnetotelluric phase tensor. *Geophysical Journal International*, **158**, 457–469.

Chave, A. D., Thomson, D. J., and Ander, M. E. (1987). On the robust estimation of power spectra, coherences and transfer functions. *Journal of Geophysical Research*, **92**(B1), 633–648.

Chen, J., Oldenburg, D. W., and Haber, E. (2005). Reciprocity in electromagnetics: application to modelling marine magnetometric resistivity data. *Physics of the Earth and Planetary Interios*, **150**, 45–61.

Commer, M. and Newman, G. A. (2004). A parallel finite-difference approach for 3D transient electromagnetic modeling with galvanic sources. *Geophysics*, **69**, 1192–2002.

Constable, S. and Weiss, C. J. (2006). Mapping thin resistors and hydrocarbons with marine EM methods: Insights from 1D modeling. *Geophysics*, **71**, G43–G51.

Constable, S. C., Parker, R. L., and Constable, C. G. (1987). Occam's inversion: A practical algorithm for generating smooth models from electromagnetic sounding data. *Geophysics*, **52**(3), 289–300.

Constable, S. C., Orange, A. S., Morrison, H. F., and Hoversten, G. M. (1998). Marine magnetotellurics for petroleum exploration Part I: A sea-floor equipment system. *Geophysics*, **63**, 816–825.

References

Dmitriev, V. I. (1969). Electromagnetic fields in inhomogeneous media. *Moscow State University*.

Dorn, O., Bertete-Aguirre, H., Berryman, J. G., and Papanicolaou, G. C. (1999). A nonlinear inversion method for 3D electromagnetic imaging using adjoint fields. *Inverse Problems*, **15**, 1523–1558.

Egbert, G. D. (2002). Processing and interpretation of electromagnetic induction array data. *Surveys in Geophysics*, **23**, 207–249.

Egbert, G. D. and Booker, J. R. (1986). Robust estimation of geomagnetic transfer functions. *Geophysical Journal of the Royal Astronomical Society*, **87**(2), 173–194.

Eidesmo, T., Ellingsrud, S., MacGregor, L. M., Constable, S., Sinha, M. C., Johansen, S., Kong, F. N., and Westerdahl, H. (2002). Sea bed logging (SBL), a new method for remote and direct identification of hydrocarbon filled layers in deepwater areas. *First Break*, **20**, 144–152.

Ellingsrud, S., Eidesmo, T., Johansen, S., Sinha, M. C., MacGregor, L. M., and Constable, S. (2002). The meter reader - Remote sensing of hydrocarbon layers by seabed logging (SBL): results from a cruise offshore Angola. *The Leading Edge*, **21**, 972–982.

Farquharson, C. G. and Oldenburg, D. W. (1998). Non-linear inversion using general measures of data misfit and model structure. *Geophysical Journal International*, **134**, 213–227.

Fletcher, R. and Reeves, C. M. (1964). Function minimization by conjugate gradients. *The Computer Journal*, **7**, 149–154.

Gamble, T. D., Goubau, W. M., and Clarke, J. (1979). Magnetotellurics with a remote magnetic reference. *Geophyiscs*, **44**(1), 53–68.

Gatzemeier, A. and Moorkamp, M. (2005). 3D modelling of electrical anisotropy from electromagnetic array data: hypothesis testing for different upper mantle conduction mechanisms. *Physics of the Earth and Planetary Interios*, **149**, 225–242.

Gill, P. E., Murray, W., and Wright, M. H. (1981). *Practical optimization*. Academic Press, Inc.

References

Haak, V., Simpson, F., Bahr, K., Bigalke, J., Eisel, M., Harms, U., Hirschmann, G., Huenges, E., Jödicke, H., Kontny, A., Kück, J., Nover, G., Rauen, A., Stoll, J., Walther, J., Winter, H., Zulauf, G., and Wolfgang, J. (1997). KTB and the electrical conductivity of the crust. *Journal of Geophysical Research*, **102**, 18289–18306.

Haber, E. (2005). Quasi-Newton methods for large-scale electromagnetic inverse problems. *Inverse Problems*, **21**(1), 305–323.

Haber, E. and Oldenburg, D. W. (1997). Joint inversion: a structural approach. *Inverse Problems*, **13**(1), 63–77.

Haber, E., Asher, U., and Oldenburg, D. (2000). On optimization techniques for solving nonlinear inverse problems. *Inverse Problems*, **16**, 1263–1280.

Heise, W., Bibby, H. M., Caldwell, T. G., Bannister, S. C., Ogawa, Y., Takakura, S., and Uchida, T. (2007). Melt distribution beneath a young continental rift: the Taupo Volcanic Zone, New Zealand. *Geophysical Research Letters*, **34**, L14313.

Hohmann, G. W. (1975). Three-dimensional induced-polarization and electromagnetic modeling. *Geophysics*, **40**, 309–324.

Hoversten, G. M., Morrison, H. F., and Constable, S. C. (1998). Marine magnetotellurics for petroleum exploration, Part II: Numerical analysis of subsalt resolution. *Geophysics*, **63**, 826–840.

Hoversten, G. M., Newman, G. A., Geier, N., and Flanagan, G. (2006). 3D modeling of a deepwater EM exploration survey. *Geophysics*, **71**, G239–G248.

Johansen, S. E., Amundsen, H. E. F., Rosten, T., Ellingsrud, S., Eidesmo, T., and Bhuyian, A. H. (2005). Subsurface hydrocarbons detected by electromagnetic sounding. *First Break*, **23**, 31–36.

Jones, A. G. and Spratt, J. (2002). A simple method for deriving the uniform field MT responses in auroral zones. *Earth Planets Space*, **54**, 443–450.

Jones, A. G., Ferguson, I. J., Chave, A. D., Evans, R. L., and McNeice, G. W. (2001). Electric lithosphere of the Slave craton. *Geology*, **29**, 423–426.

Kelley, C. T. (1999). *Iterative methods for optimization*. SIAM.

<center>*References*</center>

Key, K. W., Constable, S. C., and Weiss, C. J. (2006). Mapping 3D salt using the 2D marine magnetotelluric method: Case study from Gemini Prospect, Gulf of Mexico. *Geophysics*, **71**, B17–B27.

Ledo, J., Jones, A. G., Ferguson, I. J., and Wolynec, L. (2004). Lithospheric structure of the Yukon, northern Canadian Cordillera, obtained from magnetotelluric data. *Journal of Geophysical Research (Solid Earth)*, **109**(B18), B04410.

Li, S., Unsworth, M., Booker, J., Wei, W., Tan, H., and Jones, A. (2003). Partial melt or aqueous fluid in the mid-crust of southern Tibet? Constraints from IN-DEPTH magnetotelluric data. *Geophysical Journal International*, **153**, 289–304.

MacGregor, L. M. and Sinha, M. C. (2000). Use of marine controlled source electromagnetic sounding for sub-basalt exploration. *Geophysical Prospecting*, **48**, 1091–1106.

MacGregor, L. M., Andreis, D., Tomlinson, J., and Barker, N. (2006). Controlled-source electromagnetic imaging on the Nuggets-1 reservoir. *The Leading Edge*, **25**, 984–992.

Mackie, R. L. and Madden, T. R. (1993). Three-dimensional magnetotelluric inversion using conjugate gradients. *Geophysical Journal International*, **115**, 215–229.

Mackie, R. L., Madden, T. R., and Wannamaker, P. E. (1993). Three-dimensional mangnetotelluric modeling using difference equations – Theory and comparisons to integral equation solutions. *Geophysics*, **58**, 215–226.

Mackie, R. L., Smith, J. T., and Madden, T. R. (1994). Three-dimensional electromagnetic modeling using finite difference equations: the magnetotelluric example. *Radio Science*, **29**(4), 923–935.

Mackie, R. L., Rodi, W., and Watts, M. D. (2001). 3-D magnetotelluric inversion for resource exploration. In *71st Annual International Meeting Extended Abstracts*, pages 1501–1504. SEG.

Mackie, R. L., Watts, M. D., and Rodi, W. (2007). Joint 3D inversion of marine CSEM and MT data. *SEG Expanded Abstracts*, **26**, 574.

Macnae, J. and Liu, G., editors (2003). *Three-Dimensional Electromagnetics - III*. Australian Society of Exploration Geophysicists.

References

Mareschal, M., Kellett, R. L., Kurtz, R. D., Ludden, J. N., Ji, S., and Bailey, R. C. (1995). Archaean cratonic roots, mantle shear zones and deep electrical anisotropy. *Nature*, **375**, 134–137.

McGillivray, P. R. and Oldenburg, D. W. (1990). Methods for calculating Frechet derivatives and sensitivities for the non-linear inverse problems. *Geophysics*, **60**, 899–911.

Mitsuhata, Y. and Uchida, T. (2004). 3D magnetotelluric modeling using the T-Ω finite-element method. *Geophysics*, **69**, 108–119.

Neves, A. S. (1957). *The magnetotelluric method in two-dimensional structures*. Ph.D. thesis, Massachusetts institute of technology.

Newman, G. A. and Alumbaugh, D. L. (1995). Frequency-domain modeling of airborne electromagnetic responses using staggered finite differences. *Geophysical Prospecting*, **43**, 1021–1042.

Newman, G. A. and Alumbaugh, D. L. (2000). Three-dimensional magnetotelluric inversion using non-linear conjugate gradients. *Geophysical Journal International*, **140**(2), 410–424.

Newman, G. A. and Boggs, P. T. (2004). Solution accelerators for large-scale three-dimensional electromagnetic inverse problem. *Inverse Problems*, **20**, s151–s170.

Newman, G. A., Recher, S., Tezkan, B., and Neubauer, F. M. (2003). 3D inversion of a scalar radio magnetotelluric field data set. *Geophysics*, **68**, 791–802.

Ni, Q. and Yuan, Y. (1997). A subspace limited memory quasi-Newton algorithm for large-scale nonlinear bound constrained optimization. *Mathematics of Computation*, **66**(220), 1509–1520.

Nocedal, J. and Wright, S. J. (1999). *Numerical optimization*. Springer-Verlag, New York.

Nover, G. (2005). Electrical properties of crustal and mantle rocks - a review of laboratory measurements and their explanation. *Surveys in Geophysics*, **26**, 593–651.

Oristaglio, M. and Spies, B., editors (1999). *Three-Dimensional Electromagnetics*. Society of Exploration Geophysicists.

References

Pellerin, L. (2002). Applications of electrical and electromagnetic methods for environmental and geotechnical investigations. *Surveys in Geophysics*, **23**, 101–132.

Polak, E. and Ribiere, G. (1969). Note sur la convergence de methodes de directions conjuguees. *Revue Francaise d'Informatique et de Recherche Operationnelle*, **16**, 35–43.

Reddy, I. K., Rankin, D., and Philips, R. J. (1977). Three-dimensional modelling in magnetotelluric and magnetic variational sounding. *Geophysical Journal of the Royal Astronomical Society*, **51**, 313–325.

Rodi, W. (1976). A technique for improving the accuracy of finite element solution for magnetotelluric data. *Geophysical Journal of the Royal Astronomical Society*, **44**, 483–506.

Rodi, W. and Mackie, R. L. (2001). Nonlinear conjugate gradients algorithm for 2-D magnetotelluric inversion. *Geophysics*, **66**(1), 174–187.

Sasaki, Y. (2004). Three-dimensional inversion of static-shifted magnetotelluric data. *Earth Planets Space*, **56**, 239–248.

Simpson, F. and Bahr, K. (2005). *Practical magnetotellurics*. University press, Cambridge, UK.

Simpson, F. and Tommasi, A. (2005). Hydrogen diffusivity and electrical anisotropy of a peridotite mantle. *Geophysical Journal International*, **160**, 1092–1102.

Singer, B. S. (1995). Method for solution of maxwell's equations in non-uniform media. *Geophysical Journal International*, **120**(3), 590–598.

Siripunvaraporn, W., Egbert, G., and Lenbury, Y. (2002). Numerical accuracy of magnetotelluric modeling: A comparison of finite difference approximations. *Earth Planets Space*, **54**, 721–725.

Siripunvaraporn, W., Egbert, G., Lenbury, Y., and Uyeshima, M. (2005). Three-dimensional magnetotelluric inversion: data-space method. *Physics of the Earth and Planetary Interios*, **150**, 3–14.

Tikhonov, A. N. (1950). On determining electric characteristics of the deep layers of the Earth's crust. *Dokl. Acad. Nauk. SSSR*, **73**, 295–297.

References

Tikhonov, A. N. (1963). Regularization of incorrectly posed problems. *Soviet Mathematics Doklady*, **4**, 1624–1627.

Um, E. and Alumbaugh, D. (2005). On the physics of the marine-time-domain controlled source electromagnetic method for detecting hydrocarbon reservoirs. In *Expanded Abstracts*, pages 583–586. Society of Exploration Geophysicists.

Wang, T. and Fang, S. (2001). 3-D electromagnetic anisotrophy modeling using finite differences. *Geophysics*, **66**, 1386–1398.

Wannamaker, P. E. (1991). Advances in three-dimensional magnetotelluric modeling using integral equations. *Geophysics*, **56**(11), 1716–1728.

Ward, S. H. and Hohmann, G. W. (1987). Electromagnetic theory for geophysical applications. In M. N. Nabighian, editor, *Electromagnetic methods in applied geophysics*, pages 131–311. Society of Exploration Geophysicists, Tulsa.

Weidelt, P. (1975a). Electromagnetic induction in 3D structures. *Geophysical Journal International*, **41**, 85–109.

Weidelt, P. (1975b). Inversion of two-dimensional conductivity structures. *Physics of the Earth and Planetary Interios*, **10**, 281–291.

Xiong, Z. (1999). Domain decomposition for 3D electromagnetic modelings. *Earth Planets Space*, **51**, 1013–1018.

Yoshioka, K. and Zhdanov, M. S. (2005). Electromagnetic forward modeling based on the integral equation method using parallel computers. In *SEG expanded abstracts*, volume 24, pages 550–553.

Zhdanov, M. S. and Golubev, N. G. (2003). Three-dimensional inversion of magnetotelluric data in complex geological structures. *Austr. Soc. Expl. Geophys.*, **20**, 550–553.

Zhdanov, M. S. and Tolstaya, E. (2004). Minimum support nonlinear parametrization in the solution of a 3D magnetotelluric inverse problem. *Inverse Problems*, **20**, 937–952.

Zhdanov, M. S. and Wannamaker, P. E., editors (2002). *Three-Dimensional Electromagnetics*, Methods in Geochemistry and Geophysics, 35. Elsevier.

References

Zhdanov, M. S., Varentsov, I. M., Weaver, J. T., Golubev, N. G., and Krylov, V. A. (1997). Methods for modelling electromagnetic fields: Results from COMMEMI - the international project on the comparison of modelling methods for electromagnetic induction. *Journal of Applied Geophysics*, **37**, 133–271.

Zyserman, F. and Santos, J. (2000). Parallel finite element algorithm with domain decomposition for three-dimensional magnetotelluric modeling. *Journal of Applied Geophysics*, **44**, 337–351.